U.PORTO
FEUP FACULDADE DE ENGENHARIA
UNIVERSIDADE DO PORTO

Master's in Bioengineering

Structure-function analysis of a carbohydrate esterase family 5 enzyme from *Thielavia terrestris*

Master Thesis in Biological Engineering

by Leonor Vieira Carneiro

In association with Chalmers Tekniska Högskola

Supervision by Dr. Vera Novy, Dr. Olga Nunes,
Professor Lisbeth Olsson,

Porto, June 2020

Structure-function analysis of a carbohydrate esterase family 5 enzyme from *Thielavia terrestris*

LEONOR CARNEIRO

Faculdade de Engenharia da Universidade do Porto
Project developed in association with
Chalmers Tekniska Högskola

Porto, June 2020

Structure-function analysis of a carbohydrate esterase family 5 enzyme from *Thielavia terrestris*

Supervisors:

Dr. Vera Novy, Postdoctoral researcher at Industrial Biotechnology Division, Department of Biology and Biological Engineering, Chalmers Tekniska Högskola

Dr. Olga Nunes, Teacher at Faculdade de Engenharia da Universidade do Porto; Member of Process, Environment, Biotechnology and Energy Laboratory at Faculdade de Engenharia da Universidade do Porto

Professor Lisbeth Olsson, Head of Industrial Biotechnology Division, Department of Biology and Biological Engineering, Chalmers Tekniska Högskola

Faculdade de Engenharia da Universidade do Porto,

Rua Dr. Roberto Frias, s/n 4200-465 Porto Portugal

Telephone +351 22 508 14 00 Email feup@fe.up.pt

Porto, Portugal 2020

Thank you to mom, dad, and sis, who have made big efforts to offer me the most comfortable Erasmus experience. Unfortunately, the situation went backwards. However, your support was not in vain.

This is the result.

Acknowledgments

I would first like to thank PhD student Jae Ho Shin and master student Clarisse Breard for having welcomed me in their docking team. It was a pleasure to learn from both. I am grateful for all shared knowledge and advice, and for the overall support throughout my work. I would like to offer my special thanks to Jae Ho, whose 'classes' about homology modelling and docking analysis were crucial for the development of this project.

I would also like to thank associate Professor Johan Larsbrink for his availability in designing the phylogenetic tree, which is the basis of the promising prospects of this work.

I very much appreciated the insight into docking analysis given by post-doctoral fellow Scott Mazurkewich. I would especially like to acknowledge his initial advice on product docking which, in the end, led to an interesting discussion of results.

Thank you to my supervisor in my home faculty, Dr. Olga Nunes, for her support during the initial changes in the planned workflow and her valuable revision of the preliminary version of this report.

Thank you to Head of IndBio Division, Professor Lisbeth Olsson, for having accepted my application and for her concern in the successful fulfilment of my project.

I would also like to acknowledge the opportunity of participating in the online *Fikas* for sharing of results and discussion of science topics with the members of the 'Enzymes' subgroup.

My sincere thanks are extended to all IndBio members who have allowed me to learn so much from them even at distance.

Finally, I would like to express my deepest appreciation to my supervisor, post-doctoral researcher Dr. Vera Novy, who believed in my abilities since day one. This work would not have been possible without her valuable teaching, unwavering guidance, constructive criticisms, full encouragement, emotional support, and relentless commitment, even when the circumstances were not the most suitable. I could have not asked for a better person to guide me throughout this journey, which though taken remotely, was valuable for my growth as a person and as a scientist.

Abstract

One promising way of mitigating climate change is by utilizing lignocellulosic biomass in the biorefinery context. Suberin, one of the main components of the outer bark of trees, is a valuable hydroxylated polyester for the production of novel biochemicals. Hence, enzymatic methods are required to retrieve suberin from the barks of trees in a native-like state. Cutinases are CE5 enzymes which can cleave the ester-groups of long-chain hydrophobic compounds, such as suberin, thus enabling this task. However, the structural and biochemical characterization of these family of enzymes is still underexplored.

Therefore, study of the interactions of realistic building blocks of suberin with cutinases is relevant to promote insight into their structural-functional features. To address this goal, homology model of a *Thielavia terrestris* cutinase, an industrial relevant enzyme for polyester degradation, was built and docking analysis was performed using feruloyl esters with successively longer chains.

The main conclusions of this work concern the structural-functional features of the *T. terrestris* cutinase, namely its catalytic machinery, including the oxyanion hole, and the binding cleft. The obtained simulated binding energies and experimental literature-based kinetic data showed a similar trend for feruloyl esters with short and middle chain lengths, however for long chain ligands, low activities corresponded to high binding energies. Evidence supported on docking of the resulting products of the catalytic reaction enabled drawing of conclusions over the contribution of the aliphatic chain of the feruloyl esters in the total binding energy of the cutinase-substrate complex. The beginning of a possible structure-activity-homology analysis is initiated using two additional cutinases.

Keywords

bio-based chemicals, cutinase, suberin,

homology modelling, docking

Declaration

Declara, sob compromisso de honra, que este trabalho é original e que todas as contribuições não originais foram devidamente referenciadas com identificação da fonte.

Leonor Vieira Carneiro Porto, 25 de junho de 2020

One declares, under honor, that this work is original and that all non-original contributions were duly referenced with identification of the source.

Leonor Vieira Carneiro Porto, 25th june 2020

Contents

List of Figures

List of Tables

List of Abbreviations

List of aminoacids:

Alanine - Ala

Asparagine - Asn

Aspartate – Asp

Glutamine – Gln

Glycine – Gly

Histidine – His

Leucine – Leu

Phenylalanine – Phe

Serine – Ser

List of microorganisms:

Fusarium solani pisi – *F. solani*

Glomerella cingulata – *G. cingulata*

Malbranchea cinnamomea – *M. cinnamomea*

Thielavia terrestris – *T. terrestris*

Trichoderma reesei – *T. reesei*

List of feruloyl esters:

Ferulic acid (FA) associated to an aliphatic chain of x carbons (-Cx)

FA-CH_3, FA-C2, FA-C4, FA-C6, FA-C8, FA-C10, FA-C12, FA-C14, FA-C16, FA-C18

List of units:

Ångström – Å

Other abbreviations:

3-phenethylthio-1,1,1-trifluoropropan-2-one - PETFP

4-nitrophenyl esters – pNP

Carbohydrate esterase family 5 – CE5

Carbon dioxide – CO_2

Difference of the binding energy of substrate and correspondent product - 'dGsubstrate – dGproduct'

European Union – EU

GenBank accession number – Gb

Industrial Biotechnology Division – IndBio

Polyethylene terephthalate – PET

Poly(lactic) acid – PLA

Positional / spatial constraint – NOE constraint

Protein Data Bank – PDB

GMQE – global model quality estimate

QMEAN – model deviation from PDB crystallized structures

1. Introduction

1.1 Scope of Project

For several decades, greenhouse gas emissions from burning of fossil feedstocks have endangered the human health and have had a major negative impact on the environment. Therefore, alternatives for the utilization of fossil supplies are required. Biomass is one of those alternative resources in terms of provision of energy and production of high-added value materials.

Utilization of fatty acid compounds from renewable biomass is one promising way to realize a circular economy. A new special plant lipid compound can be retrieved from the bark of trees, an abundant waste stream from pulp mill industry (Gandini et al., 2006). The cork fraction of outer bark is mainly composed of suberin, a dense hydroxylated polyester (Graça, 2015) valuable for the production of advanced fuels (Kumaniaev & Samec, 2018) and novel bio-based materials (Gandini et al., 2006). Chemical methods for retrieving suberin from cork exist, comprising of alkaline hydrolysis using methanol with high energy input (Graça & Pereira, 2000). However, as these methods harm the valuable functional groups of suberin, current research is focusing in utilizing enzymes instead to achieve this purpose.

Cutinases belong to the carbohydrate esterase family 5 of enzymes (CE5), which is a very diverse family of poorly annotated enzymes (CAZy, 2020). They are esterases naturally produced by pathogenic fungi and bacteria as 'battle weapons' used to infect plant tissues, such as the external layer of barks and roots (Chen et al., 2013). When used in favour of technology, the infectious capability of these enzymes to degrade cork by cleaving the ester linkages present in suberin, could enable the recovery of functional and high-valued chemicals for biorefinery purposes.

So far, very little is known on cutinases and their biodiversity in terms of structure, function, activity, and substrate affinity. Also, suberin is a very dense and complex molecule, as it will be described hereinafter. Therefore, understanding the interaction between cutinases and realistic monomer models of suberin is important to correlate structural features of various cutinases from different microorganisms and their proven or yet to be proven capability of degrading substrates as dense as suberin.

For this work, an industrial relevant cutinase from the fungus *Thielavia terrestris* (XM_003655969.1) was selected because it was reported of being stable in a wide range of temperature and pH values, of being capable of degrading substrates with long chain aliphatic domains and of being successfully produced by a widely-used recombinant expression host, the yeast *Pichia pastoris* (Duan et al., 2019). However, no crystallized structure of this cutinase has been deposited.

In view of this, the main goal with this work is to build a model for *T. terrestris* cutinase and perform docking analysis to study its interactions with feruloyl esters with successively longer chain lengths. In the end, structural comparison will be discussed with other homologous cutinases, namely *Fusarium solani pisi* cutinase and *Malbranchea cinnamomea* cutinase.

1.2 Research Group

The Division of Industrial Biotechnology, Department of Biology and Biological Engineering at Chalmers University of Technology (IndBio) is led by Professor Lisbeth Olsson. The research focuses on finding technological solutions for the circular economy using renewable resources. Since 2008 they are a world leading institute in the biorefinery field, contributing significantly to the current knowledge in carbohydrate active enzymes, fermentation technologies, and many more.

1.3 Project Contributions

Using cutinases to release suberin monomers in their native configuration would contribute significantly to the creation of a circular economy. However, to achieve this goal, fundamental knowledge of these enzymes must be generated. This project will contribute significantly by understanding the enzyme structure of an industrially relevant cutinase as well as its molecular interaction with realistic model substrates. Connecting this knowledge to kinetic literature data will further support the findings of the structure-function analysis. Finally, structural traits of *T. terrestris* cutinase can be compared to others present in homologous cutinases. General conclusions can be drawn on this underexplored family of enzymes which are harbored in a newly built phylogenetic tree.

1.4 Layout of Dissertation

This dissertation is divided into four main parts: context and state of art, technical description, results and discussion, and conclusions and future work.

The context and state of art focuses on the actual prospects of biorefinery using lignocellulosic biomass, the value of suberin for novel biochemicals and a more detailed description of the chemical composition and macromolecular structure of this dense polyester. This section also focuses on cutinases as suberin-degrading enzymes. The problematic of identifying a true cutinase is introduced as is also a newly built phylogenetic tree harbouring all relevant cutinases for polyester degradation. Main structural features of cutinases are displayed using *F. solani* cutinase as an example and a collection of the few crystallized cutinases is also given.

The technical description section describes in detail homology modelling methods for *T. terrestris* cutinase and docking approach for both *T. terrestris* model and *F. solani* crystallographic structure.

Results and Discussion section display a focused interpretation of the results obtained with homology modelling and docking analysis of *T. terrestris* cutinase. In the end structural-activity comparison is performed between *T. terrestris*, *F. solani* and *M. cinnamomea* cutinases.

Conclusions of this project and future work are presented.

Supplementary material is given for all evidence and findings.

2. Context and State of Art

2.1 An Insight into Lignocellulosic Biorefinery

Since 1750, the carbon dioxide content of the atmosphere has increased by 43% (Schimel et al., 2015). In fact, the growth rate of atmospheric CO_2 during the 1960-69 decade was 0.85 ppm per year, while it climbed to 2.28 ppm per year during the more recent period (2008-17) (Raud et al., 2019). Furthermore, the mean global surface temperature suffered an increase of 0.85°C since the preindustrial era (Raud et al., 2019). This increase has already led to melting of glaciers and to a rise in sea levels. These environmental negative impacts are mainly due to our compulsory consumption of fossil feedstocks.

Renewable, environment-friendly alternatives to fossil supplies are required as awareness for limiting of greenhouse gas emissions and improvement of human and environmental health is raised.

The European Union states that approximately 30% of the total EU energy consumption will be provided by renewable sources by the year of 2030 (Comission, 2012). By this time, it also intends to replace 30% of oil-based chemicals with bio-based chemicals (Rübberdt et al., 2019).

Utilization of lignocellulosic biomass to produce fuels and chemicals represents the most promising way to achieve the goals set by the policy makers. Lignocellulosic biomass is the most abundant resource on Earth from the perspective of photosynthesis, as it has a global annual production of ~$220x10^{12}$ tons on dry basis (Ebaid et al., 2019). Additionally, lignocellulosic (or second-generation) products are not in direct conflict with food supply, which is the main issue of first-generation resources (Nigam & Singh, 2011).

The production of second-generation biofuel has already taken a leap in the research field and has already jumped to a commercial level in the heat and power supply sectors. Indeed, companies such as Fortum in Finland and Empyro (Empyro – BTG – Bioliquids BV) in the Netherlands have already settled a production process to produce lignocellulosic biofuel using the catalytic pyrolysis technology (Raud et al., 2019).

Nonetheless, according to a Norwegian study, the fossil fuel spot price (plus unit subsidy) must be above 1.3 €/L for wood-based biofuel production to be profitable (Jåstad et al., 2020). Nowadays, automotive gas oil, which accounts for 58% of the primary energy consumed, costs from 0.9 to 1.3 €/L (Comission, 2020; Nigam & Singh, 2011).

Improving the overall yield and lowering the production costs of large-scale second-generation biofuel production can be achieved with an integrative biorefinery approach with the production of high value-added chemicals.

Plant-based chemicals have been used in innumerable applications for thousands of years and new compounds have been developed in the past decades. Bio-polyethylene terephthalate (Bio-PET) is an alternative plastic, fatty acid esters from vegetable oils are present in lubricants, poly(lactic) acid fibres are used in clothing and bedding, cellulose fibres are used for absorbency in toilet paper and tissues, starches serve as adhesives (Shogren et al., 2019) and this list goes further on.

Nonetheless, one main issue regarding the industrial production of plant-based chemicals is their extraction and fractioning from recalcitrant lignocellulosic biomass. Hence, novel methods are required to extract these compounds in a native-like state.

2.2 Tree Bark - a Special Resource for Circular Economy

Tree barks are a quite abundant resource in many world forests and a side stream of the pulp and paper industries. In fact, a birch kraft pulp mill, with a typical yearly pulp production of 400,000 ton, generates about 28,000 ton of outer bark (Gandini et al., 2006). A promising way to realize a circular economy would be to contribute to process intensification, reutilizing the wasted bark to produce fuels and chemicals. In this way, land usage could be improved without the need for planting more trees.

Bark tissues develop from two lateral meristems: the vascular cambium, which gives rise to the interior wood tissue, and the phellogen, which produces the exterior phellem tissue, also known as cork (Leite & Pereira, 2017). Hence, cork is anatomically and chemically different from wood (Leite & Pereira, 2017). The average composition of cork from *Quercus suber*, which is taken as a reference cork material, is as follows: 16% extractives, 22% lignin, 20% polysaccharides and 43% suberin, this last one being the major component (Pereira, 2013).

Suberin acts as a lipophilic barrier to protect plant tissues against dehydration, wounding, and pathogen attacks (Bernards, 2002; Pollard et al., 2008), being that it is constantly produced according to environmental stimuli. This polymer itself is also recalcitrant to microbial degradation when present in plants (Kontkanen et al., 2009).

Accordingly, suberin is the polymer responsible for the possibility of using cork as a renewable resource to generate pyrolytic bio-oil with different composition and characteristics from those obtained from lignocellulosic agricultural and woody materials (Marques & Pereira, 2014). Additionally, the chemical composition of suberin, particularly the presence of valuable side groups, makes it particularly suited for the development of polymers with original architectures and interesting properties (Gandini et al., 2006).

However, attention is still necessary in understanding the chemical composition and macromolecular structure of suberin. In fact, the current knowledge about suberin structure derives mainly from compositional data generated by depolymerization and subsequent analysis of the depolymerization products or observations on the intact biopolymer by solid state NMR spectroscopy (Graça & Santos, 2007).

Structurally, suberin is a dense matrix comprising of a network of esterified fatty acids associated to a three-dimensional polyaromatic lignin-like moiety (Graça & Santos, 2007).

The monomers of suberin account for long-chain ω-hydroxyacids and α,ω-diacids, and small amounts of alkanoic acids and alkanols (Şen et al., 2010). Some of these monomers have a hydroxylation in carbon 9 of the fatty acid chain, followed by hydroxylation at either carbon 10 or the ω-carbon, resulting in valuable substituting groups such as epoxi rings and hydroxyl groups (Bernards, 2002). These monomeric structures are associated to glycerol and ferulic acid molecules, forming glyceryl esters and feruloyl esters (Graça & Santos, 2007). The major building blocks of suberin are represented in Figure 1 .

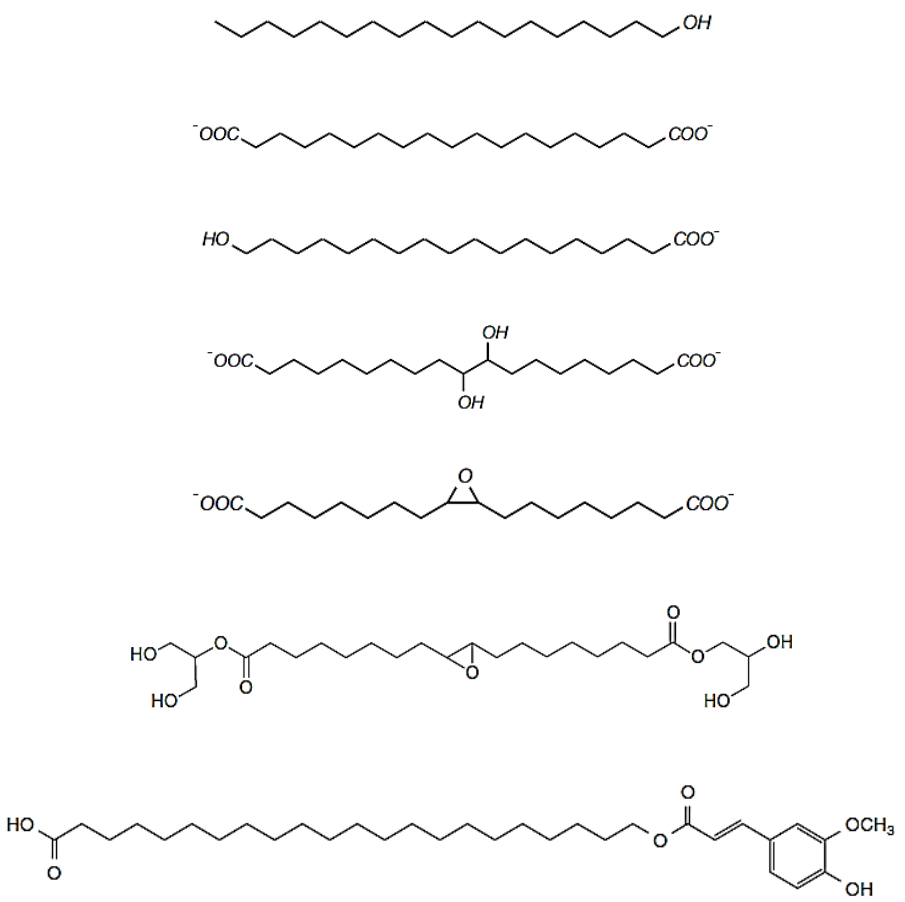

Figure 1. *Representative oligomers of suberin. From up to bottom: 1-alkanol; α,ω-alkanodioic acid; ω-hydroxyalkanoic acid; 9,10-dihydroxy-α,ω-alkanodioic acid; 9,10-epoxy-α,ω-alkanodioic acid; glycerol esterified to 9,10-epoxy-1,18-alkanodioic acid esterified to glycerol; 22-hydroxyalkanoic acid esterified to ferulic acid (adapted from Bernards, 2002; Graça & Santos, 2007).*

These building blocks assemble together in a macromolecular structure proposed by Bernards (2002) and Graça & Santos (2007), who considered that suberized cell walls are generally very thin and present a primary, a secondary and sometimes a tertiary wall. Polysaccharides and polyaromatics are present in the primary and tertiary cell walls and the secondary wall presents opaque and translucent lamellae of suberin and part of polyaromatics (Graça & Santos, 2007). Therefore, the proposed structural layout of the molecule is that of Figure 2. The polyaromatic fractions stay on the edges of the core molecule and the deployed alkyl moieties fill in the middle of the backbone structure.

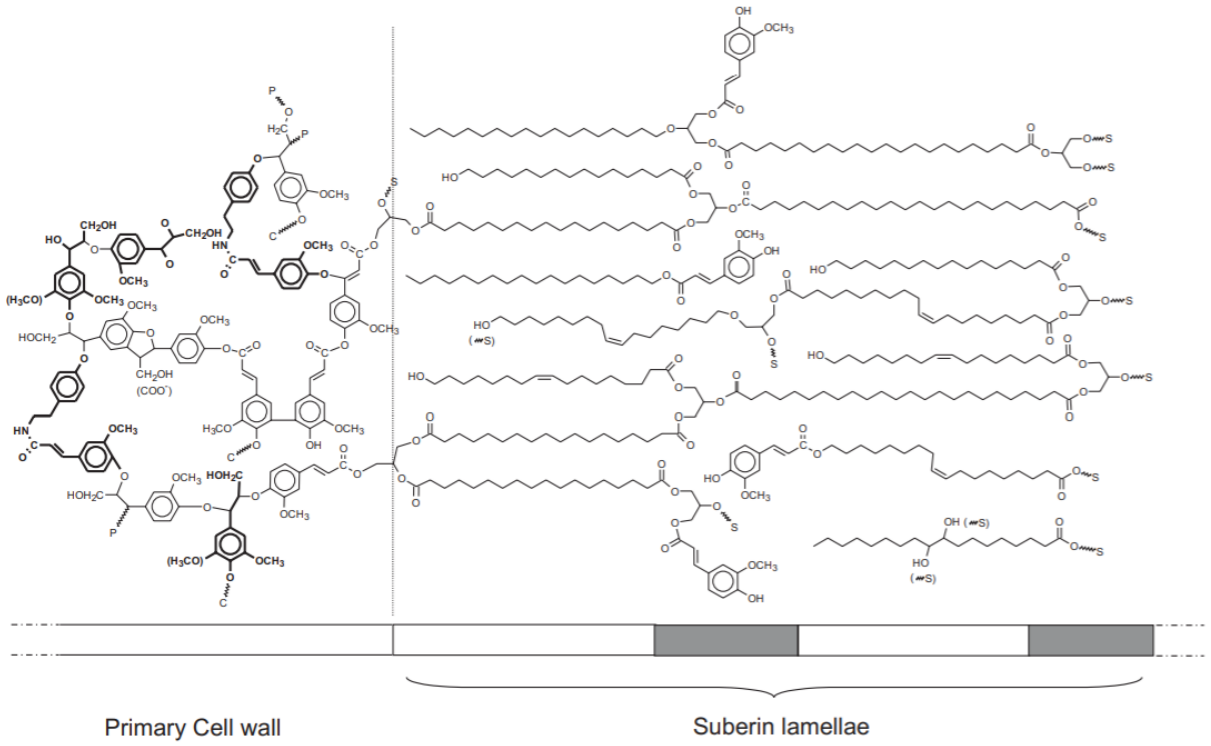

Figure 2. *Macromolecular assembly model of suberin (Bernards, 2002). Aromatic lignin-like fraction is present in the primary wall and esterified fraction is present in the secondary wall characterized by translucent (white) and opaque (grey) lamellae. This fraction comprises of hydroxylated fatty acids, which can be associated to glycerol molecules (connecting the C-chain to the hydroxycinnamic derivatives of the aromatic fraction) and to ferulic acid.*

2.3 Cutinase as a Plant Polyester Degrading Enzyme

Cutin is the major constituent of plant cuticle, a protective layer composed of waxes and lipid polymers that coats the epidermis of above ground portions of terrestrial plants. Its function is to protect the plant from dehydration and infection by pathogen organisms (Chen et al., 2013). This polymer is composed of hydroxylated 16-18-carbon fatty acids linked together via ester bonds, having a similar structure and composition as suberin (Nyyssölä, 2015).

Cutinases (EC 3.1.1.74) are serine esterases belonging to the hydrolase super family presenting a Ser-His-Asp (Serine-Histidine-Aspartate) catalytic triad, where the serine is exposed to the solvent (Chen et al., 2013). Cutinases are produced by both fungi and bacteria and are capable of hydrolysing both cutin and suberin. In fact, several suberin-degrading esterases have been identified as cutinases and are active on both cutin and suberin (Järvinen et al., 2009). Additionally, bacterial cutinases may also be active on suberin because cutinase production is induced by suberin in *Thermobifida* (Fett et al., 1999).

The versatile catalytic ability of cutinases led to the early recognition that these enzymes were potentially useful for a variety of industrial applications (Carvalho et al., 1999). Since then numerous studies were carried out to discover and characterize putative cutinases and systems for industrial scale production of these enzymes. Altering cutinase specificity for a desired substrate or improving its stability has also been one of the focus of researchers. Indeed, cutinases have displayed good stability over a wide range of temperature and pH values and relatively good production yields and activity. As a result, they have substantial potential to be widely used in the food, chemical, detergent, environmental, and textile industries (Chen et al., 2013).

On the other hand, suberinases are still in a starting point when it comes to research, only having one of its encoding genes annotated (NCBI: txid1930), from *Streptomyces scabiei*, the causal agent of potato common scab (Komeil et al., 2013). Nonetheless, they also seem promising candidates for industrial applications regarding biofuel production from materials such as cork (Marques & Pereira, 2014). Still, efforts need to be made to thoroughly characterize and annotate suberinases from different microorganisms to keep up with the current annotation status of putative cutinases.

2.3.1 The Struggle of Identifying a True Cutinase

In the context of this work, a phylogenetic tree was built harbouring all relevant cutinases and is given in Figure 3.

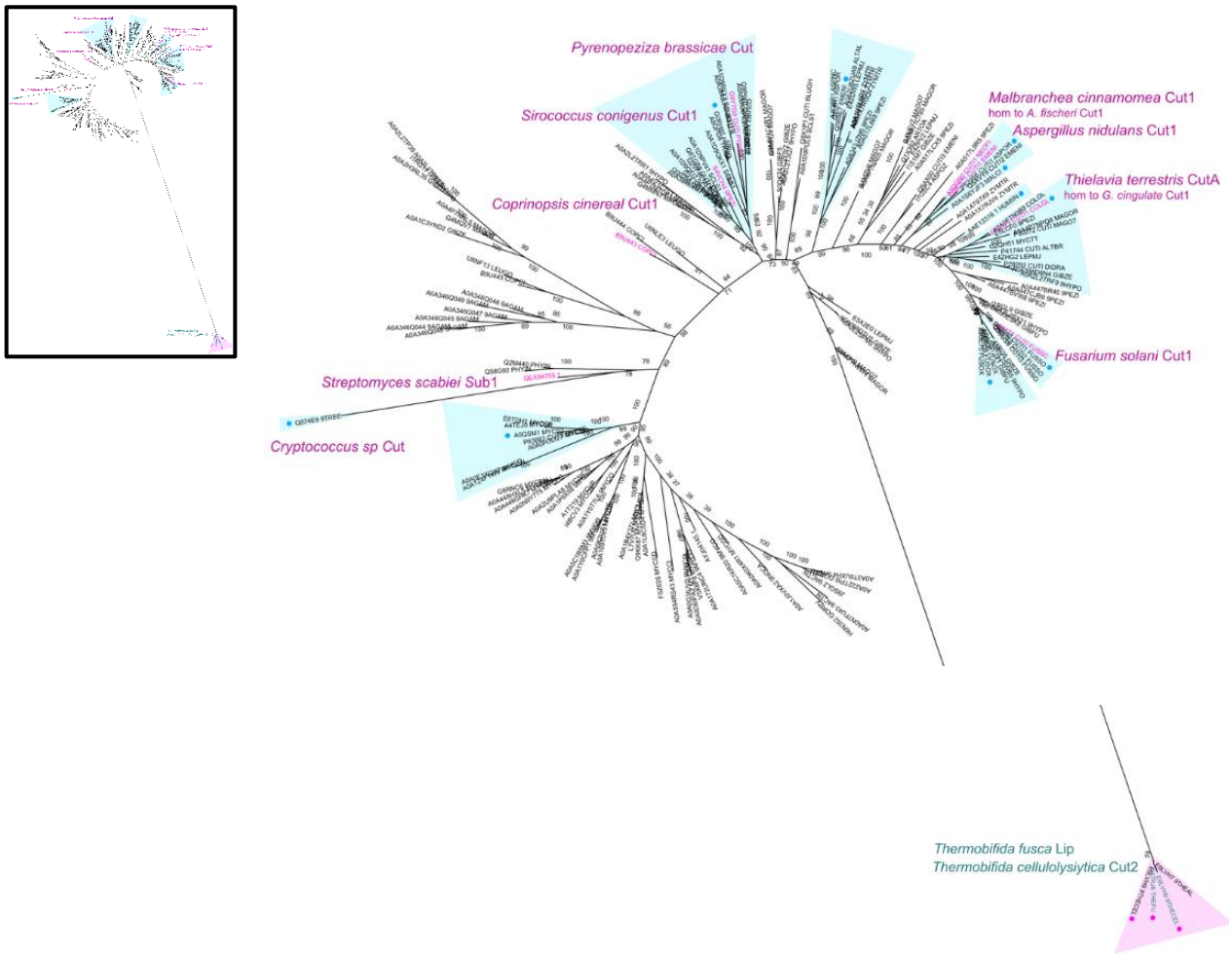

Figure 3. *Phylogenetic tree.*

Approximately 180 possible true cutinases were selected from over 3000 annotated cutinase sequences from bacterial and fungal microorganisms (CAZy, 2020). Only annotated cutinases with relatively good annotation score and promising for polyester degradation (assayed with suitable substrates or from pathogenic microorganisms) were chosen. The tree displays a broad range of homology, presenting 25% to 70% sequence identity between clusters.

A phylogenetic analysis reveals that the prokaryotic cutinases are distinct from the eukaryotic cutinases. Their low sequence identity indicates that they have undergone extensive evolutionary differentiation (Chen et al., 2013).

Previously, Belbahri et al. (2008) presented a study of interdomain gene transfer of cutinases between eukaryotic plant pathogens *Phytophthora* species and prokaryotic bacterial lineages. More precisely, they claimed a cutinase gene was likely acquired by a phytopathogenic water mold ancestor from an actinobacterial source, suggesting that gene transfer to fungi might be an important mechanism in the evolution of their virulence. However, later, Skamnioti et al. (2008b) recognized the existence of mycobacterial cutinases, but rejected the idea of lateral gene transfer to fungi, placing the bacterial cutinase sequences in a separate group.

Regarding gene expression, different putative cutinases are expressed at different times during the microbial life cycle (Skamnioti et al., 2008a, 2008b). Plus, a single species can contain several putative cutinases, as it occurs with *Magnaporthe oryzae* cutinase family, which comprises 14–17 genes encoding putative serine esterases (Skamnioti et al., 2008a).

Also, Skamnioti et al. (2008b) categorized the *Magnaporthe grisea* cutinases into four temporal regulatory patterns, which are associated with the complex requirements of pathogenesis (signal perception and transduction, penetration and nutrition).

Intriguingly, they found no genes that were solely induced upon initial spore contact with the host, as hypothesized based on findings in *F. solani* cutinases (Kolattukudy et al., 1995). As a result, they deduced that multiple cutinases are expressed constitutively and/or that during early host perception, they may be acting together with transcriptionally activated penetration-enabling cutinases. Additionally, they verified that the differentiation in the expression patterns in constitutively expression genes was not associated with the phylogenetic closeness of the putative cutinases, thus deducing that there has been considerable subfunctionalization and neofunctionalization among the putative cutinases (Skamnioti et al., 2008b).

Consequently, an enzyme coded by a gene homolog to a true cutinase gene and showing strong virulence capability against esterified substrates may not display cutinase activity.

Therefore, it is advised to develop practical means of identifying a true cutinase, specifically demonstrating the ability of an isolated protein to hydrolyse cutin or a suitable substitute. Assays to detect true cutinases were reviewed by Chen et al. (2013).

The classical method to measure cutinase activity is to use cutin as the substrate and detect the cutin monomers released by hydrolysis. This can be achieved using radiolabelled cutin, non-specifically labelled cutin with the chromogenic compound Remazol Brilliant Blue R (RBB) and native cutin. Although enzymatic assays aiming to identify proteins with real cutinase activity seem more than reliable, the difficulty in identifying true cutinases relates to the fact that natural cutin is commercially unavailable and the procedure to prepare it in the laboratory is challenging and time consuming, comprising of organic solvent extractions and enzymatic hydrolysis.

Therefore, possible substrate alternatives are synthetic high molecular weight polyesters, such as PET, poly (ε-caprolactone), PLA and poly (butylene succinate), which are much easier to obtain. Other alternative is to measure esterase activity of cutinase by monitoring the hydrolysis of 4-nitrophenyl esters (pNP). Though these substrates are of easy access, they are highly susceptible to impurities in the enzyme preparation because many esterases are capable of hydrolysing them.

To avoid the susceptibility of these assays, using triacylglycerols (normally used to characterize lipases) seems a suitable alternative. However, this assay is not only susceptible to lipases that may be present in the enzyme preparation but also it cannot be used to identify a true cutinase, only to characterize its esterase activity.

Within the scope of identifying enzymes with real cutinase activity, sequences encoding true cutinases have been deposited and can be accessed using their Genbank accession numbers (Gb). A short collection of annotated true cutinase encoding genes shows next: *F. solani* (Gb. AAA33334.1); *Aspergillus nidulans* (Gb. ABF50887.1); *Aspergillus niger* (Gb. CAL00335.1); *Monilinia fructicola* (Gb. AAZ95012.1); *Pyrenopeziza brassicae* (Gb. CAB40372.1); *Botrytis cinerea* (Gb. CAA93255.1); *Magnaporthe grisea* (Gb. EHA46959.1); *Aspergillus oryzae* (Gb. BAA07428.1); *Pseudozyma antarctica* (Gb. GAC73680.1); *Coprinopsis cinerea* (Gb. EU435153.1); *Thermobifida fusca* (Gb. AAZ54920.1; Gb. AAZ54921.1); *Thermobifida alba* (Gb. ADV92525.1); *Thermobifida cellulosilytica* (Gb. ADV92527.1); *Cryptococcus sp.* (Gb. BAK82405.1).

2.3.2 Cutinase Structure and Function

The first X-ray crystal structure of the cutinase from *F. solani* (PDB ID: 1CUS) was described in 1992 (Martinez et al., 1992) and is given in Figure 4.

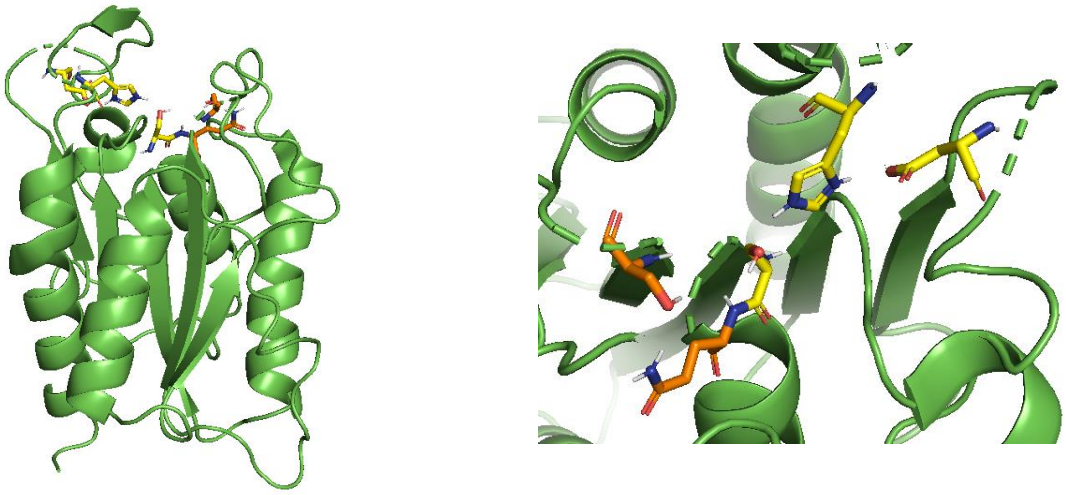

Figure 4. *Crystallographic structure of cutinase from* F. solani *(PDB ID: 1CUS). Side view and top view. Enzyme is represented in green cartoon figure. Fungal cutinases all display beta sheets enclosed by helixes pointing towards the binding cleft. The active site residues are shown in stick figures coloured in yellow. The oxyanion hole residues, whose amides are responsible for donating hydrogens to stabilize possible ligands, are represented in stick figures in orange. Catalytic serin is exposed to the solvent. The catalytic residues are Ser120-Asp175-His188; oxyanion hole residues are Ser42-Gln121, being Gln (glutamine) the residue following the catalytic serine.*

This structure revealed that *F. solani* cutinase adopts an α/β fold that exposes the catalytic serine (Ser120) to the solvent, instead of burying the active site with a hydrophobic loop (Chen et al., 2013). The presence of this lid covering the active site in true lipases is the reason behind their induced activity at aqueous/lipid interfaces (Cambillau et al., 1996), thus its absence in cutinases is considered to be responsible for their lack of interfacial activation. Upon this, cutinases are distinguished from lipases because they can hydrolyse insoluble substrates in solution or in emulsion, while lipases are only activated by interfacial effects. Accordingly, cutinases are capable of hydrolysing low molecular weight soluble esters and short and long chain triacylglycerols. They are also able of degrading high molecular weight cutin and synthetic polyesters, such as PET and poly (ε-caprolactone). In addition, cutinases catalyse esterification and transesterification reactions (Chen et al., 2013).

A collection of all crystal structures of cutinases (native and mutants) are presented in Table 1. Note that the crystallographic structure of *F. solani* cutinase is the most studied so far.

Table 1. *All crystallized structures of cutinases.*

	Microorganism	PDB ID
Fungal cutinases	*Fusarium solani pisi*	1 CUD*, 1CUW*, 1OXM, 1XZK, 1XZA*, 1CUS, 1CEX, 1CUB*, 1CUA*, 1CUZ*, 1CUY*, 1CUX*, 1CUV*, 1CUU*, 1CUJ*, 1CUI*, 1CUH*, 1CUG*, 1CUF*, 1CUE*, 1CUC*, 1XZJ*, 1XZI*, 1XZH*, 1XZG*, 1XZF*, 1XZE*, 1XZD*, 1XZM, 1XZL, 1XZC*, 1XZB*, 1AGY, 1FFE*, 1FFD*, 1FFC*, 1FFB*, 1FFA*, 2CUT, 3ESA, 3ESB, 3ESC, 3ESD, 3EF3, 3QPC, 3QPA
	Cryptococcus sp.	2CZQ
	Glomerella cingulata	3DCN, 3DEA, 3DD5
	Aspergillus oryzae	3GBS, 3QPD
	Humicola insolens	4OYL, 4OYY
	Trichoderma reesei	4PSD, 4PSC, 4PSE
	Fusarium oxysporum	5AJH
	Malbranchea cinnamomea	5X88
Bacterial cutinases	*Thermobifida alba*	6AID, 6THT, 3WYN, 3VIS
	Leaf branch compost	4EBO, 6THS*, 6THT*
	Thermobifida fusca	5ZOA, 4CG1, 4CG2, 4CG3
	Saccharomonospora viridis	4WFK*, 4WFI*, 4WFJ*, 5ZNO*, 5ZRR*, 5ZRS*, 5ZRQ*
	Thermobifida cellullosilytica	5LUJ, 5LUK*, 5LUI, 5LUL*
	Idionella sakaiensis	6ANE
	Mycobacterium tuberculosis	5W95

Mutant variants are signaled with *. These structures were obtained searching the Protein Data Bank (PDB) database (Worldwide PDB, 2020) using 'cutinase' as search word. The results showed consisted of cutinases but also enzymes annotated as PETases (as they have a high capability of degrading PET but are homologous to cutinases), lipases and acetylxylan esterases. Only the relevant cutinases were collected here.

Regarding docking analyses on cutinases, the number of studies encountered is small (Araújo et al., 2007; Kawabata et al., 2017, 2018; Kitadokoro et al., 2012; Shinozaki et al., 2013). Lipase and PETase docking analysis of bulky substrates, such as PET, is of relevance too, but still lack in literature (Austin et al., 2018; Li et al., 2011; Ma et al., 2018).

3. Technical Description

3.1 Homology Modelling

The target sequence of *T. terrestris* cutinase (XM_003655969.1) was retrieved from the NCBI protein sequence database (Medicine, 2020). Homology models were built using the SWISS-MODEL server, (Andrew et al., 2018; Biozentrum, 2020; Guex et al., 2009), the I-TASSER server (Lab, Zhang, 2020; Roy et al., 2010; Zhang, 2015), the PHYRE2 server (Kelley et al., 2015; Structural Bioinformatics Group, 2020) and the Prime tool from Maestro 12.3 (Schrödinger Release 2020-1). The identified template structures for each built model are present in Table S1.

The SwissModel template library (SMTL version 2020-04-15, PDB release 2020-04-10) was searched with BLAST and HHBlits for evolutionary related structures matching the target sequence. Overall, 1301 templates were found by the server. 6 templates were chosen by the author according to evaluating parameters, such as GMQE value (global model quality estimate), sequence identity, alignment coverage and the oligo-state and X-ray resolution of the crystal structures. With the chosen templates, SwissModel built single template homology models using ProMod3 3.0.0. The final Swiss model for the *T. terrestris* cutinase was selected considering the QMEAN value, which accounts for the deviation of the model relative to crystallized structures, and the new calculated GMQE value of the models built with the selected templates.

Phyre2 was run in intensive modelling mode. It encountered 120 crystal structures. The multi template homology model was built considering the top 5 templates selected by the server based on heuristics to maximize confidence, percentage identity and alignment coverage. The first 32 residues were modelled by *ab initio* techniques, being highly unreliable. 86% of the residues were modelled at >90% confidence.

iTasser identified structural templates from the PDB library by multiple threading approach. iTasser selected one template of the highest Z-score (highest alignment significance) from each threading program. The top 10 alignments were generated from the following threading programs of LOMETS meta-server: MUSTER, FFAS-3D, SPARKS-X, HHSEARCH2, HHSEARCH1, Neff-PPAS, HHSEARCH, pGenTHREADER, PROSPECT2 and PRC. Full-length

atomic models were constructed by iterative template-based fragment assembly simulations using SPICKER cluster program. The confidence of each model was quantitatively measured by C-score which was calculated based on the significance of threading template alignments and the convergence parameters of the structure assembly simulations. After the structure assembly simulation, iTasser used the TM-align structural alignment program to match the iTasser built models to all structures in the PDB library, resulting in the best 10 templates ranked by TM-score. The iTasser model chosen presented a C-score of 0.65 (estimated TM-score of 0.80 ± 0.09 and an estimated RMSD of 4.3 ± 2.9 Å).

The Prime homology modelling tool was used to build four different models. Two single template models and two consensus models were built using the Structure Prediction Wizard interface. Homologous crystal structures were found by blasting the target sequence to the NCBI PDB database, using the BLAST extension of Prime module. The secondary structure of the query sequence was then predicted. Then, the structural templates for each of the four models were chosen, considering the rationale described in section 4. Afterwards, the alignments between the query and the selected templates were calculated using ClustalW method (when the template structures chosen had high sequence identity with the query sequence, >50%) and STA method (when the template structures chosen had low sequence identity with the query sequence, <50%). The faster knowledge-based method was selected to build the models. The reasons behind building these different models are later discussed in section 4.

Phyre model was chosen for *T. terrestris* cutinase considering the N-terminus loop conformation of the enzyme and the disposition of the active site residues in all built models. This decision will be discussed in detail in section 4. Briefly, the templates of the model were from five different microorganisms: *F. solani*, *Glomerella cingulata, M. cinnamomea, Humicola insolens* and *Aspergillus oryzae.* Comparison of *T. terrestris* cutinase models with its templates (for decision of the best model for docking analysis and for structural comparison between homologous structures) was performed using PyMOL 2.4 (Schrödinger).

3.2 Docking Analysis

Docking analysis was performed using Schrödinger tools (Maestro 12.3-Schrödinger Release 2020-1). A detailed docking approach was carried out for *T. terrestris* and *F. solani* cutinases, using feruloyl esters with successfully longer chain lengths as substrates. The resultant products of the ester-cleaving reaction, the alcohols without the esterified ferulic acid, were also docked but only to *T. terrestris* cutinase. The methodology for the docking procedures is presented in the following.

3.2.1 Model Refinement

The chosen model from *T. terrestris* cutinase was refined using the Protein Preparation Wizard (Prepwizard) module of Maestro 12.3 (Schrödinger Release 2020-1). Bond orders were assigned, hydrogen atoms were added, disulfide bonds were created, missing side chains and loops were filled using Prime tool and waters beyond 5.00 Å from het groups were removed. H-bonds were assigned and optimized and restrained minimization job was incorporated. Same procedure was repeated for *F. solani* cutinase (PDB ID: 1cex).

3.2.2 Ligands Design and Preparation

All feruloyl esters and correspondent products with successively longer chain lengths, specifically C_2, C_4, C_6, C_8, C_{10}, C_{12}, C_{14}, C_{16} and C_{18}, were designed using ChemSketch (ACD/Labs). LigPrep module from Maestro 12.3 (Schrödinger Release 2020-1) was used to prepare the ligands by adding hydrogen atoms and generating 3D structures. Tautomers were generated and chirality was retained from the 3D structure. Ligands were ionized at pH (7.0 ± 2.0) using Epik. Energy minimization was performed resourcing to OPLS3e force field to generate the lowest-energy ligand isomer.

3.2.3 Docking of Starting Ligand

Neither the *T. terrestris* cutinase model nor the *F. solani* cutinase crystal structure had a complexed ligand. To make the catalytic pocket ready for docking of molecules, a starting ligand was introduced in both receptor structures. To avoid faulty interaction of the alcohol group of the ferulic acid with the oxyanion hole, the initial ligand chosen was a ferulic acid associated to a CH_3 terminal (FA-CH_3).

The procedure to achieve a suitable catalytic pocket for both structures was initiated by docking the FA-CH_3 in *G. cingulata* structure (PDB ID: 3dea). This crystal structure was obtained with a complexed ligand which comprises of an aromatic ring and a scissile carbon bound to a double bond oxygen, same as the chosen starting ligand. After docking of the FA-CH_3 to 3dea template, the coordinates of the docked ligand were dragged to both *T. terrestris* and *F. solani* receptor structures. Each receptor complexed with the starting ligand was prepared again using the Prepwizard module. This time, het states of the docked FA-CH_3 were generated using Epik at pH (7.0 ± 2.0). Afterwards, the complexed receptors were subjected to energy minimization to readjust the starting ligand in each of the catalytic pockets.

3.2.4 Receptor Grid Generation

Receptor grid boxes are designed to determine the volume of the enzyme in which the docking of each ligand pose will be calculated.

For docking of the feruloyl esters in both *T. terrestris* and *F. solani* structures, two different grids were generated, both centered on the catalytic serine of the cutinases. One was made smaller for substrates with C_2 to C_8 aliphatic domains and one sized bigger for substrates with C_{10} to C_{18} aliphatic domains. Hydrogen bonds between the amides and oxygens of the oxyanion hole residues were constrained in both grids and NOE (spatial) constraints of 2.0 Å around the scissile carbon of the starting complexed ferulic acid were also incorporated in the bigger sized box. Catalytic serine was obliged to rotate in both grids. The receptor grid settings used in the docking of each ligand to both cutinases are given in Table S2.

For docking of the products in *T. terrestris* cutinase, a receptor grid was designed for every structure complexed with the each docked feruloyl ester. A NOE (spatial) constraint of 0.5 Å was incorporated around the single bond oxygen of the ester group of each docked ligand.

3.2.5 Ligand Docking

Docking of the feruloyl esters to *T. terrestris* and *F. solani* cutinases was set using Glide module.

Flexible docking with Glide Standard precision (SP) protocol was performed for all designed and prepared feruloyl esters, to predict their best binding pose in both cutinases. The constraints checked in each docking test are present in Table S2. In this procedure, intramolecular hydrogen bonds were always rewarded, and planarity of pi conjugated groups was always enhanced.

In each test, Glide generated thousands of poses for each docked ligand and the incorporated results were filtered using the defined constraints. Poses were ranked according to Emodel value and not according to the GlideScore or the overall docking score.

For docking of products in *T. terrestris* cutinase, the same procedure was applied, however only one constraint was checked: the oxygen of the hydroxyl group of the products was committed to stay within 0.5 Å of the correspondent atom of the feruloyl ester, which was spatially constrained when generating the receptor grid boxes.

3.2.6 Binding Energies Calculation

The binding energy values of both feruloyl esters and correspondent products were obtained using the MM-GBSA module, a Prime/Glide tool. This module allowed energy minimization of the complexed receptor and calculation of the binding energies of each docked ligand.

4. Results and Discussion

Understanding the capability of *T. terrestris* cutinase for degrading substrates as complex and dense as suberin requires the previous study of the relevant structural-functional features of cutinases: the binding cleft and the catalytic machinery.

Binding cleft: As occurs in *F. solani* cutinase (see section 2.3.2), structurally, all fungal cutinases display a set of helixes surrounding a central beta-sheet of five parallel strands, each pointing towards the binding cleft. The binding groove is enclosed by hydrophobic loops which are responsible for the capability of this family of enzymes of degrading substrates with long aliphatic fractions (Roussel et al., 2014). Hence, a larger binding groove is expected on cutinases which can welcome bulkier hydrophobic ligands. Moreover, after collection of data obtained from electron relaxation and NMR studies performed on *F. solani* cutinase, and determination of b-factors (or temperature factors) of several cutinases, evidence supports the considerable mobility of the binding loops of these enzymes (Figure S1).

Catalytic machinery: As it is displayed in *F. solani* cutinase (see section 2.3.2), cutinases are also characterized by their serine-histidine-aspartic acid catalytic triad and the oxyanion hole. Generally, the catalytic serine is exposed to the solvent, opposing to true lipases, which are characterized by an interfacial activation consisting of the unfolding of a lid covering the active site. This lid has been associated to an N-terminal extension connected to the core structure of lipases through a long loop (Soni et al., 2019).

During catalysis, the exposed catalytic serine links to the carbonyl group of the ester being hydrolyzed (Chen et al., 2013). In these first steps of the reaction, the catalytic histidine deprotonates the serine (Rauwerdink & Kazlauskas, 2015). Additionally, during the whole mechanism, the catalytic aspartic acid stabilizes the histidine through hydrogen bond interactions (Rauwerdink & Kazlauskas, 2015). Hence the pair interacting catalytic residues (Ser-His; Asp-His) should be within a 3Å reach of each other during catalysis, which is the standard hydrogen bond length.

Furthermore, for catalysis to properly occur, the transition state needs to be stabilized by at least two hydrogen donors (Rauwerdink & Kazlauskas, 2015). Generally, the oxyanion key residues consist of two main chain amides, one being from the residue following the catalytic

serine (Rauwerdink & Kazlauskas, 2015). For example, *F. solani* cutinase displays two amides as hydrogen donors, one from Ser42 and one from Gln121 (see section 2.3.2). Nonetheless, one possible variation in the oxyanion hole of cutinases is a third hydrogen bond donor, which occurs in *G. cingulata* cutinase (Nyon et al., 2009) and lipase B from *Candida antarctica* (Rauwerdink & Kazlauskas, 2015).

4.1 Homology Modelling

Considering that no crystallographic structure of *T. terrestris* cutinase has been deposited, building a suitable model for the enzyme was required.

Therefore, seven different homology models of *T. terrestris* cutinase were built using four different tools: SWISS-MODEL server (Biozentrum, 2020), I-TASSER server (Lab, Zhang, 2020), PHYRE 2 server (Structural Bioinformatics Group, 2020) and Prime module from Maestro 12.3 (Schrödinger Release 2020-1). The alignment of the models with the respective homologous cutinase templates are present in Figure S2 and the information on the evaluating parameters of the templates used for each model, such as overall homology score, percentage identity, coverage and X-ray resolution, is given in Table S1.

The conscious decision of the most suitable model for *T. terrestris* cutinase considered two main factors: the conformation of the N-terminus of the enzyme and the disposition of its catalytic residues in each model.

The analysis starts with the first factor. Figure 5 shows all homology models built, with their characteristic N-terminus conformation highlighted. Briefly, evidence found in this work shows that the N-terminus region of *T. terrestris* structure may display an active participation in the functional mechanism of the enzyme. Therefore, all homology models which displayed a non-functional N-terminus domain were instantly excluded. A detailed discussion of these findings and decisions is described next.

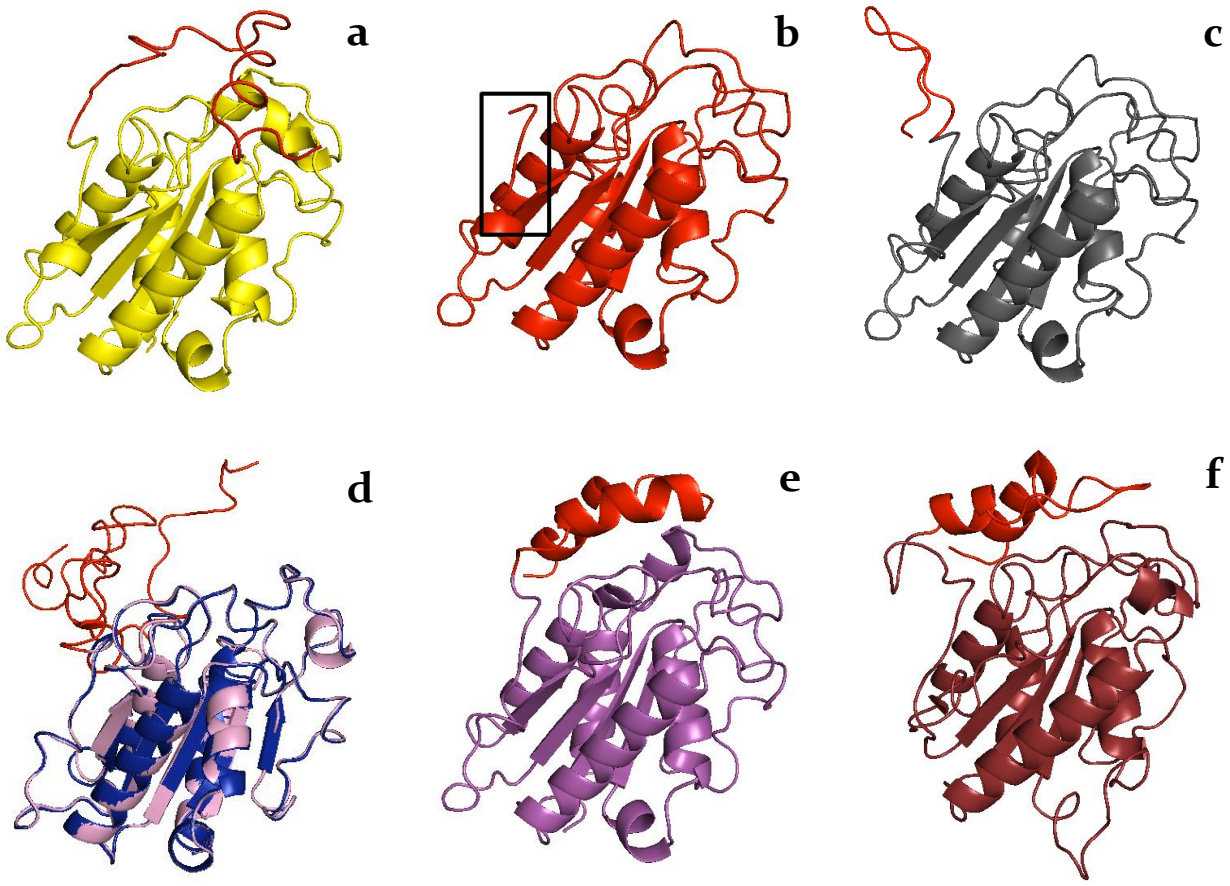

Figure 5. *Homology models of* T. terrestris *cutinase with red signaled N-terminus.* ***a.*** *Phyre non refined model.* ***b.*** *Swiss model.* ***c.*** *Prime 1 model.* ***d.*** *Prime 2 (blue) and Prime 3 (light pink) models.* ***e.*** *iTasser model.* ***f.*** *Prime 4 model.*

The Phyre model (Figure 5a) shows a highly unreliable N-terminus loop. Swiss model (Figure 5b), Prime 1 model (Figure 5c), Prime 2 and Prime 3 models (Figure 5d) present a non-functional N-terminus loop. Only iTasser model (Figure 5e) and Prime 4 model (Figure 5f) display a complete functional N-terminus region, comprising of a precise helix-like structure.

Phyre model was built from five crystallographic cutinases from different microorganisms: *G. cingulata* (PDB ID: 3dd5), *Humicola insolens* (PDB ID: 4oyl), *F. solani* (PDB ID: 1cex), *Aspergillus oryzae* (PDB ID: 3gbs) and *M. cinnamomea* (PDB ID: 5x88).

The position of its N-terminal domain near the binding cleft was the first indicium of a possible active role of this region in the functional mechanism of *T. terrestris* cutinase. Arguments in favour of this hypothesis were developed after analysis of the confidence level of the secondary structure of the model. Briefly, the N-terminus residues 5 to 14 were confidently presented as forming a helix figure (Figure S3), which was then confirmed after refinement of the model (Figure S4).

In light of the unraveled helix configuration close to the binding cleft presented in this model, the initial hypothesis was not discarded. Therefore, Swiss model was excluded, as it deleted the N-terminus of the sequence (Figure 5b), as was also the Prime 1 single template model, which concepted an N-terminus loop folding inward (Figure 5c). Attention should be taken to the fact that both Swiss and Prime 1 models shared the same homologous template, a cutinase from *G. cingulata* (PDB ID: 3dcn), the closest cutinase to *T. terrestris* with a sequence identity of ~58%. This reveals that two different homology modelling tools can design different models for the same target sequence using the same crystallographic template structures, by using different alignment algorithms.

Since the N-terminus loop/helix of *T. terrestris* cutinase could not be properly modelled by neither SwissModel server, Phyre2 server or Prime module, there was reasonable doubt over the chosen templates by the three different homology modelling tools.

Therefore, a quick run-through over the results of Prime BLAST homology search was carried out, as its interface provides a clear real-time check on multiple sequence alignments. A new goal was set which consisted in finding templates with longer N-terminus regions that could possibly match the N-terminus of *T. terrestris* cutinase. A negative control is given in Figure S5, which presents the failed alignment between the target sequence and the 3dcn template from *G. cingulata*, specifically in the N-terminus region. Upon this, a trial alignment between the target sequence and the multiple highest scored templates chosen was performed and is given in Figure S6. This procedure was unsuccessful since none of the templates displayed a matching N-terminus region. Nonetheless, two multi-template consensus models, Prime 2 and Prime 3, were built using these selected templates. As expected, both presented non-functional N-terminus loops (Figure 5d) thus were ruled out. Detailed information on the templates used for each consensus model are given in Table S1, Figure S6.

The iTasser model defined a functional N-terminus appendix (Figure 5e) since it runs high quality iterative template-based fragment assembly simulations. Consequently, two of its threading programs encountered one single crystallized cutinase that presented a longer N-terminus region, belonging to *Trichoderma reesei* cutinase (PDB ID: 4psc) (Figure S7). This structure presented a lower sequence identity (~30%) comparatively to other identified templates (~50%) (Table S1). This fact explained the difficulty in identifying this structural

template when searching through Prime BLAST search results for the building of the consensus models.

Furthermore, Phyre2 server had also identified one of *T. reesei* crystallographic structures as a possible structural template (PDB ID: 4psd), which presented the highest coverage percentage (~95%) despite its overall lower sequence identity (~26%) (Table S1). Still, the server did not model the N-terminus of the target sequence through homology modelling using *T. reesei* as the template structure. Instead, the server resourced to *ab initio* techniques to achieve this task.

Aligning both Phyre and iTasser models, differences were observed not only in the conformation of the two modelled domains but also in their placement. Accordingly, iTasser model defines the N-terminus region more precisely, presenting two helixes positioned over the binding cleft, connected by a loop structure which promotes the flexibility of this region (Figure S8). This conformation endorsed the possibility of an existing lid covering the active site in *T. terrestris* cutinase, a characteristic natural in true lipases. This hypothesis was later confirmed by the reported lid existing also in *T. reesei* cutinase (Roussel et al., 2014), the highest scored template of the iTasser model (Figure S9).

As previously stated, different homology modelling tools can build different models for one target sequence using the same template structures. Bearing this in mind, another homology model was built using Prime module, selecting the cutinase from *T. reesei* (PDB ID: 4psc) as the single template structure. Prime 4 could properly model the N-terminus conformation of *T. terrestris* cutinase (Figure 5f) by also designing a lid covering the binding cleft.

Hence, considering the evidence of a functional N-terminus region in *T. terrestris* cutinase, the first step of the decision was completed with the remaining Phyre, iTasser and Prime 4 homology models still competing. iTasser and Prime 4 modelled more precisely the N-terminus of the target sequence, burying the catalytic machinery under a flexible lid. However, the most suitable model requires a correct arrangement of the well-known catalytic triad since no activity would be possible otherwise. Therefore, aligning each model with their corresponding templates was crucial to determine the catalytic residues of *T. terrestris* cutinase. Accordingly, *T. terrestris* cutinase displays a catalytic triad comprising of Ser136-His188-Asp191. Figure 6 shows all remaining homology models aligned with one of their templates, with the respective catalytic triad signaled.

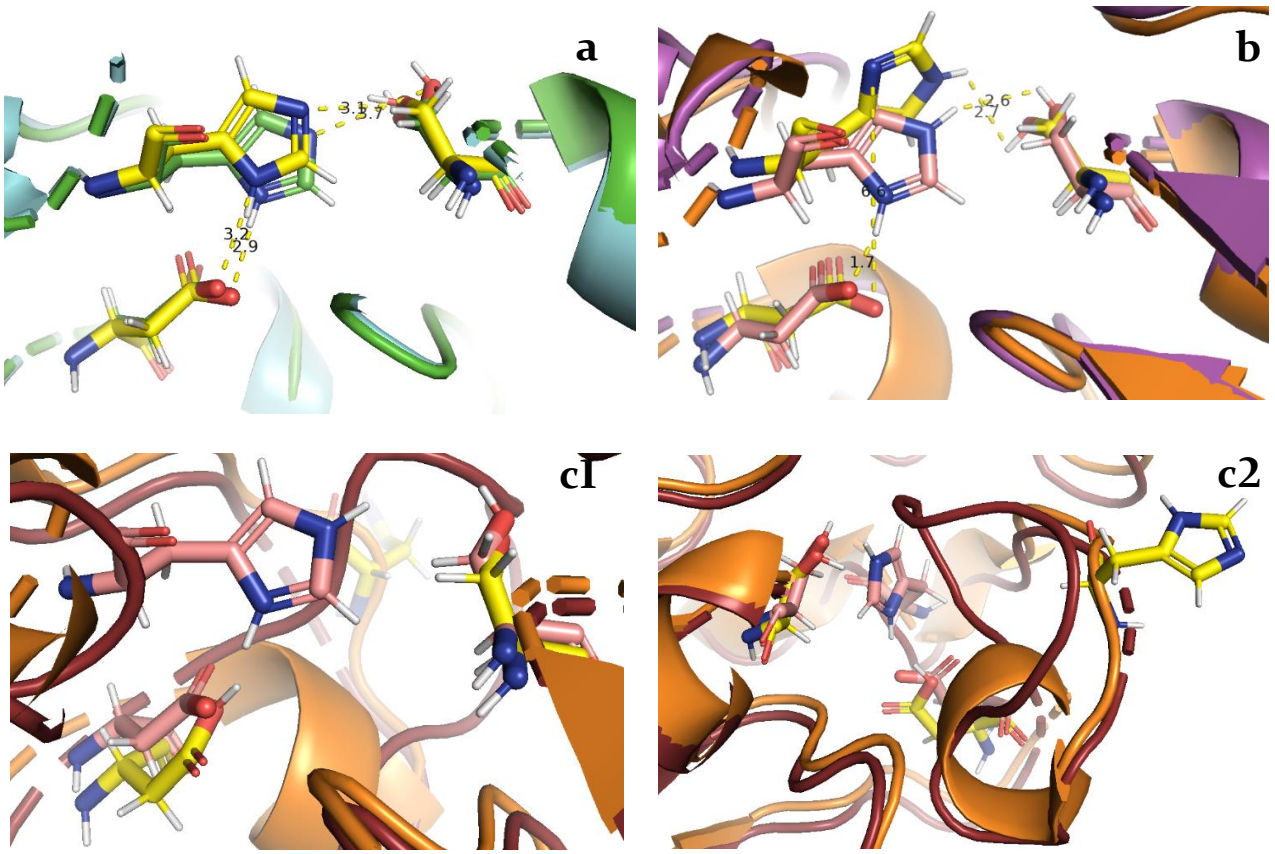

Figure 6. *Catalytic residues arrangement in* T. terrestris *cutinase homology models. Distances in Å.* ***a.*** *Phyre model (green) aligned with* F. solani *template structure (PDB ID: 1cex). Active site residues coloured by element with custom carbons coloured yellow (Phyre) and green (1cex).* ***b.*** *iTasser model (magenta) aligned with* T. reesei *template structure (PDB ID: 4psc). Active site residues coloured by element with custom carbons coloured yellow (iTasser) and salmon (4psc).* ***c1, c2.*** *Prime 4 model (ruby) aligned with* T. reesei *template structure (PDB ID: 4psc). Active site residues coloured by element with custom carbons coloured yellow (Prime 4) and salmon (4psc).*

The catalytic residues of Phyre model exhibited a good alignment to the homologous residues of the template cutinase from *F. solani*, the most well characterized cutinase so far (Figure 6a). Alignments between the target Phyre model and other templates, specifically from *M. cinnamomea* and *G. cingulata* are present in Figure S10 and Figure S11, respectively. Both also revealed matching catalytic residues, except for the catalytic histidine from *G. cingulata* cutinase. This residue adopts an unusual configuration being swung out of the active site into a position where it is unable to participate in catalysis. However, this position in *G. cingulata* cutinase has been reported by Nyon et al. (2009). In this study, based on site-directed mutagenesis, the authors confirmed that the catalytic histidine is essential for the catalytic cycle, suggesting that the loop has to go through significant conformational changes for the residue to participate in catalysis.

Despite initial focus on the iTasser and Prime 4 models, due to their successful disposition of a functional N-terminus domain, these two models were later discarded considering the configuration of the catalytic histidine. As described above, the pair interacting catalytic residues (Ser136-His188; Asp191-His188) should be within a 3Å reach of each other during catalysis, which is not fulfilled in either the iTasser or the Prime 4 model. iTasser model presented this residue shifted from the catalytic aspartic acid (Figure 6b) and Prime 4 model exhibited this residue too far off from the expected catalytic pocket (Figure 6c). The possibility of His204 of iTasser model shifting towards Asp191 was considered, however quickly ruled out, since this residue is positioned in a helix structure of the enzyme, which does not display as much flexibility as a loop configuration would (Figure S12).

Furthermore, the catalytic groove in the iTasser model is not as predominant as in the Phyre model (Figure S13). As *T. terrestris* cutinase has been reported to hydrolyze substrates with longer aliphatic fractions (Duan et al., 2019), a larger binding groove is expected in its structure.

In view of the reported discoveries, the most suitable homology model for *T. terrestris* cutinase was the Phyre model, shown in Figure 7, as it presented the correct arrangement of the catalytic residues, a larger catalytic groove, and a relatively acceptable N-terminus conformation.

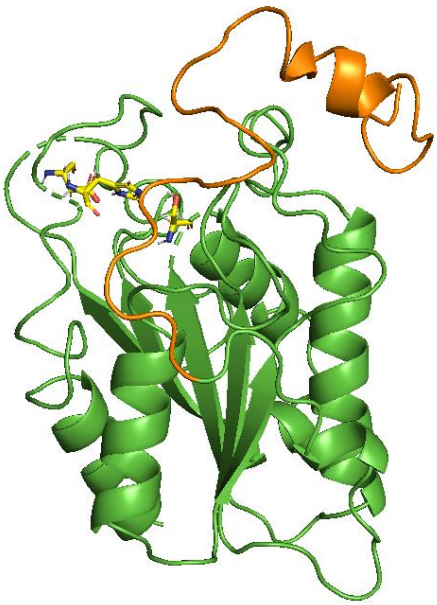

Figure 7. T. terrestris *cutinase model chosen. The refined N-terminus region is coloured in orange. The active site residues are displayed in sticks coloured by element with custom carbons coloured yellow.*

4.2 Docking Analysis

Docking analysis gives information on the most favourable position of a ligand in the enzyme pocket based on the number of intermolecular interactions within the complex formed, such as hydrogen bonds and hydrophobic contacts. Therefore, the most suitable complexes are predicted based on the free energy of binding of the ligand. More information can be found in Meng et al. (2011).

4.2.1 Choosing a Substrate

Several esterified compounds were considered for the target substrate to obtain a realistic study of the interactions between suberin and cutinases. However, docking tools only enable the generation of favourable poses of a candidate ligand for targeting of a single ester group. Therefore, the model substrate selected for docking to the *T. terrestris* cutinase was a suberin oligomer with one ester group, a feruloyl ester as described in section 2.2. The chosen feruloyl ester comprised of a stearyl alcohol (octadecan-1-ol) esterified to a ferulic acid. This molecule displays a long aliphatic moiety. Hence, to overcome possible steric hindrance issues, feruloyl esters with successively longer aliphatic fractions were docked, specifically with C_2, C_4, C_6, C_8, C_{10}, C_{12}, C_{14}, C_{16}, C_{18} chains. The ligands are represented by the following nomenclature: FA-C2, FA-C4, FA-C6, FA-C8, FA-C10, FA-C12, FA-C14, FA-C16, FA-C18, respectively. As an example, two of the designed ligands are given in Figure S14.

4.2.2 Identifying the Oxyanion hole

To determine the oxyanion residues of *T. terrestris* cutinase, the closest homologous cutinase from *G. cingulata* (PDB ID: 3dea) was analysed (Nyon et al., 2009). *G. cingulata* cutinase was crystallized covalently bound to a PETFP inhibitor (3-phenethylthio-1,1,1-trifluoropropan-2-one), which has a similar structure as one of the target ligands, FA-C2. Figure S15 shows that both ligands (PETFP and FA-C2) display the carbonyl oxygen occupying the oxyanion hole.

Structural alignment between *G. cingulata* and *T. terrestris* cutinases revealed that Ser58 and Gln137 form the oxyanion hole in *T. terrestris* cutinase.

A docking methodology for the cutinase of *T. terrestris* was then developed as it is described in section 3.2, comprising of model refinement, ligand preparation, docking of a starting ligand, generation of a receptor grid and application of docking constraints. This last step is discussed next.

4.2.3 Docking Constraints

When performing molecular docking, Glide generates several possible conformations and orientations for a target ligand. Hence setting constraints based on acknowledged receptor-ligand interactions is required to screen out poses that do not meet the catalytic and binding mechanism of cutinases early on in their evaluation for docking suitability.

As described above, a correct ligand pose involves hydrogen bond interactions with the oxyanion residues as well as the proximity between the catalytic serine and the scissile carbon. Thus, the feruloyl esters were docked to *T. terrestris* cutinase requiring their respective carbonyl oxygens to be interacting with the oxyanion residues. Also, the carbonyl carbons of FA-C10 to FA-C18 were assigned to be placed within interacting distance of the catalytic serine. The need to set positional constraints for ligands with longer aliphatic chains discloses the difficulty in obtaining an active and functional binding mode for highly hydrophobic molecules. Therefore, there is evidence that the hydrophobicity of the longer aliphatic chains is responsible for steric hindrance issues, which renders the position of the ligand's ester group in the catalytic pocket of the receptor more difficult. Docking constraints are summarized in Table S2.

Challenges in finding the right constraints were caused by the sensitivity of the Glide algorithm, where small spatial changes in residues resulted in a complete shift in the ligand pose. Furthermore, to allow the ligand to bind, and to understand which residues spatially limited the ligand taking its position in the cleft, each hydroxy and thiol group had to be rotated individually, and the effect on the binding pose observed.

Though the application of constraints was difficult, FA-C2 to FA-C18 were docked successfully in the *T. terrestris* cutinase model.

4.2.4 Docking Results

Figure 8 shows the most reliable pose encountered for FA-C18 in *T. terrestris* cutinase, the stabilizing oxyanion hole and the support of the binding groove. The binding poses for the other docked feruloyl esters are given in Figure S16 - Figure S23.

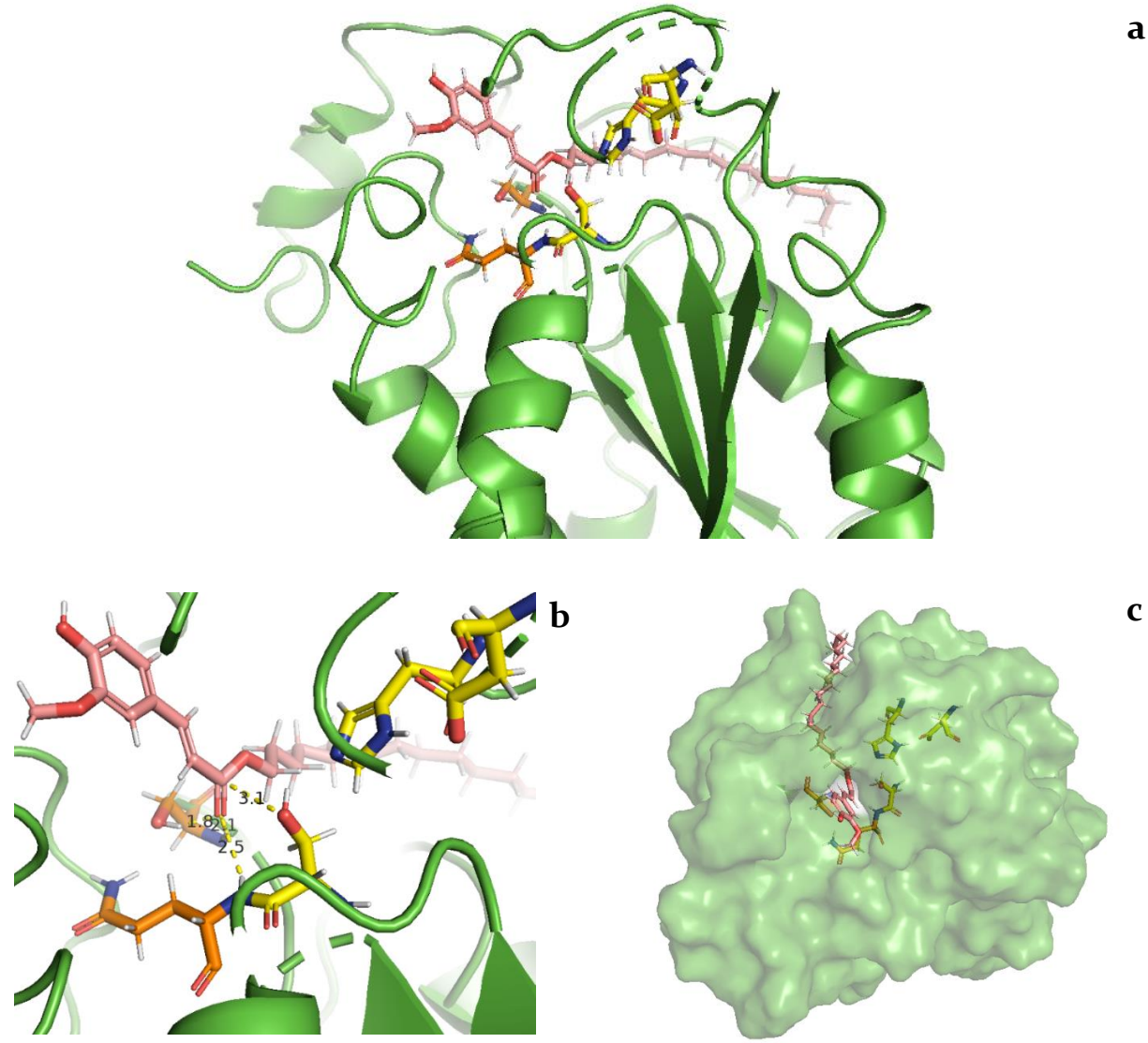

Figure 8. *The most reliable binding pose for FA-C18 in* T. terrestris *model.* ***Active site and oxyanion hole residues show in sticks coloured by element with custom carbons coloured yellow and orange, respectively. FA-C18 represented in sticks coloured by element with salmon custom carbons. a.*** *Model represented in green cartoon figure. FA-C18 is docked.* ***b.*** *Model represented in green cartoon figure. The aromatic moiety of the feruloyl ester is placed in the oxyanion cavity within interacting distance of the catalytic serine (3.1 Å). The distances between the carbonyl oxygen and the oxyanion residues are also displayed in Å and are also represented by yellow dashes.* ***c.*** *Model represented in green surface figure. The aliphatic fraction of FA-C18 is displayed throughout the binding tunnel of* T. terrestris *model.*

After encountering the most reliable poses for each ligand in the *T. terrestris* model, the binding energy of each feruloyl ester was calculated using the Prime MM-GBSA module. These values account for the binding free energy once the ligand-receptor complex is formed, meaning the lower the energy value given, the energetically more favorable the pose is. The term 'binding affinity' will be used in this report to specify the strength of the intermolecular interactions between a complexed ligand and the receptor. Also, the increment or reduction of the values of free binding energy is discussed regarding the module value.

Table 2 shows the docking results for each ligand, from FA-C2 to FA-C18. The following table presents the distances between the carbonyl carbon of each docked ligand and the catalytic serine (Distance (Ser136)), the oxyanion residues within interacting distance (3 Å) of the ligand (oxyanion residues) and the simulated binding energies. The sensitivity of the binding energy is 1 Kcal/mol (Schrödinger, 2016). The experimental specific activities obtained from Duan et al. (2019) are also shown. These experimental data where retrieved using pNP as substrates, molecules structurally similar to the target ligand.

Table 2. *Docking results of FA-C2 to FA-C18 of* T. terrestris *cutinase.*

	Distance (Ser136) (Å)	Oxyanion residues	Binding energy (Kcal/mol)	Specific activity (U/mg)
FA-C2	4.16	Ser58 (N)	-46.69	266.2 ± 4.5
FA-C4	4.11	Ser58 (N)	-53.10	2322.4 ± 17.8
FA-C6	3.95	Ser58(N)	-57.81	1056.4 ± 18.8
FA-C8	3.05	Ser58(N); Ser58(O); Gln137(N);	-44.16	1043.1 ± 5.8
FA-C10	3.14	Ser58(N); Ser58 (O);	-48.27	1262.3 ± 8.7
FA-C12	3.27	Ser58(N); Ser58(O); Gln137(N);	-50.72	1257.1 ± 1.4
FA-C14	3.48	Ser58(N); Ser58(O);	-62.52	880.7 ± 7.2
FA-C16	3.16	Ser58(N); Ser58(O); Gln137(N);	-54.93	412.6 ± 15.2
FA-C18	3.06	Ser58(N); Ser58(O); Gln137(N);	-69.12	---

The results point to the stronger stabilizing force of the oxyanion pocket when testing from FA-C8 onwards, as the ligands interact with more than one hydrogen donor. The oxyanion hole even gains a third donor when docking FA-C8, FA-C12, FA-C16 and FA-C18.

However, the hydrogen interactions within the catalytic pocket do not seem to be the single energy contribution to the total binding energy, as a higher binding energy is not always supported by an increase in the oxyanion hydrogen donors and vice-versa (for example from FA-C6 to FA-C8 and from FA-C12 to FA-C14). Therefore, the intermolecular interactions between the aliphatic domains of the feruloyl esters and the residues enclosing the binding cleft seem to contribute to the calculated binding energy. This is a good indicator on the extent of conclusions one can draw with molecular docking procedures for long-chain ligands, as will be discussed later in this section.

Comparing experimental specific activities with simulated binding energies, the results follow the same trend for ligands with short and middle-chain aliphatic lengths. Specifically: from FA-C2 to FA-C4, and again from FA-C8 to FA-C12, both binding energy and activity are increasing, and from FA-C4 to FA-C8, both binding energy and activity decrease. From FA-C12 onwards, several reasons might support the observed disparage between the two parameters since low specific activities are correlated to high binding affinities. To explain this, two main hypotheses were postulated:

1. The local intermolecular interactions between the aliphatic tails of the target ligands and the residues enclosing the binding tunnel of the *T. terrestris* cutinase have a significant contribution in the calculated free binding energy. Hence, for long-chain ligands, a high value of binding energy masks the low interaction energy within the catalytic pocket of the target structure, which is the main responsible for the low activity of the enzyme.

2. A strong binding of the aliphatic fractions of the substrates to the target receptor difficults their release once reaction is completed (Kakaei et al., 2019). Therefore, no new molecules can enter the target structure to start a new degradation cycle. Hence the ester-cleaving rate of the enzyme decreases as does its activity.

Hypothesis 1 and 2 were analyzed by studying the contribution of the aliphatic chain of the substrates to the total binding energy. To achieve this, the docking of products was performed since these consist of the aliphatic alcohols without the esterified ferulic acids. The aim was to mimic the ester group cleavage of all substrates in *T. terrestris* cutinase prior to the release of the product. This was achieved by committing the hydroxyl groups of the products to a 0.5 Å distance of the correspondent atoms in the respective substrates. Figure 9 shows the docked stearyl alcohol (octadecan-1-ol) aligned with its correspondent substrate, FA-C18. The poses for the other docked products are given in Figure S24.

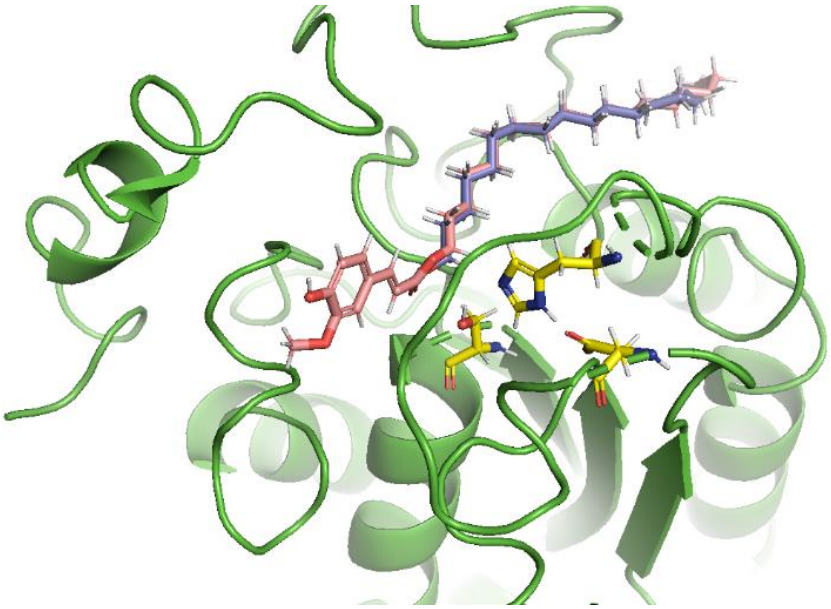

Figure 9. *Docking of FA-C18 and correspondent product in* T. terrestris *cutinase.* T. terrestris *model represented in green cartoon figure. Active site residues show in sticks with custom carbons coloured yellow. FA-C18 substrate and correspondent product represented in sticks coloured by element with salmon and blue custom carbons, respectively.*

The binding energies of each docked product were then calculated using Prime MM-GBSA module. 'dGsubstrate – dGproduct' represents the difference between the binding energy of the feruloyl esters calculated previously and the correspondent products. As a product is composed only of the same aliphatic domain of its correspondent substrate, the calculated 'dGsubstrate – dGproduct' can represent the contributing energy factor of the aromatic domain of a substrate. Results are given in Table 3.

Table 3. *Docking of products. The binding energy of the docked products with the correspondent C-chains is showed. The binding energies obtained previously for the correspondent substrates are also present as the experimental specific activities. The calculated difference between the binding energy of the substrates and products (dGsubstrate-dGproduct) is also given.*

	Binding energy of substrate (Kcal/mol)	**Binding energy of product (Kcal/mol)**	**dGsubstrate – dGproduct (Kcal/mol)**	**Specific activity (U/mg)**
C2	-46.69	-13.74	-32.95	266.2 ± 4.5
C4	-53.10	-18.83	-34.27	2322.4 ± 17.8
C6	-57.81	-19.17	-38.64	1056.4 ± 18.8
C8	-44.16	-27.84	-16.32	1043.1 ± 5.8
C10	-48.27	-33.42	-14.85	1262.3 ± 8.7
C12	-50.72	-34.34	-16.38	1257.1 ± 1.4
C14	-62.52	-39.71	-22.81	880.7 ± 7.2
C16	-54.93	-33.46	-21.47	412.6 ± 15.2
C18	-69.12	-36.57	-32.55	---

The binding energy of the products increases with increasing chain-lengths, stabilizing for long-chain products. Therefore, results show that products bind more tightly to the target cutinase as their chains increase their lengths, for short and middle chain products (C_2 to C_{10}). This can be translated to the binding affinity of the substrates, as the aliphatic chain is the same. However, determining the contribution of the long hydrophobic tails in the total binding energy is still necessary to promote understanding over the veracity of Hypothesis 1 and 2.

Regarding Hypothesis 1 – The analysis of 'dGsubstrate – dGproduct' values reveals that those are higher for short and long-chain substrates (C_2 to C_6 and C_{14} to C_{18}). Therefore, the interactions of the aromatic fractions of short and long-chain substrates have a stronger dominant contribution in the total binding energy as compared to the aliphatic fractions. Hypothesis 1 is not supported then, as there is no masking effect of the interactions of the aliphatic chains of long-chain ligands over the interactions within the catalytic pocket of *T. terrestris* cutinase.

Regarding Hypothesis 2 - Excluding the product with a C_{14} chain, the free energy of binding of the products with longer aliphatic chains does not increase, it stabilizes around -35 Kcal/mol. Therefore, Hypothesis 2 is not supported by these findings, as the loss of activity for long chain ligands cannot be correlated with their increasing binding to the receptor.

As none of the two hypotheses postulated were confirmed, there are no structural evidence that support the decaying activity of the *T. terrestris* cutinase for long chain pNP, which confirms the reported industrial relevance of this cutinase for polyester degradation.

Even though molecular docking techniques are normally used for study of shorter ligands, the successful results obtained when docking longer ligands in this cutinase seem to indicate the promising application of this approach in the discovery of industrially relevant cutinases for polyester degradation. However, docking of more structures is advised to infer over the suitability of the method for polyester-cutinase interaction studies and preliminary determination of structural-functional characteristics of cutinases.

4.3 Comparison with Homologous Cutinases

To verify the above stated findings, comparison of docking results with kinetic literature data was performed with structural templates of *T. terrestris* model, specifically the cutinases from *F. solani* (PDB ID: 1cex) and *M. cinnamomea* (PDB ID: 5x88).

First, the specific activities for *M. cinnamomea* and *F. solani* cutinases were taken from Duan et al. (2017) and Ping et al. (2017), respectively. *F. solani* and *M. cinnamomea* cutinases are reported to have a lower activity against the same substrates than *T. terrestris* cutinase (see Table S3), thus being less suitable for degradation of polyesters. *F. solani* cutinase displays low activity for all pNP tested. *M. cinnamomea* shows a different behaviour: the activity is high for pNP with short chain lengths; however, it instantly decreases when assaying pNP with middle to long chain lengths. Additionally, *T. terrestris*, *F. solani* and *M. cinnamomea* cutinases belong to different clans in the phylogenetic tree (Figure 3*)*. Hence, structural differences may exist between these three cutinases which may provide understanding over their different activities.

Docking of *F. solani* cutinase was performed to understand which structural characteristics of this enzyme were inhibiting its activity. *F. solani* displays the Ser120-His188-Asp175 as the catalytic triad (Longhi et al., 1997) and the residues Ser42 and Gln121 as the oxyanion residues (Chen et al., 2013).

The docking was performed using the same constraints as for the *T. terrestris* cutinase. In all but one case (FA-C14) this resulted in successful docking results. Binding energies were calculated also. The docked feruloyl esters are present in Figure S25 - Figure S32. Again, the ferulic acid of the ligands stays within the catalytic pocket and the aliphatic tail goes through the binding tunnel. Table 4 shows docking results for *F. solani* cutinase.

Table 4. *Docking results of FA-C2 to FA-C18 of* F. solani *cutinase. The distances between the carbonyl carbon of each docked ligand and the catalytic serine (Distance (Ser120)), the oxyanion residues within interacting distance (3 Å) of the ligand (oxyanion residues) and the simulated binding energies are shown.*

	Distance (Ser120) (Å)	**Oxyanion residues**	**Binding energy (Kcal/mol)**
FA-C2	3.45	Ser42 (N)	-36.28
FA-C4	3.56	Ser42 (N)	-42.08
FA-C6	4.28	Ser42 (N)	-46.32
FA-C8	3.65	Ser42 (N)	-37.82
FA-C10	3.53	Ser42 (N)	-50.32
FA-C12	3.54	Ser42 (N)	-45.46
FA-C14	Not docked	Not docked	Not docked
FA-C16	3.53	Ser42 (N)	-52.66
FA-C18	3.86	Ser42 (N)	-34.99

Analysis of Table 4 shows that the binding energies for each docked ligand are lower for this cutinase when compared to the results obtained for *T. terrestris* cutinase (see section 4.2.4). The lower binding energy is associated to a weaker binder, which can be correlated with the overall inferior activity of *F. solani* cutinase to degrade all pNP substrates comparative to *T. terrestris* cutinase.

The most relevant binding residues in *F. solani* cutinase are Leu182, Asn84 and Ala85, which enclose the binding cleft at the 'top' (Figure S33). Indeed, these residues are responsible for the conformation of the binding cavity. For example, mutational studies to promote a larger binding groove of this cutinase have been carried out by replacing Leu182 to Gly182 since this residue is smaller (Longhi et al., 1996). Additionally, the relevant binding residues (Leu182, Asn84 and Ala85) of *F. solani* cutinase are perfectly aligned with the homologous residues of *T. terrestris* cutinase (Figure S33). Although this does not explain the differences in the activity of the two cutinases, this clearly highlights engineering potential to increase the pocket in *T. terrestris* cutinase.

However, a possible structural characteristic that may explain the weaker binding of ligands in *F. solani* cutinase may consist in the substitution of Phe205 near the catalytic site of *T. terrestris* cutinase for a Leu189 in *F. solani* cutinase. The hydrophobic Phe205 of *T. terrestris* cutinase encloses the aliphatic chain of the complexed ligand. In contrast, in *F. solani* cutinase, it is the aromatic domain which is positioned near Leu189 (Figure S34). However, this structural difference which leads to a reverse ligand position in both cutinases still needs to be evaluated in depth since its existence alone does not seem to fully explain the lower activity revealed by *F. solani* cutinase.

Simulated evidence reveals that *F. solani* cutinase never achieved the total oxyanion hole stabilization, opposite to what has occurred in *T. terrestris* cutinase (see section 4.2.4). This may be explained by the fact that the crystal structure just reflects one position in the entire catalytic cycle, hence the disposition of the oxyanion residues in that moment negatively influenced the docking results. Since molecular docking does not account for protein mobility, this can be a limitation when exploring other crystallized structures.

Regarding the *M. cinnamomea* cutinase, structural differences were encountered when comparing its crystallized structure with *T. terrestris* model and *F. solani* template, which may explain its decaying activity for substrates with longer chain lengths.

Figure S35 reveals the presence of a smaller binding cleft in the *M. cinnamomea* cutinase. The gatekeeper residues (Leu73 and Leu176) are closer than the respective homologous residues in *T. terrestris* cutinase. Additionally, Ser34 is displaced from the classical position predicted by *F. solani* and *T. terrestris* cutinases, narrowing the binding cleft.

In light of these findings, docking of short and middle chain ligands was performed with the *M. cinnamomea* cutinase to understand the influence of the Ser34 in the capability of the enzyme of accepting bulkier substrates. As shown in Figure S36, no successful pose was achieved, indicating that the ligand cannot access the active site.

This steric hindrance issue of *M. cinnamomea* has been reported in Duan et al. (2017) to explain its preference for short-chain substrates. However, in this work, when comparing *M. cinnamomea* to *T. terrestris* cutinase, structural evidence shows that Ser34 is homologous to Ser58, the oxyanion residue of *T. terrestris*, as is shown in Figure 10.

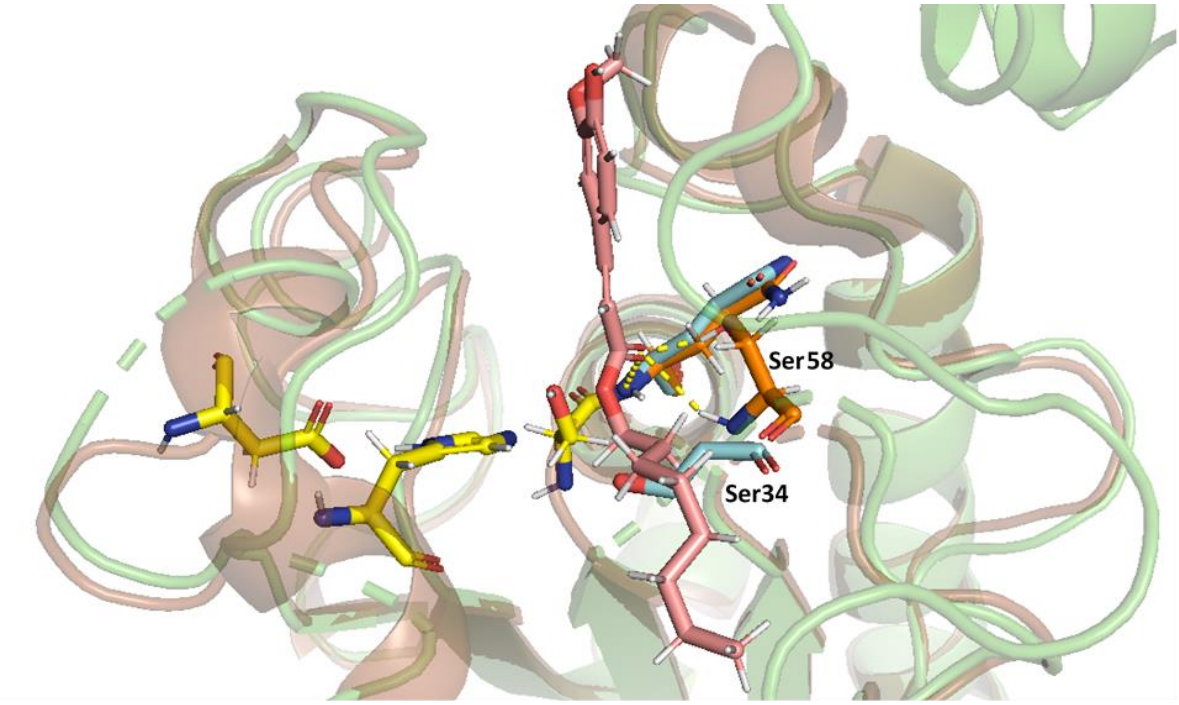

Figure 10. *Ser34 of* M. cinnamomea *cutinase is homologous to Ser58 of* T. terrestris *cutinase. Ser58 of* T. terrestris *cutinase is one of the oxyanion residues which stabilizes the ligand during catalysis. Hydrogen bonds between* T. terrestris *oxyanion residues and the carbonyl oxygen of one docked feruloyl ester (FA-C8) are represented as yellow dash lines.*

Therefore, new findings reveal that the preference for short-chain substrates of *M. cinnamomea* cutinase can be explained by the unclassical disposition of Ser34 in two ways: by sterically hindering the entrance of longer-chain substrates, as has been reported in Duan et al. (2017), and by the lost stabilization of the oxyanion hole.

5. Conclusions

In this work, the structural-functional features of *T. terrestris* cutinase for polyester degradation were assessed, particularly the catalytic machinery and the binding cavity.

Homology modelling provided insight over the possible functional role of the N-terminus of the query sequence as a flexible lid covering the active site, a characteristic common in lipases. Still, the most suitable model required a big binding cleft and the correct disposition of the catalytic triad, with the catalytic pair His-Asp, His-Ser within interacting distance of each other.

Docking of feruloyl esters with successively longer chain lengths to *T. terrestris* cutinase model supported the importance of both oxyanion hole and binding tunnel in ligand-receptor complexation. Comparison of the free binding energy of the docked feruloyl esters with kinetic experimental data of pNP was performed. A trend was observed in both variables for ligands with short and middle chain ligands. However, for long-chain ligands, strong binding of ligands correlated with low activities of the enzyme.

Docking of products promoted understanding over the contribution of the aliphatic chains of the ligands in the total binding affinity. It was concluded that the ligand-receptor interactions within the catalytic pocket were dominant in long-chain ligands, leading to a proper catalytic mechanism. Additionally, the binding of long-chain products was not impeding the start of new degradation cycles. Hence, no structural feature was hindering the activity of the enzyme, supporting the industrial relevance of *T. terrestris* cutinase.

Comparison of docking results between *T. terrestris* and *F. solani* cutinases revealed that the reverse ligand pose in *F. solani* cutinase may partly explain the lower activity of this enzyme towards pNP. Additionally, the lower activity of *F. solani* cutinase was supported by the obtained lower binding energies.

The decaying activity of *M. cinnamomea* cutinase relative to *T. terrestris* and *F. solani* cutinases was supported by the misplacement of Ser34, which sterically hinders the entrance of long-chain substrates and causes the loss of the stabilization of the oxyanion hole.

6. Future Work

Future work will consist in the biochemical characterization of novel CE5 enzymes of every cluster of the newly built phylogenetic tree presented in the background section of this report. Evaluation of docking results with the experimentally obtained activity data will be performed. Conclusions over structural differences between cutinases from microorganisms present in the different clusters will be determined and correlated with the performance of each enzyme. In the end, the major goal consists in the structural-activity characterization of every clan present in the tree and hopeful identification of the key ones for suberin degradation.

7. References

Andrew Waterhouse, Martino Bertoni, Stefan Bienert, Gabriel Studer, Gerardo Tauriello, Rafal Gumienny, Florian T Heer, Tjaart A P de Beer, Christine Rempfer, Lorenza Bordoli, Rosalba Lepore, T. S. (2018). SWISS-MODEL: homology modelling of protein structures and complexes. *Nucleic Acids Research*, *46*, 296–303. https://doi.org/10.1093/nar/gky427

Araújo, R., Silva, C., O'Neill, A., Micaelo, N., Guebitz, G., Soares, C. M., Casal, M., & Cavaco-Paulo, A. (2007). Tailoring cutinase activity towards polyethylene terephthalate and polyamide 6,6 fibers. *Journal of Biotechnology*, *128*(4), 849–857. https://doi.org/10.1016/j.jbiotec.2006.12.028

Austin, H. P., Allen, M. D., Donohoe, B. S., Rorrer, N. A., Kearns, F. L., Silveira, R. L., Pollard, B. C., Dominick, G., Duman, R., Omari, K. El, Mykhaylyk, V., Wagner, A., Michener, W. E., Amore, A., Skaf, M. S., Crowley, M. F., Thorne, A. W., Johnson, C. W., Lee Woodcock, H., … Beckham, G. T. (2018). Characterization and engineering of a plastic-degrading aromatic polyesterase. *Proceedings of the National Academy of Sciences of the United States of America*, *115*(19), E4350–E4357. https://doi.org/10.1073/pnas.1718804115

Belbahri, L., Calmin, G., Mauch, F., & Andersson, J. O. (2008). Evolution of the cutinase gene family: Evidence for lateral gene transfer of a candidate Phytophthora virulence factor. *Gene*, *408*(1–2), 1–8. https://doi.org/10.1016/j.gene.2007.10.019

Bernards, M. A. (2002). Demystifying suberin. *Canadian Journal of Botany*, *80*(3), 227–240. https://doi.org/10.1139/b02-017

Biozentrum. (2020). *SWISS-MODEL*. https://swissmodel.expasy.org/

Cambillau, C., Longhi, S., Nicolas, A., & Martinez, C. (1996). Acyl glycerol hydrolases: Inhibitors, interface and catalysis. *Current Opinion in Structural Biology*, *6*(4), 449–455. https://doi.org/10.1016/S0959-440X(96)80108-4

Carvalho, C. M. L., Aires-Barros, M. R., & Cabral, J. M. S. (1999). Cutinase: From molecular level to bioprocess development. *Biotechnology and Bioengineering*, *66*(1), 17–34. https://doi.org/10.1002/(SICI)1097-0290(1999)66:1<17::AID-BIT2>3.0.CO;2-F

CAZy. (2020). *CE5*. http://www.cazy.org/CE5.html

Chen, S., Su, L., Chen, J., & Wu, J. (2013). Cutinase: Characteristics, preparation, and application. *Biotechnology Advances*, *31*(8), 1754–1767. https://doi.org/10.1016/j.biotechadv.2013.09.005

Comission, E. (2012). *Energy Roadmap 2050 Energy*. https://doi.org/10.2833/10759

Comission, E. (2020). *Weekly Oil Bulletin*. https://ec.europa.eu/energy/data-analysis/weekly-oil-bulletin_en?redir=1

Duan, X., Jiang, Z., Liu, Y., Yan, Q., Xiang, M., & Yang, S. (2019). High-level expression of codon-optimized Thielavia terrestris cutinase suitable for ester biosynthesis and biodegradation. *International Journal of Biological Macromolecules*, *135*, 768–775. https://doi.org/10.1016/j.ijbiomac.2019.05.173

Duan, X., Liu, Y., You, X., Jiang, Z., Yang, S., & Yang, S. (2017). High-level expression and characterization of a novel cutinase from Malbranchea cinnamomea suitable for butyl butyrate production. *Biotechnology for Biofuels*, *10*(1). https://doi.org/10.1186/s13068-017-0912-z

Ebaid, R., Wang, H., Sha, C., Abomohra, A. E. F., & Shao, W. (2019). Recent trends in hyperthermophilic enzymes production and future perspectives for biofuel industry: A critical review. *Journal of Cleaner Production*, *238*, 117925. https://doi.org/10.1016/j.jclepro.2019.117925

Fett, W. F., Wijey, C., Moreau, R. A., & Osman, S. F. (1999). Production of cutinase by Thermomonospora fusca ATCC 27730. *Journal of Applied Microbiology*, *86*(4), 561–568. https://doi.org/10.1046/j.1365-2672.1999.00690.x

Gandini, A., Pascoal Neto, C., & Silvestre, A. J. D. (2006). Suberin: A promising renewable resource for novel macromolecular materials. *Progress in Polymer Science*, *31*(10), 878–892. https://doi.org/10.1016/j.progpolymsci.2006.07.004

Graça, J. (2015). Suberin: the biopolyester at the frontier of plants. *Frontiers in Chemistry*, *3*(OCT), 62. https://doi.org/10.3389/fchem.2015.00062

Graça, J., & Pereira, H. (2000). Methanolysis of bark suberins: analysis of glycerol and acid monomers. *Phytochemical Analysis*, *11*(1), 45–51. https://doi.org/10.1002/(SICI)1099-1565(200001/02)11:1<45::AID-PCA481>3.0.CO;2-8

Graça, J., & Santos, S. (2007). Suberin: A biopolyester of plants' skin. *Macromolecular Bioscience*, *7*(2), 128–135. https://doi.org/10.1002/mabi.200600218

Guex, N., Peitsch, M. C., & Schwede, T. (2009). Automated comparative protein structure modeling with SWISS-MODEL and Swiss-PdbViewer: A historical perspective. *ELECTROPHORESIS*, *30*(S1), S162–S173. https://doi.org/10.1002/elps.200900140

Järvinen, R., Silvestre, A. J. D., Holopainen, U., Kaimainen, M., Nyyssölä, A., Gil, A. M., Neto, C. P., Lehtinen, P., Buchert, J., & Kallio, H. (2009). Suberin of potato (Solanum tuberosum Var. Nikola): Comparison of the effect of cutinase CcCutl with chemical depolymerization. *Journal of Agricultural and Food Chemistry*, *57*(19), 9016–9027. https://doi.org/10.1021/jf9008907

Jåstad, E. O., Bolkesjø, T. F., & Rørstad, P. K. (2020). Modelling effects of policies for increased production of forest-based liquid biofuel in the Nordic countries. *Forest Policy and Economics*, *113*, 102–191. https://doi.org/10.1016/j.forpol.2020.102091

Kakaei, K., Esrafili, M. D., & Ehsani, A. (2019). Introduction to Catalysis. *Interface Science and Technology*, *27*, 1–21. https://doi.org/10.1016/B978-0-12-814523-4.00001-0

Kawabata, T., Oda, M., & Kawai, F. (2017). Mutational analysis of cutinase-like enzyme, Cut190, based on the 3D docking structure with model compounds of polyethylene terephthalate. *Journal of Bioscience and Bioengineering*, *124*(1), 28–35. https://doi.org/10.1016/j.jbiosc.2017.02.007

Kawabata, T., Oda, M., Numoto, N., & Kawai, F. (2018). Structural and mutational analysis of polyethylene terephthalate-hydrolyzing enzyme, cut190, based on three-dimensional docking structure with model compounds of polyethylene terephthalate. *ACS Symposium Series*, *1310*, 63–75. https://doi.org/10.1021/bk-2018-1310.ch005

Kelley, L. A., Mezulis, S., Yates, C. M., Wass, M. N., & Sternberg, M. J. E. (2015). The Phyre2 web portal for protein modeling, prediction and analysis. *Nature Protocols*, *10*(6), 845–858. https://doi.org/10.1038/nprot.2015.053

Kitadokoro, K., Thumarat, U., Nakamura, R., Nishimura, K., Karatani, H., Suzuki, H., & Kawai, F. (2012). Crystal structure of cutinase Est119 from Thermobifida alba AHK119 that can degrade modified polyethylene terephthalate at 1.76 Å resolution. *Polymer Degradation and Stability*, *97*(5), 771–775. https://doi.org/10.1016/j.polymdegradstab.2012.02.003

Kolattukudy, P. E., Rogers, L. M., Li, D., Hwang, C. S., & Flaishman, M. A. (1995). Surface signaling in pathogenesis. *Proceedings of the National Academy of Sciences of the United States of America*, *92*(10), 4080–4087. https://doi.org/10.1073/pnas.92.10.4080

Komeil, D., Simao-Beaunoir, A. M., & Beaulieu, C. (2013). Detection of potential suberinase-encoding genes in streptomyces scabiei strains and other actinobacteria. *Canadian Journal of Microbiology*, *59*(5), 294–303. https://doi.org/10.1139/cjm-2012-0741

Kontkanen, H., Westerholm-Parvinen, A., Saloheimo, M., Bailey, M., Rättö, M., Mattila, I., Mohsina, M., Kalkkinen, N., Nakari-Setälä, T., & Buchert, J. (2009). Novel Coprinopsis cinerea polyesterase that hydrolyzes cutin and suberin. *Applied and Environmental Microbiology*, *75*(7), 2148–2157. https://doi.org/10.1128/AEM.02103-08

Kumaniaev, I., & Samec, J. S. M. (2018). Valorization of Quercus suber Bark toward Hydrocarbon Bio-Oil and 4-Ethylguaiacol. *ACS Sustainable Chemistry and Engineering*, *6*(5), 5737–5742. https://doi.org/10.1021/acssuschemeng.8b00537

Lab, Zhang, U. of M. (2020). *I-TASSER server for protein structure and function prediction*. https://zhanglab.ccmb.med.umich.edu/I-TASSER/

Leite, C., & Pereira, H. (2017). Cork-containing barks - a review. *Frontiers in Materials*, *3*. https://doi.org/10.3389/fmats.2016.00063

Li, Q., Li, G., Yu, S., Zhang, Z., Ma, F., & Feng, Y. (2011). Ring-opening polymerization of ε-caprolactone catalyzed by a novel thermophilic lipase from Fervidobacterium nodosum. *Process Biochemistry*, *46*(1), 253–257. https://doi.org/10.1016/j.procbio.2010.08.019

Longhi, S., Czjzek, M., Lamzin, V., Nicolas, A., & Cambillau, C. (1997). Atomic resolution (1.0 Å) crystal structure of Fusarium solani cutinase: Stereochemical analysis. *Journal of Molecular Biology*, *268*(4), 779–799. https://doi.org/10.1006/jmbi.1997.1000

Longhi, S., Nicolas, A., Creveld, L., Egmond, M., Verrips, C., de Vlieg, J., Martinez, C., & Cambillau, C. (1996). Dynamics of Fusarium Solani Cutinase Investigated Through Structural Comparison Among Different Crystal Forms of Its Variants. *Proteins*, *26*(4). https://doi.org/10.1002/(SICI)1097-0134(199612)26:4<442::AID-PROT5>3.0.CO;2-D

Ma, Y., Yao, M., Li, B., Ding, M., He, B., Chen, S., Zhou, X., & Yuan, Y. (2018). Enhanced Poly(ethylene terephthalate) Hydrolase Activity by Protein Engineering. *Engineering*, *4*(6), 888–893. https://doi.org/10.1016/j.eng.2018.09.007

Marques, A. V., & Pereira, H. (2014). Aliphatic bio-oils from corks: A Py-GC/MS study. *Journal of Analytical and Applied Pyrolysis*, *109*, 29–40. https://doi.org/10.1016/j.jaap.2014.07.016

Martinez, C., De Geus, P., Lauwereys, M., Matthyssens, G., & Cambillau, C. (1992). Fusarium solani cutinase is a lipolytic enzyme with a catalytic serine accessible to solvent. *Nature*, *356*(6370), 615–618. https://doi.org/10.1038/356615a0

Medicine, U. S. N. L. of. (2020). *National Center for Biotechnology Information*. https://www.ncbi.nlm.nih.gov/

Meng, X.-Y., Zhang, H.-X., Mezei, M., & Cui, M. (2011). Molecular docking: a powerful approach for structure-based drug discovery. *Current Computer-Aided Drug Design*, *7*(2), 146–157. https://doi.org/10.2174/157340911795677602

Nigam, P. S., & Singh, A. (2011). Production of liquid biofuels from renewable resources. *Progress in Energy and Combustion Science*, *37*(1), 52–68. https://doi.org/10.1016/j.pecs.2010.01.003

Nyon, M. P., Rice, D. W., Berrisford, J. M., Hounslow, A. M., Moir, A. J. G., Huang, H., Nathan, S., Mahadi, N. M., Bakar, F. D. A., & Craven, C. J. (2009). Catalysis by Glomerella cingulata Cutinase Requires Conformational Cycling between the Active and Inactive States of Its Catalytic Triad.

Journal of Molecular Biology, *385*(1), 226–235. https://doi.org/10.1016/j.jmb.2008.10.050

Nyyssölä, A. (2015). Which properties of cutinases are important for applications? *Applied Microbiology and Biotechnology*, *99*(12), 4931–4942. https://doi.org/10.1007/s00253-015-6596-z

Pereira, H. (2013). Variability of the chemical composition of cork. *BioResources*, *8*(2), 2246–2256. https://doi.org/10.15376/biores.8.2.2246-2256

Ping, L. F., Chen, X. Y., Yuan, X. L., Zhang, M., Chai, Y. J., & Shan, S. D. (2017). Application and comparison in biosynthesis and biodegradation by Fusarium solani and Aspergillus fumigatus cutinases. *International Journal of Biological Macromolecules*, *104*, 1238–1245. https://doi.org/10.1016/j.ijbiomac.2017.06.118

Pollard, M., Beisson, F., Li, Y., & Ohlrogge, J. B. (2008). Building lipid barriers: biosynthesis of cutin and suberin. *Trends in Plant Science*, *13*(5), 236–246. https://doi.org/10.1016/j.tplants.2008.03.003

Raud, M., Kikas, T., Sippula, O., & Shurpali, N. J. (2019). Potentials and challenges in lignocellulosic biofuel production technology. *Renewable and Sustainable Energy Reviews*, *111*, 44–56. https://doi.org/10.1016/j.rser.2019.05.020

Rauwerdink, A., & Kazlauskas, R. J. (2015). How the Same Core Catalytic Machinery Catalyzes 17 Different Reactions: The Serine-Histidine-Aspartate Catalytic Triad of α/β-Hydrolase Fold Enzymes. *ACS Catalysis, 5*(10), 6153–6176. https://doi.org/10.1021/acscatal.5b01539

Roussel, A., Amara, S., Nyyssölä, A., Mateos-Diaz, E., Blangy, S., Kontkanen, H., Westerholm-Parvinen, A., Carrière, F., & Cambillau, C. (2014). A cutinase from Trichoderma reesei with a lid-covered active site and kinetic properties of true lipases. *Journal of Molecular Biology*, *426*(22), 3757–3772. https://doi.org/10.1016/j.jmb.2014.09.003

Roy, A., Kucukural, A., & Zhang, Y. (2010). I-TASSER: A unified platform for automated protein structure and function prediction. *Nature Protocols*, *5*(4), 725–738. https://doi.org/10.1038/nprot.2010.5

Rübberdt, K., Michels, J., & König, L. (2019). *Roadmap for the Chemical Industry in Europe towards a Bioeconomy*.

Schimel, D., Stephens, B. B., & Fisher, J. B. (2015). Effect of increasing CO2 on the terrestrial carbon cycle. *Proceedings of the National Academy of Sciences of the United States of America*, *112*(2), 436–441. https://doi.org/10.1073/pnas.1407302112

Schrödinger. (2016). *GlideScore/Docking Score doesn't correlate with my known activities. What is wrong?* https://www.schrodinger.com/kb/144

Şen, A., Miranda, I., Santos, S., Graça, J., & Pereira, H. (2010). The chemical composition of cork and phloem in the rhytidome of Quercus cerris bark. *Industrial Crops and Products*, *31*(2), 417–422. https://doi.org/10.1016/j.indcrop.2010.01.002

Shinozaki, Y., Kikkawa, Y., Sato, S., Fukuoka, T., Watanabe, T., Yoshida, S., Nakajima-Kambe, T., & Kitamoto, H. K. (2013). Enzymatic degradation of polyester films by a cutinase-like enzyme from Pseudozyma antarctica: Surface plasmon resonance and atomic force microscopy study. *Applied Microbiology and Biotechnology*, *97*(19), 8591–8598. https://doi.org/10.1007/s00253-012-4673-0

Shogren, R., Wood, D., Orts, W., & Glenn, G. (2019). Plant-based materials and transitioning to a circular economy. *Sustainable Production and Consumption*, *19*, 194–215. https://doi.org/10.1016/j.spc.2019.04.007

Skamnioti, P., Furlong, R. F., & Gurr, S. J. (2008a). The fate of gene duplicates in the genomes of fungal pathogens. *Communicative & Integrative Biology*, *1*(2), 196–198. https://doi.org/10.4161/cib.1.2.7144

Skamnioti, P., Furlong, R. F., & Gurr, S. J. (2008b). Evolutionary history of the ancient cutinase family in five filamentous Ascomycetes reveals differential gene duplications and losses and in *Magnaporthe grisea* shows evidence of sub- and neo-functionalization. *New Phytologist*, *180*(3), 711–721. https://doi.org/10.1111/j.1469-8137.2008.02598.x

Soni, S., Sathe, S. S., Sheth, R. R., Tiwari, P., Vadgama, R. K. N., Odaneth, A. A., Lali, A. M., & Chandrayan, S. K. (2019). N-terminal domain replacement changes an archaeal monoacylglycerol lipase into a triacylglycerol lipase. *Biotechnology for Biofuels*, *12*(1), 110. https://doi.org/10.1186/s13068-019-1452-5

Structural Bioinformatics Group, I. C. (2020). *PHYRE2 Protein Fold Recognition Server*. http://www.sbg.bio.ic.ac.uk/~phyre2/html/page.cgi?id=index

Worldwide PDB, E. D. R. (2020). *RCSB PDB*. https://www.rcsb.org/

Zhang, J. Y. and Y. (2015). I-TASSER server: new development for protein structure and function predictions. *Nucleic Acids Research*, *43*(Web server), W174–W181. https://doi.org/10.1093/nar/gkv342

8. Supplementary Information

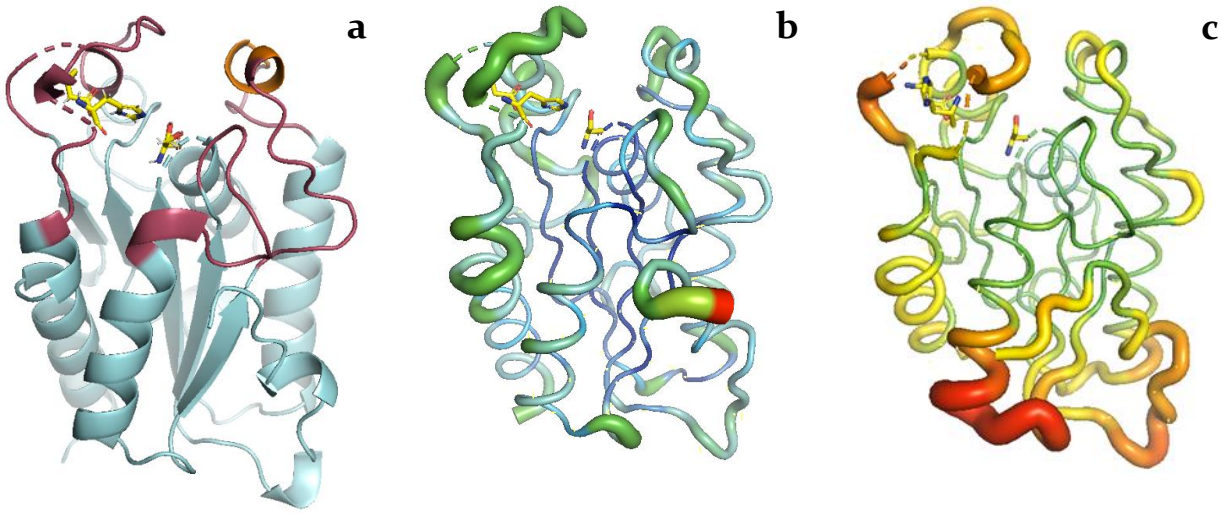

Figure S 1. *Mobility of hydrophobic loops of cutinases.* ***a.*** F. solani *cutinase (PDB ID: 1cex). High mobility flaps coloured in ruby and blocking loop coloured in orange. Information collected after analysis of electron relaxation and NMR studies.* ***b.*** F. solani *structure (PDB ID: 1cex) coloured by b-factor. Loops show uncertainty in their position as they are coloured in warmer colours.* ***c.*** G. cingulata *structure (PDB ID: 3dcn) coloured by b-factor. Loops show uncertainty in their position as they are coloured in warmer colours.*

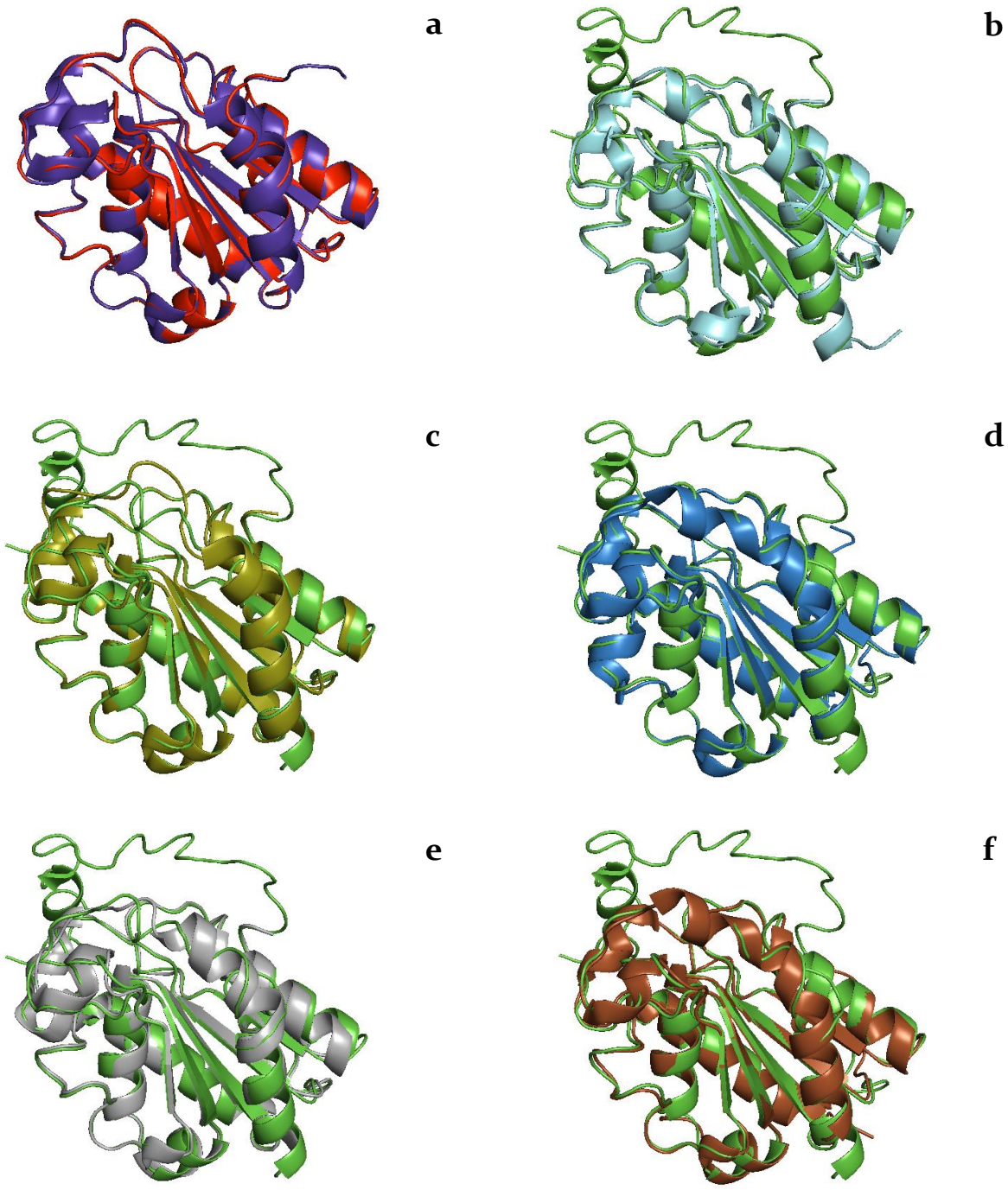
a
b
c
d
e
f

g

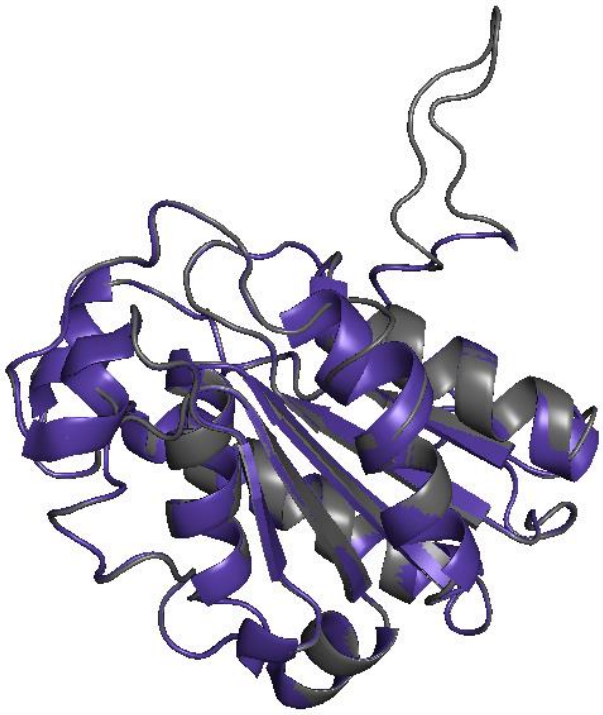

h

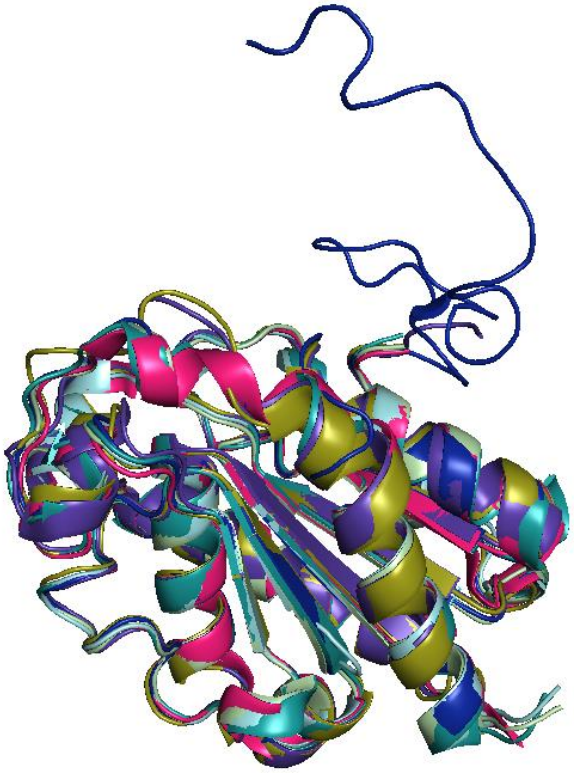

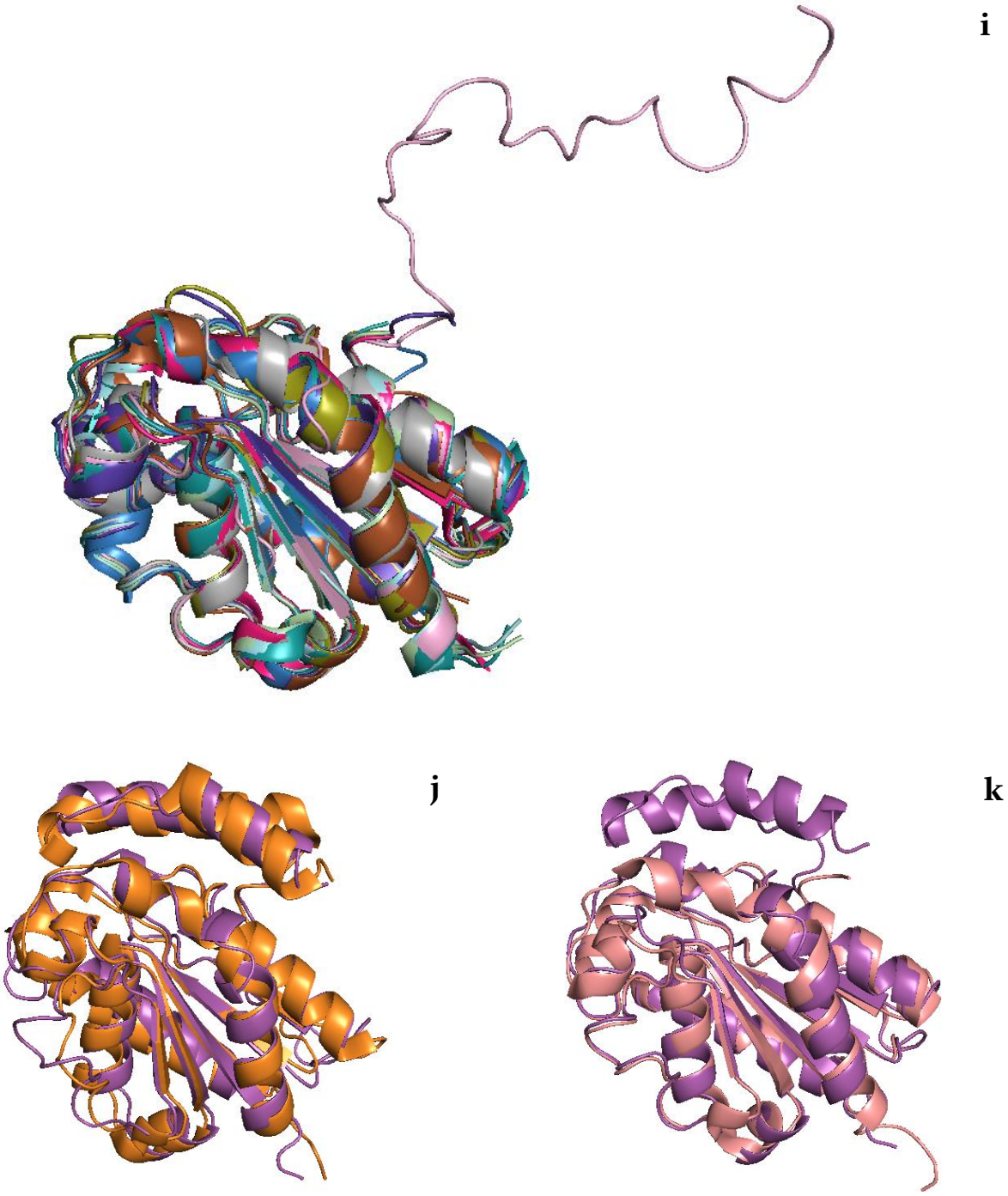
i
j
k

l

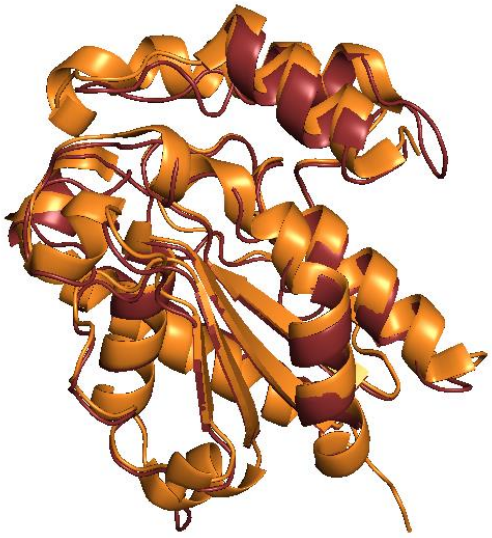

Figure S 2. *Homology models of* T. terrestris *cutinase aligned with their respective templates.* ***a****. Swiss model (red) aligned with 3dcn (purple blue) template.* ***b.*** *Phyre model (green) aligned with 1cex (cyan) template.* ***c.*** *Phyre model (green) aligned with 3dd5 (deep olive) template.* ***d.*** *Phyre model (green) aligned with 3gbs (sky blue) template.* ***e.*** *Phyre model (green) aligned with 4oyl (gray) template.* ***f.*** *Phyre model (green) aligned with 5x88 (brown) template.* ***g.*** *Prime 1 model (dark gray) aligned with 3dcn (purple blue) template.* ***h.*** *Prime 2 model (blue) aligned with 3dcn (purple blue), 3dd5 (deep olive), 1cuw (deep teal), 1cud (pale green), 3esa (hot pink), 1cex (cyan) templates****. i.*** *Prime 3 model (pink) aligned with 3dcn (purple blue), 3dd5 (deep olive), 1cuw (deep teal), 1cud (pale green), 3esa (hot pink), 1cex (cyan), 3gbs (sky blue), 4oyl (gray), 5x88 (brown) templates.* ***j.*** *iTasser model (magenta) aligned with 4psc (orange) template.* ***k.*** *iTasser model (magenta) aligned with 3esb (salmon) template.* ***l.*** *Prime 4 model (ruby) aligned with 4psc (orange) template.*

***Table S 1**. Templates used to build each model and corresponding evaluating parameters. Marked gray are relevant template structures though not used for the model; abb. Seq. Id – sequence identity; Xray – resolution; Conf – confidence of Phyre model; GMQE – global Swiss model quality estimate; QMEAN – Swiss model deviation from PDB crystallized structures; TM-Score – iTasser model score relative to template structure; RMSD – root mean square deviation of atomic positions of iTasser model.*

Template	Source	SwissModel	Phyre2	Prime 1	Prime 2	Prime 3	Prime 4	iTasser
3dcn	*Glomerella cingulata*	GMQE: 0.73 QMEAN: -0.99 Seq. Id: 58.33% Coverage: 84% Xray: 1.90Å		Score: 550 Seq. Id: 57% Gaps: 1% Xray: 1.9Å	Score: 550 Seq. Id: 57% Gaps: 1% Xray: 1.9Å	Score: 550 Seq. Id: 57% Gaps: 1% Xray: 1.9Å		TM-Score: 0.818 RMSD: 1.16 Seq. Id: 56% Coverage: 84.2%
3dd5	*Glomerella cingulata*		Conf: 100% Seq. Id: 57% Coverage: 84%		Score: 550 Seq. Id: 57% Gaps: 1% Xray: 2.6 Å	Score: 550 Seq. Id: 57% Gaps: 1% Xray: 2.6 Å		
1cuw	*Fusarium solani*				Score: 529 Seq. Id: 51% Gaps: 2% Xray: 2.7 Å	Score: 529 Seq. Id: 51% Gaps: 2% Xray: 2.7 Å		
1cud	*Fusarium solani*				Score: 528 Seq. Id: 51% Gaps: 2% Xray: 2.7 Å	Score: 528 Seq. Id: 51% Gaps: 2% Xray: 2.7 Å		
3esa	*Fusarium solani*				Score: 528 Seq. Id: 51% Gaps: 2% Xray: 2.0Å	Score: 528 Seq. Id: 51% Gaps: 2% Xray: 2.0Å		
1cex	*Fusarium solani*		Conf: 100% Seq. Id: 51% Coverage: 85%		Score: 527 Seq. Id: 51% Gaps: 2% Xray: 1.0 Å	Score: 527 Seq. Id: 51% Gaps: 2% Xray: 1.0 Å		
3esb	*Fusarium solani*							TM-Score: 0.825 RMSD: 1.14 Seq. Id: 51.5% Coverage: 85.1%
5x88	*Malbranchea cinnamomea*		Conf: 100% Seq. Id: 52% Coverage: 79%			Score: 501 Seq. Id: 51% Gaps: 2% Xray: 1.76 Å		TM-Score: 0.790 RMSD: 1.11 Seq. Id: 51.3% Coverage: 81.6%
4oyl	*Humicola insolens*		Conf: 100% Seq. Id: 51% Coverage: 84%			Score: 494 Seq. Id: 51% Gaps: 1% Xray: 2.05Å		TM-Score: 0.815 RMSD: 0.79 Seq. Id: 50.8% Coverage: 82.9%
3gbs	*Aspergillus oryzae*		Conf: 100% Seq. Id: 51% Coverage: 81%			Score: 457 Seq. Id: 53% Gaps: 3% Xray: 1.75 Å		TM-Score: 0.794 RMSD: 1.39 Seq. Id: 50.8% Coverage: 82.0%
4psc	*Trichoderma reesei*			Score: 196 Seq. Id: 31% Gaps: 8% Xray: 1.15Å	Score: 196 Seq. Id: 31% Gaps: 8% Xray: 1.15Å	Score: 196 Seq. Id: 31% Gaps: 8% Xray: 1.15Å	Score: 196 Seq. Id: 31% Gaps: 8% Xray: 1.15Å	TM-Score: 0.860 RMSD: 1.65 Seq. Id: 29% Coverage: 92.1%
4psd	*Trichoderma reesei*		Conf: 100% Seq. Id: 26% Coverage: 96%	Score: 196 Seq. Id: 31% Gaps: 8% Xray: 1.52Å	Score: 196 Seq. Id: 31% Gaps: 8% Xray: 1.52Å	Score: 196 Seq. Id: 31% Gaps: 8% Xray: 1.52Å	Score: 196 Seq. Id: 31% Gaps: 8% Xray: 1.52Å	

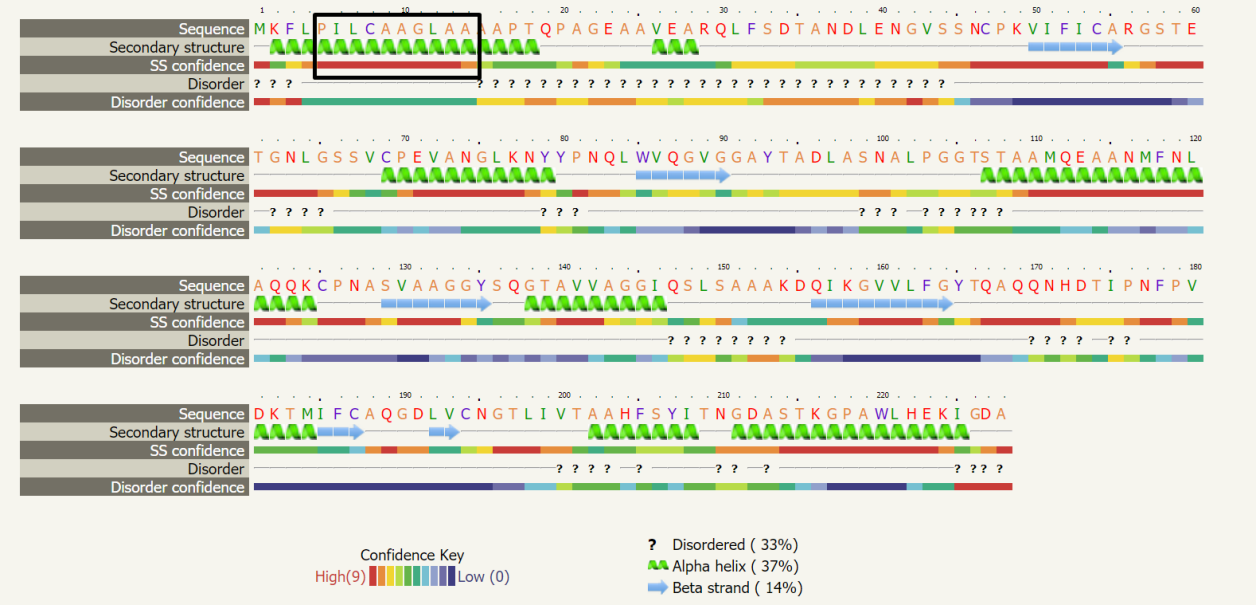

Figure S 3. *Secondary structure prediction of Phyre model. Initial 32 aa predicted by* ab initio *techniques (highly unreliable), but a high confidence helix is predicted from aa5 to aa14.*

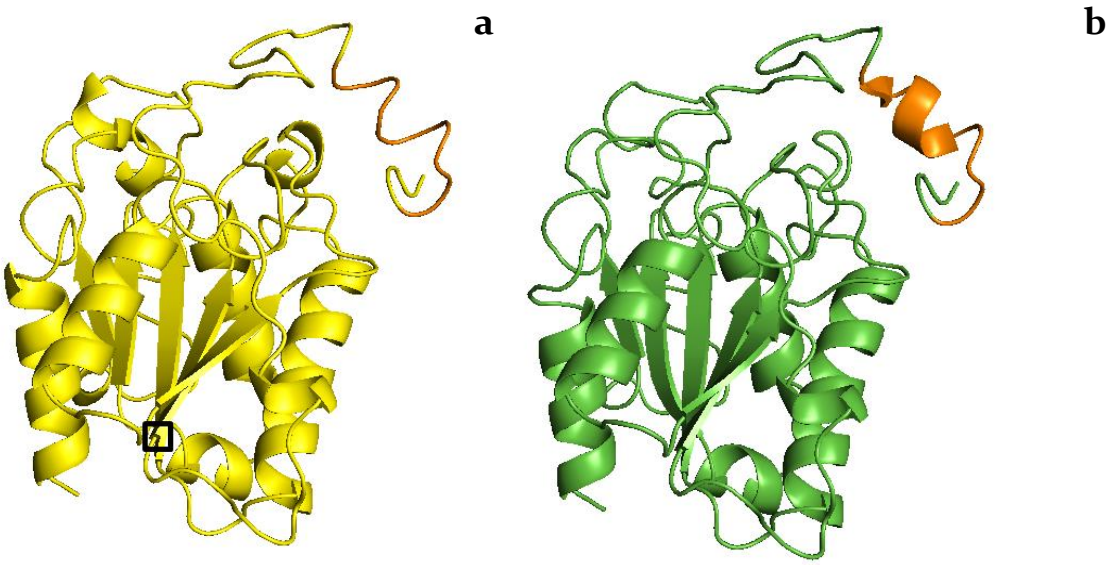

Figure S 4. *Helix figure is modelled for aa5-aa14 after model refinement.* ***a.*** *Yellow cartoon figure shows Phyre model pre-refined. Aa5-aa14 are coloured orange.* ***b.*** *Green cartoon figure shows Phyre model pos-refined. Aa5-aa14 are coloured orange.*

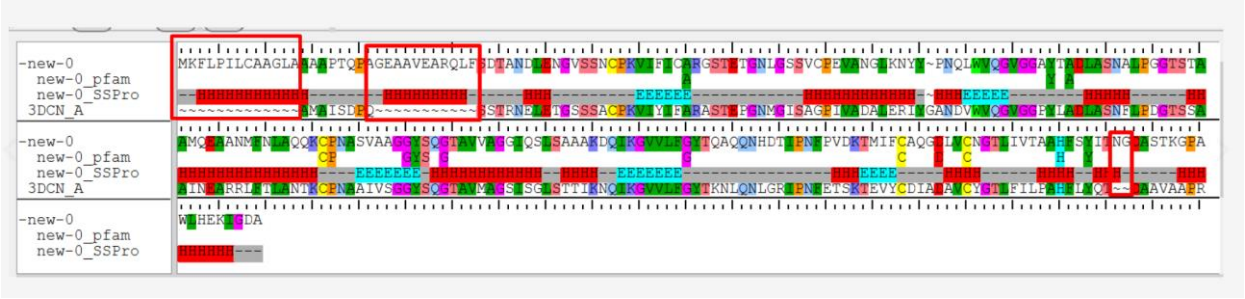

Figure S 5. *Target sequence aligned with 3dcn template. Red squares disclose gaps in the alignment.*

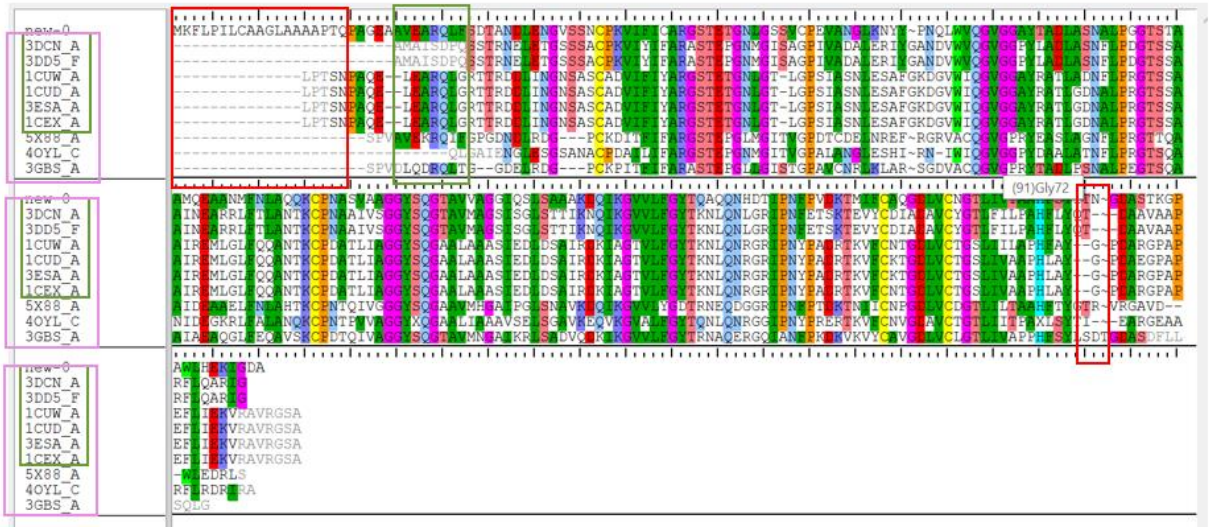

Figure S 6. *Multi-sequence alignment. Two consensus models were built to try to fill in the gaps of the previous alignment. N-terminus was not filled. Green box comprises of templates used for consensus model Prime 2 and pink box comprises of templates used for consensus model Prime 3.*

a

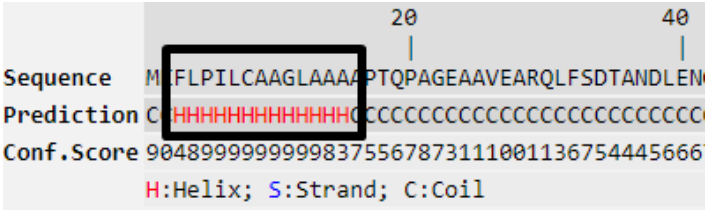

b

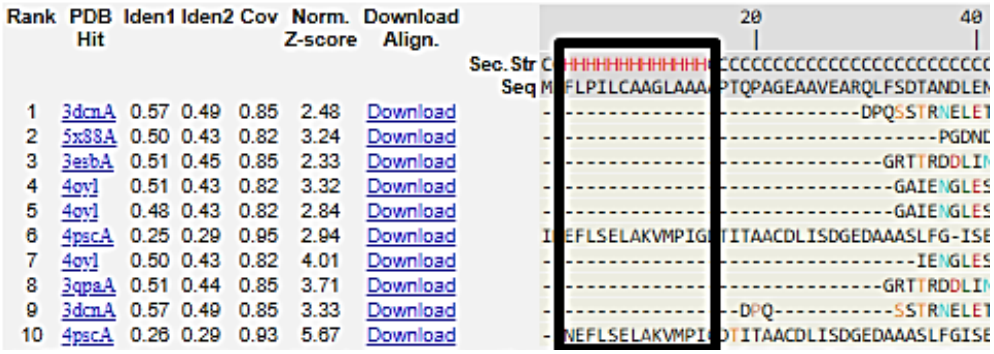

Rank	PDB Hit	Iden1	Iden2	Cov	Norm. Z-score	Download Align.
1	3dcnA	0.57	0.49	0.85	2.48	Download
2	5x88A	0.50	0.43	0.82	3.24	Download
3	3esbA	0.51	0.45	0.85	2.33	Download
4	4oyl	0.51	0.43	0.82	3.32	Download
5	4oyl	0.48	0.43	0.82	2.84	Download
6	4pscA	0.25	0.29	0.95	2.94	Download
7	4oyl	0.50	0.43	0.82	4.01	Download
8	3qpaA	0.51	0.44	0.85	3.71	Download
9	3dcnA	0.57	0.49	0.85	3.33	Download
10	4pscA	0.26	0.29	0.93	5.67	Download

c

Top 10 Identified stuctural analogs in PDB

Click to view	Rank	PDB Hit	TM-score	RMSD[a]	IDEN[a]	Cov	Alignment
◉	1	4pscA	0.860	1.65	0.290	0.921	Download
○	2	3esbA	0.825	1.14	0.515	0.851	Download
○	3	3dcnA	0.818	1.16	0.560	0.842	Download
○	4	4oylA	0.815	0.79	0.508	0.829	Download
○	5	3gbsA	0.794	1.39	0.508	0.820	Download
○	6	5x88A	0.790	1.11	0.513	0.816	Download
○	7	3eblA	0.685	3.83	0.110	0.882	Download
○	8	1lzlA	0.682	3.58	0.105	0.851	Download
○	9	2czqA	0.679	2.42	0.271	0.754	Download
○	10	3qh4A	0.678	3.95	0.137	0.873	Download

Figure S 7. *iTasser results.* ***a.*** *iTasser predicts helix in N-terminus of model.* ***b.*** *iTasser found one crystal structure displaying a possible helix-like homologous N-terminus: 4psc.* ***c.*** *Top 10 identified structural analogs in PDB of iTasser model.*

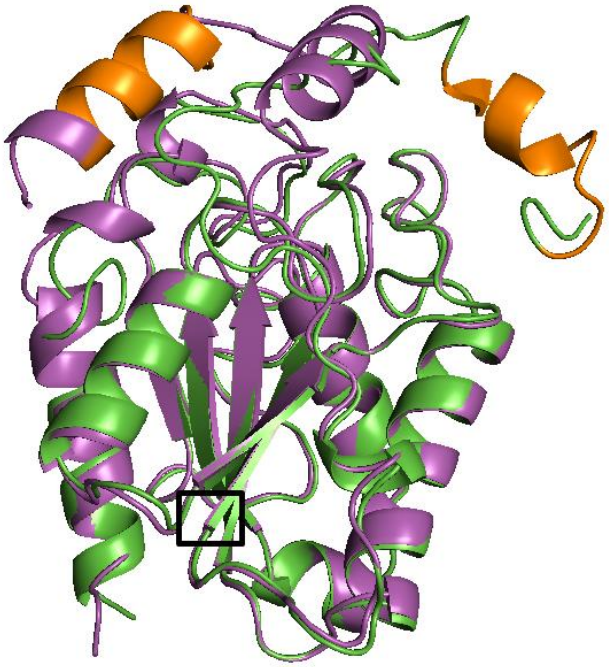

Figure S 8. *Helix conformation (5aa-14aa in orange) and disposition on Phyre (green) and iTasser (magenta) models. They are both hovering the binding cleft. Loop comes out of signaled beta sheet in both models.*

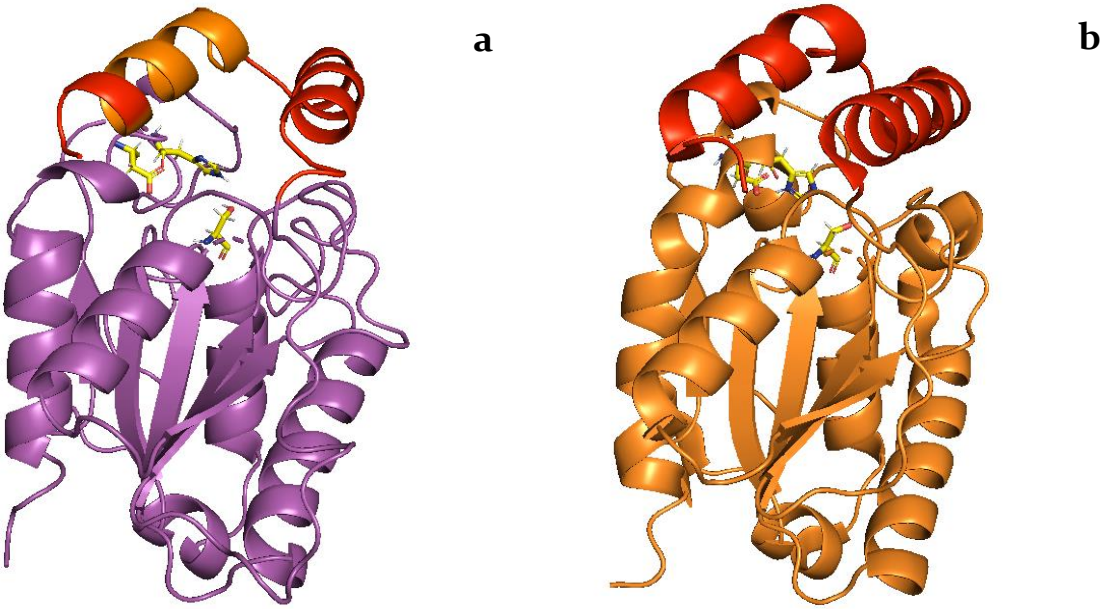

Figure S 9. T. terrestris *cutinase displays a lid covering the active site.* ***a.*** *Lid covering the active site (red) in iTasser model. Orange represents the residues of high confidence helix structure in Phyre model (5aa-14aa), which belong to lid structure in iTasser model.* **b.** *Lid covering the active site (red) in 4psc template.*

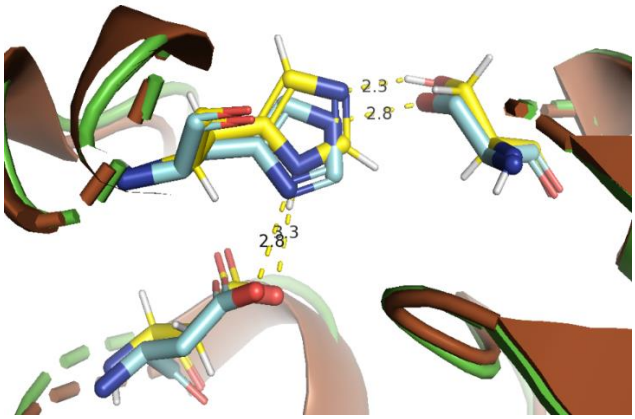

Figure S 10. *Phyre model aligned with 5x88 template (*M. cinnamomea*). Active site residues coloured by element with custom carbons coloured yellow (Phyre) and cyan (5x88). Measurements displayed are in Å.*

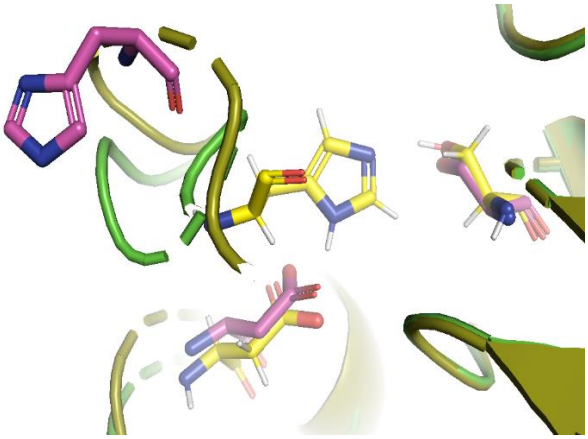

Figure S 11. *Phyre model aligned with 3dd5 template (*G. cingulata*). Active site residues coloured by element with custom carbons coloured yellow (Phyre) and magenta (3dd5). Inactive state of template histidine shows.*

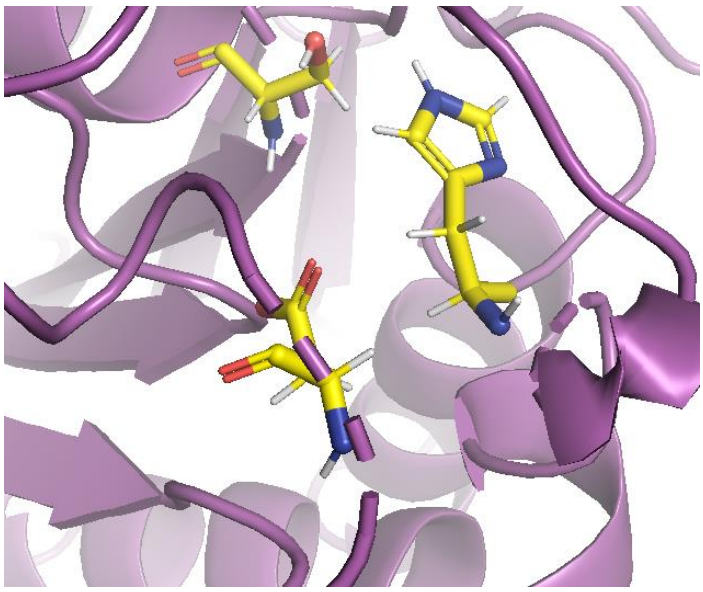

Figure S 12. *Catalytic histidine in iTasser model. Active site residues coloured by element with custom carbons coloured yellow. Model histidine is placed on helix. Not much flexibility exists for this residue to shift towards catalytic aspartate.*

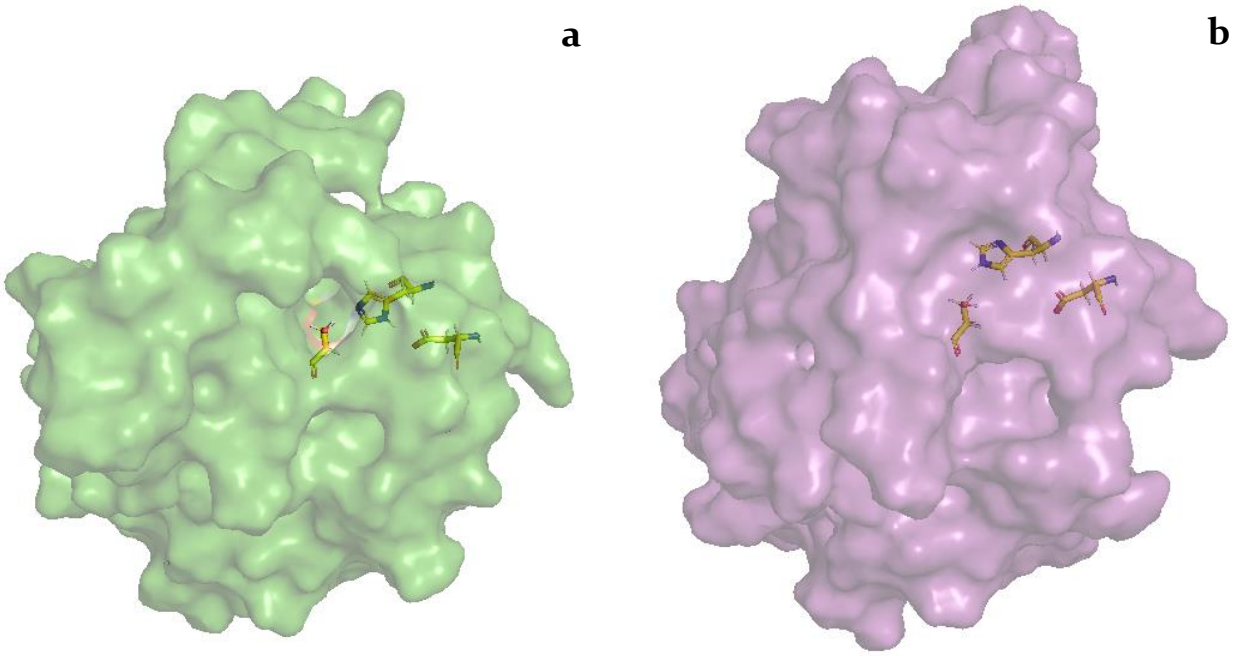

Figure S 13. *Phyre model presents a larger catalytic groove than iTasser model.* ***a.*** *Phyre model represented as surface. Catalytic groove exists. Catalytic serine is exposed to solvent* ***b.*** *iTasser model represented as surface. Catalytic groove not as dominant.*

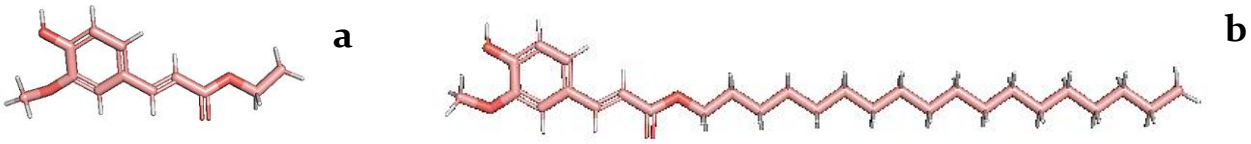

Figure S 14. *Example of two of the designed ligands.* ***a.*** *FA-C2* ***b.*** *FA-C18.*

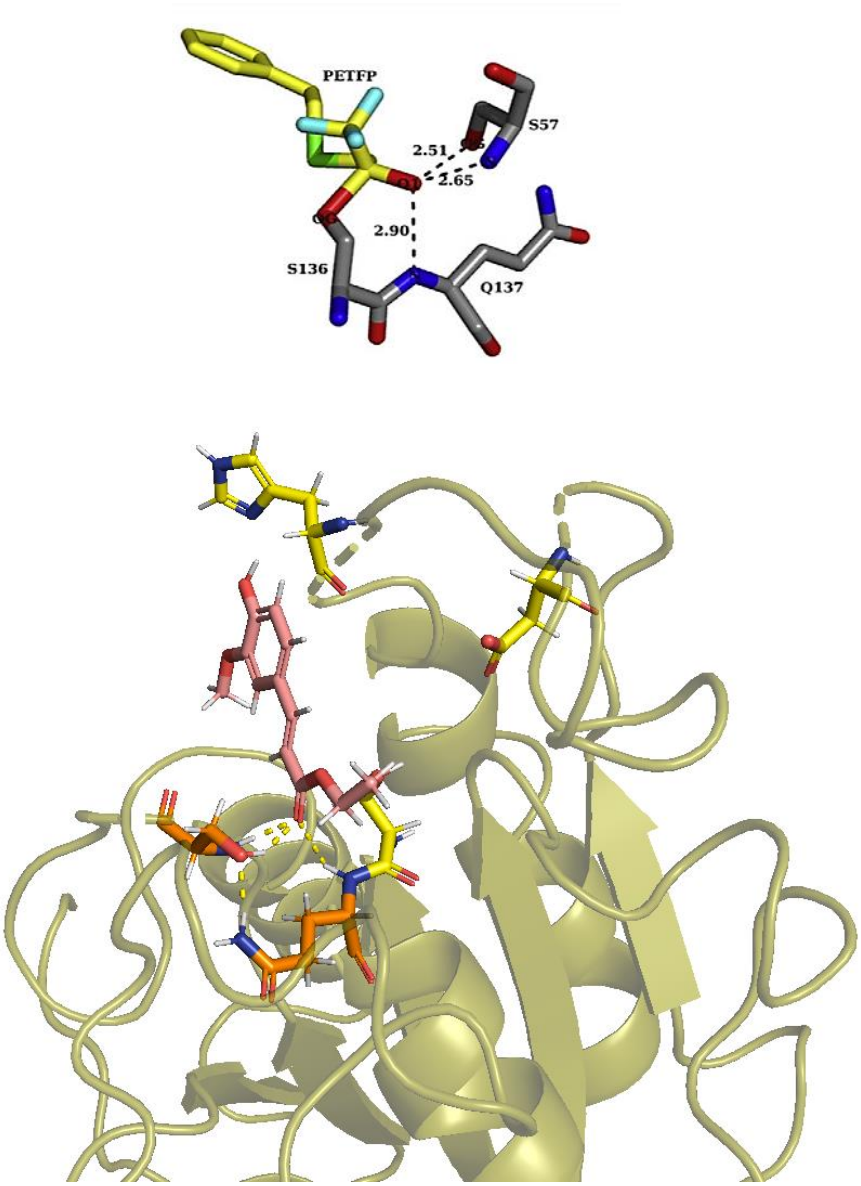

Figure S 15. *Oxyanion hole of* G. cingulata *cutinase.* ***a.*** *Oxyanion hole stabilization of* G. cingulata *cutinase (PDB ID: 3dea) native ligand PETFP. The double bond oxygen attached to the scissile carbon is stabilized by hydrogens from oxygen of Ser57 and from amides of Ser57 and Gln137.* ***b.*** G. cingulata *cutinase (PDB ID: 3dea) as positive control for docking of cutinases. Enzyme in deep olive cartoon figure. Active site residues show in sticks coloured by element with custom carbons coloured yellow. The double bond oxygen attached to the scissile carbon of docked FA-C2 is stabilized by hydrogens from oxygen of Ser57 and from amides of Ser57 and Gln137, both residues coloured by element with orange custom carbons. Hydrogen bonds are represented by yellow dashes.*

Table S 2. *Receptor grid settings and Glide constraints.*

	Receptor grid settings						Glide constraints		
	Centre	Size (Å)	Spatial restricted atom	Spatial restriction radius (Å)	Hydrogen bonds	Rotational atoms	Spatial constraints	Hydrogen bonds ticked	Hydrogen bonds setting
FA-C2	catSer	10x10x10	X	X	Oxy aa	catSer	X	All	At least 1
FA-C4	catSer	10x10x10	X	X	Oxy aa	catSer	X	All	At least 1
FA-C6	catSer	10x10x10	X	X	Oxy aa	catSer	X	All	At least 1
FA-C8	catSer	10x10x10	X	X	Oxy aa	catSer	X	All	At least 1
FA-l0	catSer	36x36x36	O-(C)=O	2.0	Oxy aa	catSer	O-(C)=O	oxySer (N) oxySer (O)	At least 1
FA-C12	catSer	36x36x36	O-(C)=O	2.0	Oxy aa	catSer	O-(C)=O	oxySer (N) oxyGln (N)	At least 1
FA-C14	catSer	36x36x36	O-(C)=O	2.0	Oxy aa	catSer	O-(C)=O	oxySer (N) oxyGln (N)	At least 1
FA-C16	catSer	36x36x36	O-(C)=O	2.0	Oxy aa	catSer	O-(C)=O	oxySer (N) oxyGln (N)	At least 1
FA-C18	catSer	36x36x36	O-(C)=O	2.0	Oxy aa	catSer	O-(C)=O	oxySer (N) oxyGln (N)	At least 1

Nomenclature: 'catSer' stands for catalytic serine; 'Oxy aa' stands for all oxyanion hole residues; as an example, 'oxySer(N)' stands for the amide of the oxyanion serine which has been ticked to donate hydrogens to stabilize the oxyanion hole; 'at least 1' means that during docking at least one of the hydrogen bonds constrained had to exist.

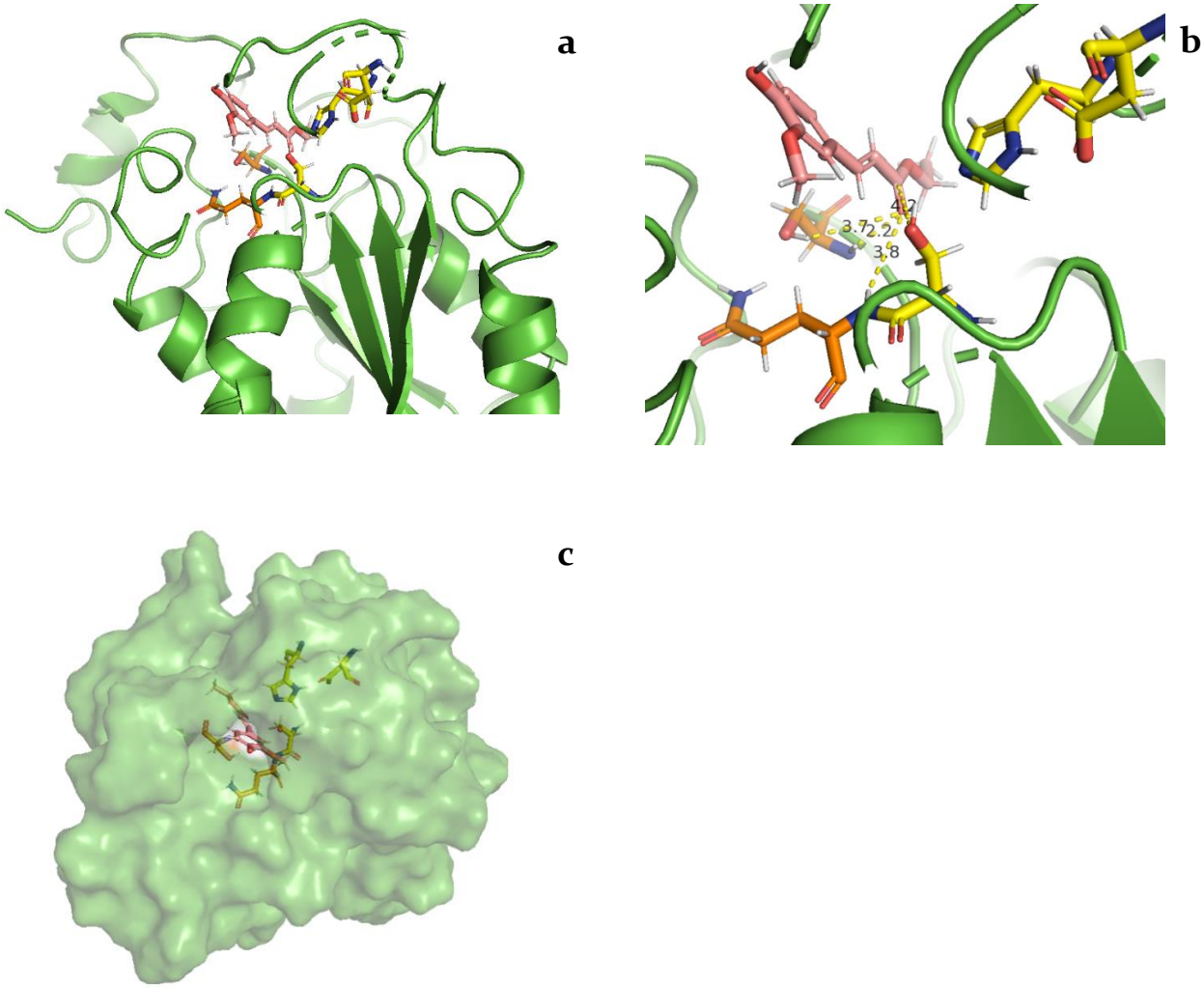

Figure S 16. *Docking of FA-C2 in* T. terrestris *cutinase. Active site and oxyanion hole residues show in sticks coloured by element with custom carbons coloured yellow and orange, respectively. FA-C2 represented in sticks coloured by element with salmon custom carbons.* ***a.*** T. terrestris *cutinase represented in green cartoon figure with docked FA-C2.* ***b.*** T. terrestris *cutinase represented in green cartoon figure with docked FA-C2. Measurements displayed are in Å and are represented by yellow dashed lines* ***c.*** T. terrestris *cutinase represented in green surface figure. The aliphatic domain of FA-C2 goes through the binding tunnel.*

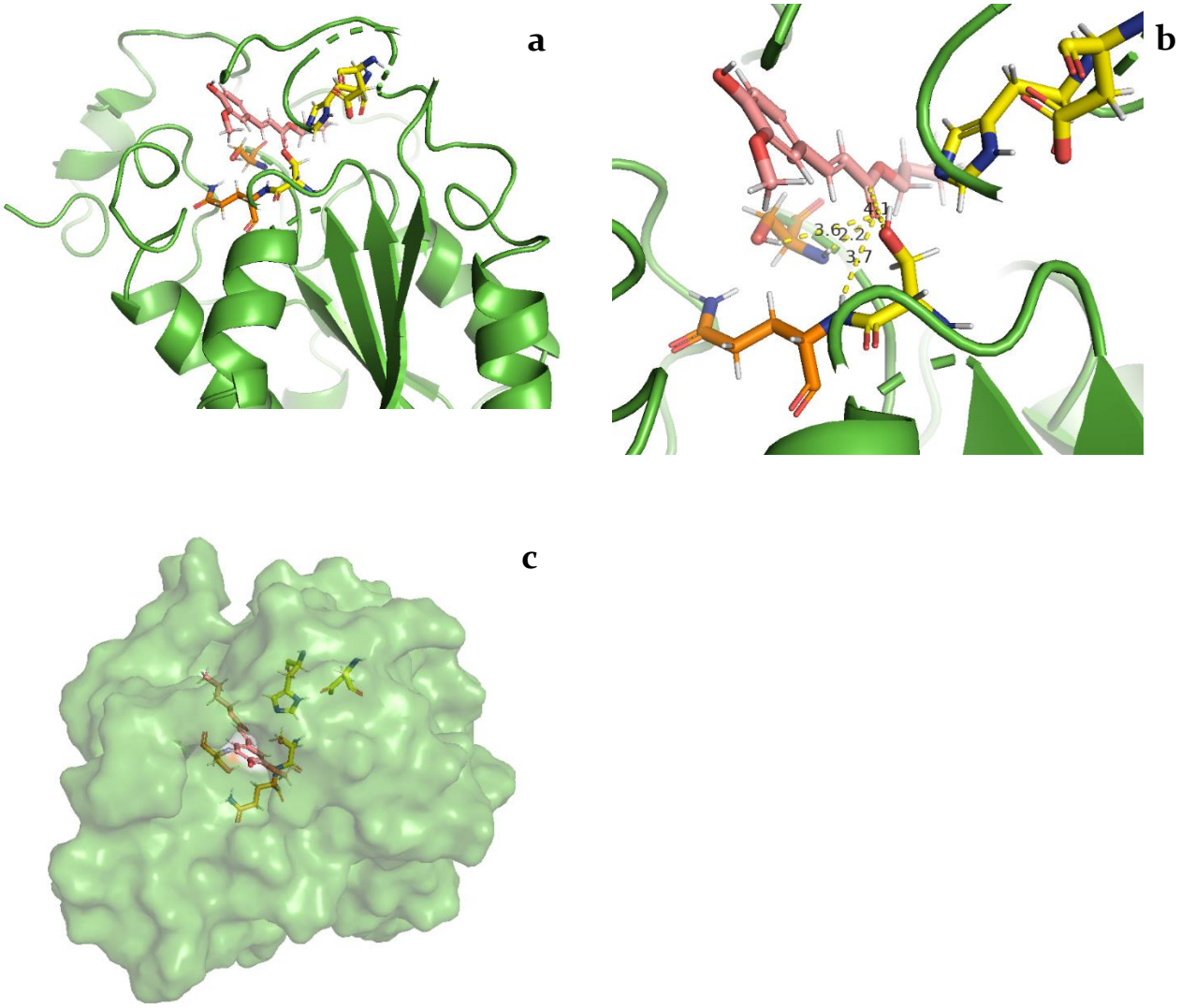

Figure S 17. *Docking of FA-C4 in* T. terrestris *cutinase. Active site and oxyanion hole residues show in sticks coloured by element with custom carbons coloured yellow and orange, respectively. FA-C4 represented in sticks coloured by element with salmon custom carbons.* ***a.*** T. terrestris *cutinase represented in green cartoon figure with docked FA-C4.* ***b.*** T. terrestris *cutinase represented in green cartoon figure with docked FA-C4. Measurements displayed are in Å and are represented by yellow dashed lines* ***c.*** T. terrestris *cutinase represented in green surface figure. The aliphatic domain of FA-C4 goes through the binding tunnel.*

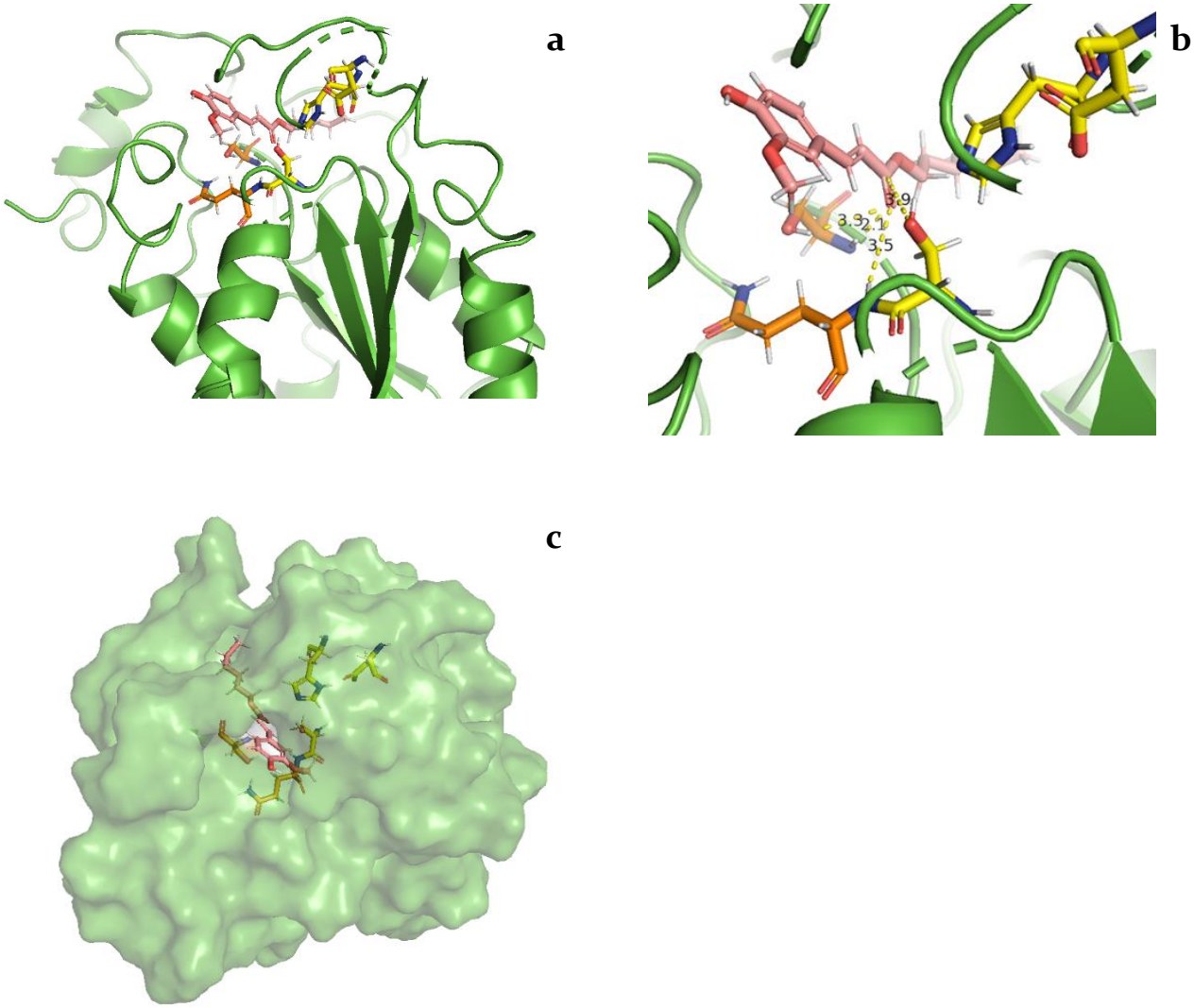

Figure S 18. *Docking of FA-C6 in* T. terrestris *cutinase. Active site and oxyanion hole residues show in sticks coloured by element with custom carbons coloured yellow and orange, respectively. FA-C6 represented in sticks coloured by element with salmon custom carbons.* ***a.*** T. terrestris *cutinase represented in green cartoon figure with docked FA-C6.* ***b.*** T. terrestris *cutinase represented in green cartoon figure with docked FA-C6. Measurements displayed are in Å and are represented by yellow dashed lines* ***c.*** T. terrestris *cutinase represented in green surface figure. The aliphatic domain of FA-C6 goes through the binding tunnel.*

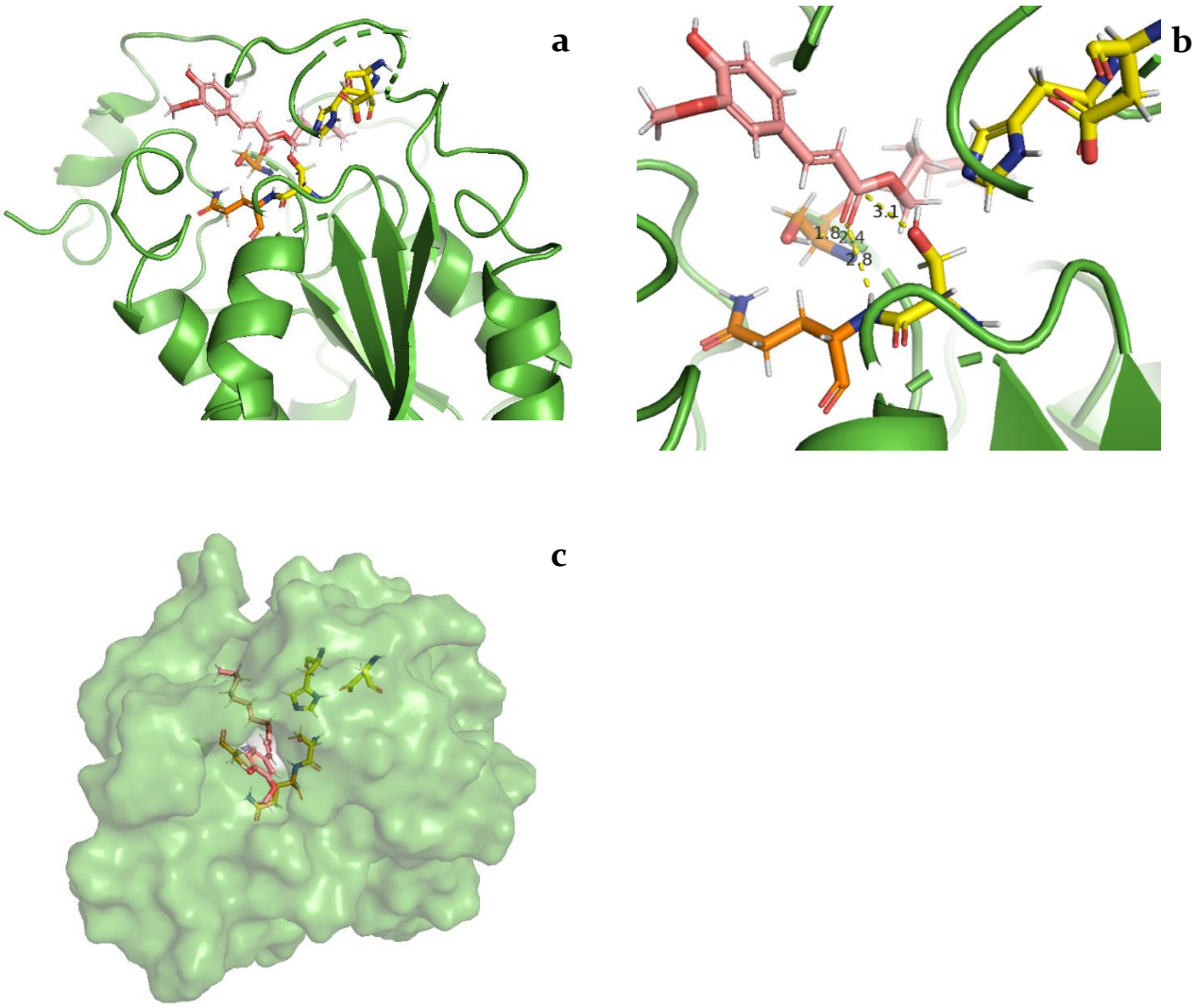

Figure S 19. *Docking of FA-C8 in* T. terrestris *cutinase. Active site and oxyanion hole residues show in sticks coloured by element with custom carbons coloured yellow and orange, respectively. FA-C8 represented in sticks coloured by element with salmon custom carbons.* ***a.*** T. terrestris *cutinase represented in green cartoon figure with docked FA-C8.* ***b.*** T. terrestris *cutinase represented in green cartoon figure with docked FA-C8. Measurements displayed are in Å and are represented by yellow dashed lines* **c.** T. terrestris *cutinase represented in green surface figure. The aliphatic domain of FA-C8 goes through the binding tunnel.*

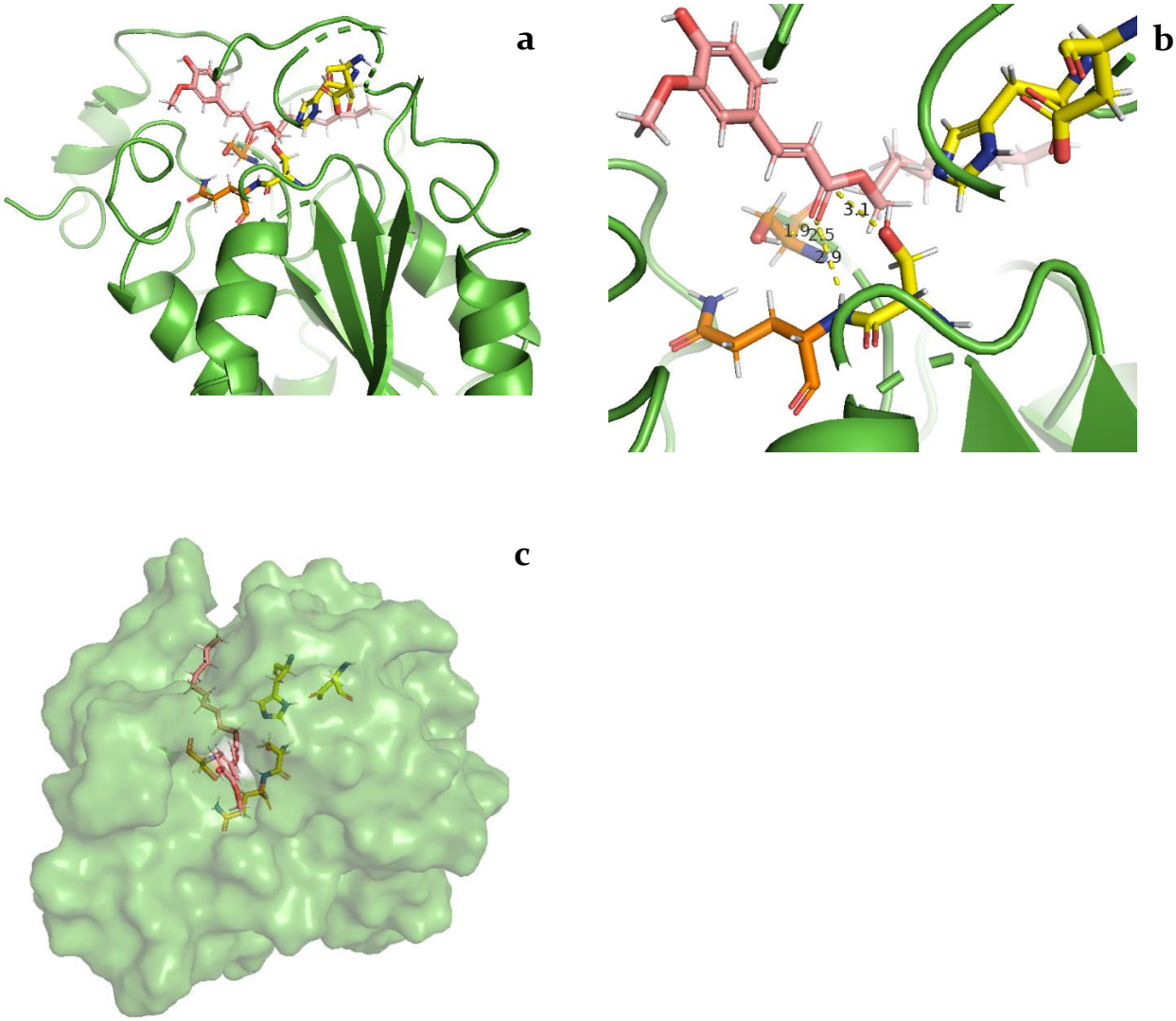

Figure S 20. *Docking of FA-C10 in* T. terrestris *cutinase. Active site and oxyanion hole residues show in sticks coloured by element with custom carbons coloured yellow and orange, respectively. FA-C10 represented in sticks coloured by element with salmon custom carbons.* ***a.*** T. terrestris *cutinase represented in green cartoon figure with docked FA-C10.* ***b.*** T. terrestris *cutinase represented in green cartoon figure with docked FA-C10. Measurements displayed are in Å and are represented by yellow dashed lines* ***c.*** T. terrestris *cutinase represented in green surface figure. The aliphatic domain of FA-C10 goes through the binding tunnel.*

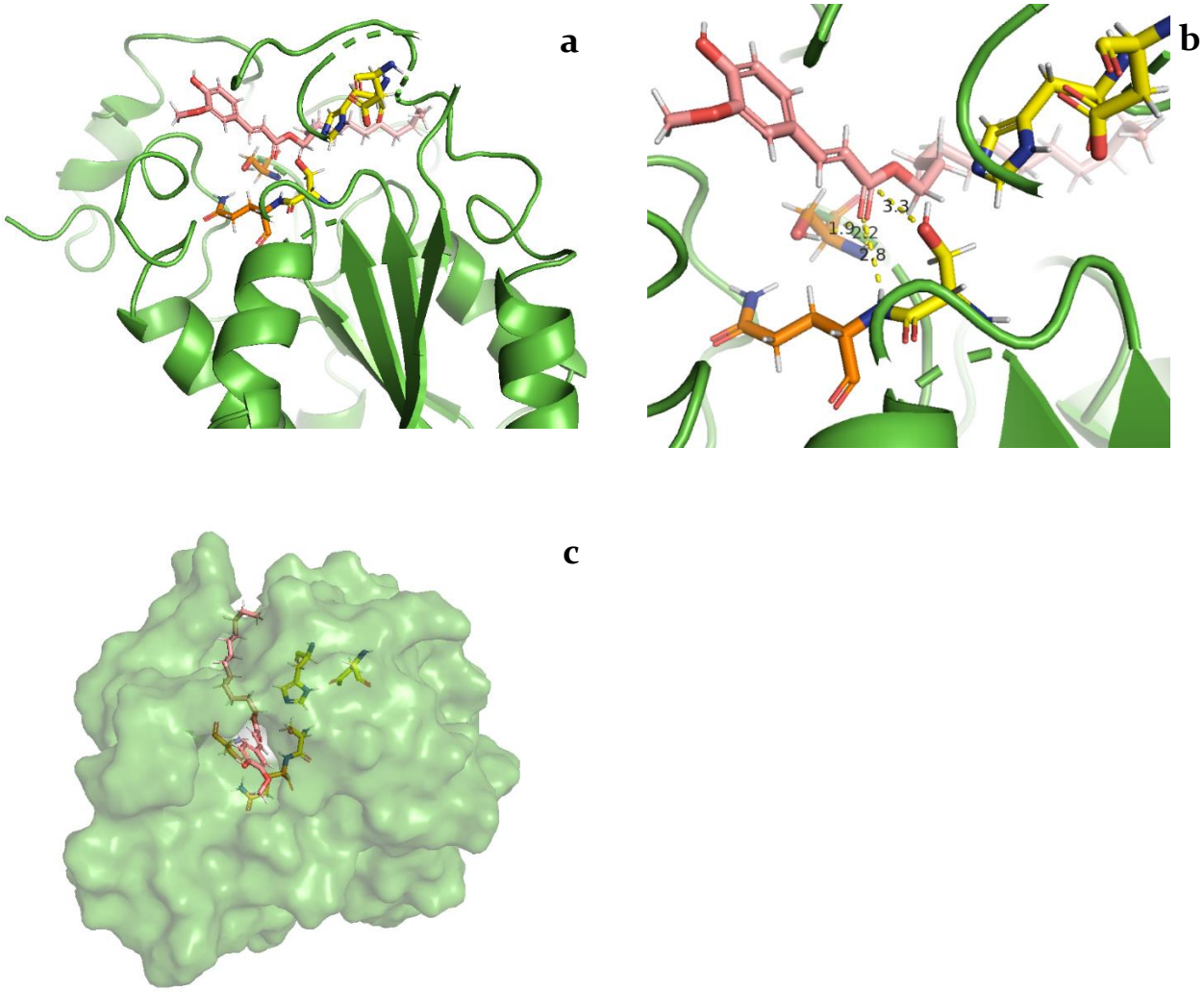

Figure S 21. *Docking of FA-C12 in* T. terrestris *cutinase. Active site and oxyanion hole residues show in sticks coloured by element with custom carbons coloured yellow and orange, respectively. FA-C12 represented in sticks coloured by element with salmon custom carbons.* ***a.*** T. terrestris *cutinase represented in green cartoon figure with docked FA-C12.* ***b.*** T. terrestris *cutinase represented in green cartoon figure with docked FA-C12. Measurements displayed are in Å and are represented by yellow dashed lines* ***c.*** T. terrestris *cutinase represented in green surface figure. The aliphatic domain of FA-C12 goes through the binding tunnel.*

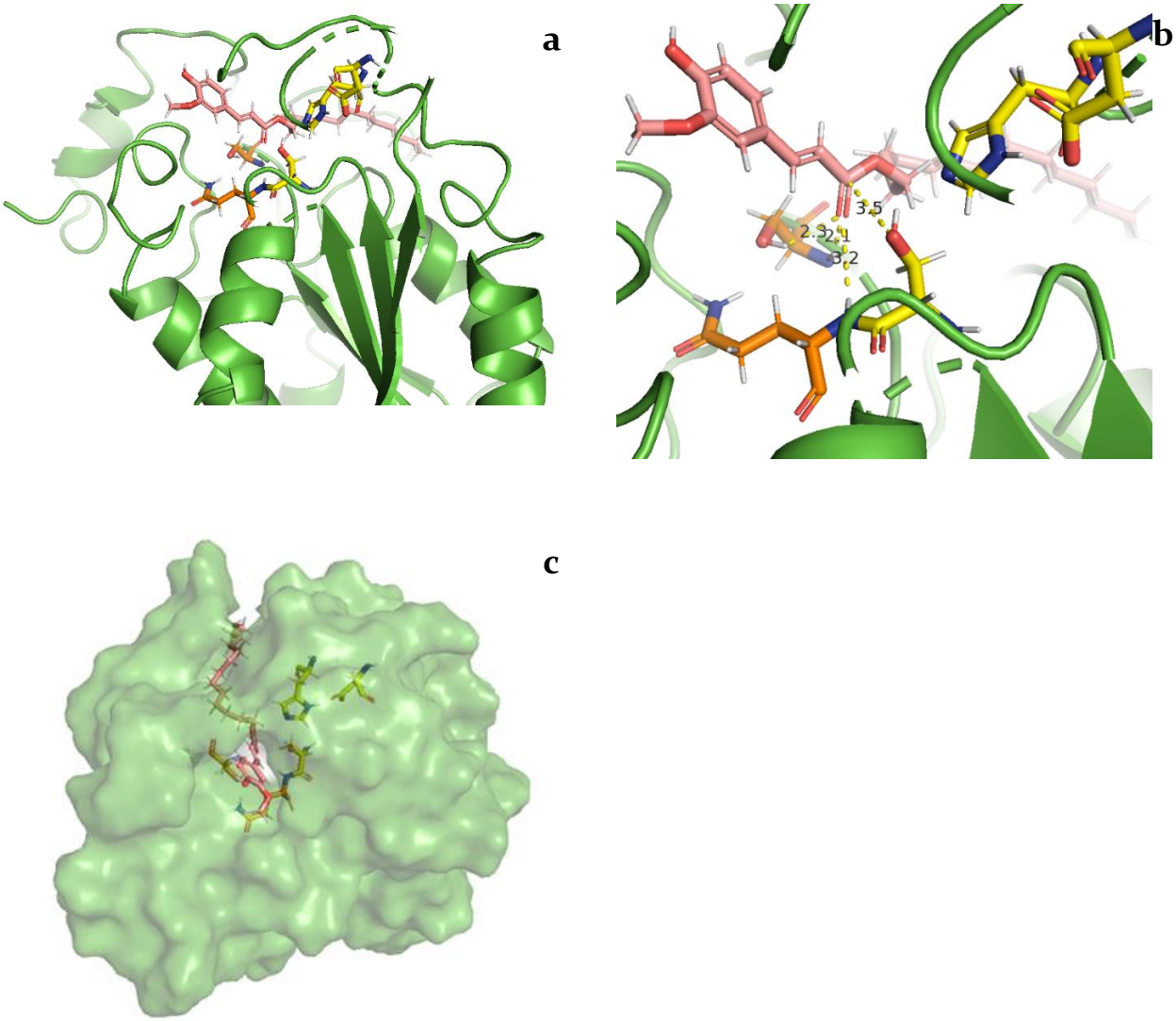

Figure S 22. *Docking of FA-C14 in* T. terrestris *cutinase. Active site and oxyanion hole residues show in sticks coloured by element with custom carbons coloured yellow and orange, respectively. FA-C14 represented in sticks coloured by element with salmon custom carbons.* ***a.*** T. terrestris *cutinase represented in green cartoon figure with docked FA-C14.* ***b.*** T. terrestris *cutinase represented in green cartoon figure with docked FA-C14. Measurements displayed are in Å and are represented by yellow dashed lines* ***c.*** T. terrestris *cutinase represented in green surface figure. The aliphatic domain of FA-C14 goes through the binding tunnel.*

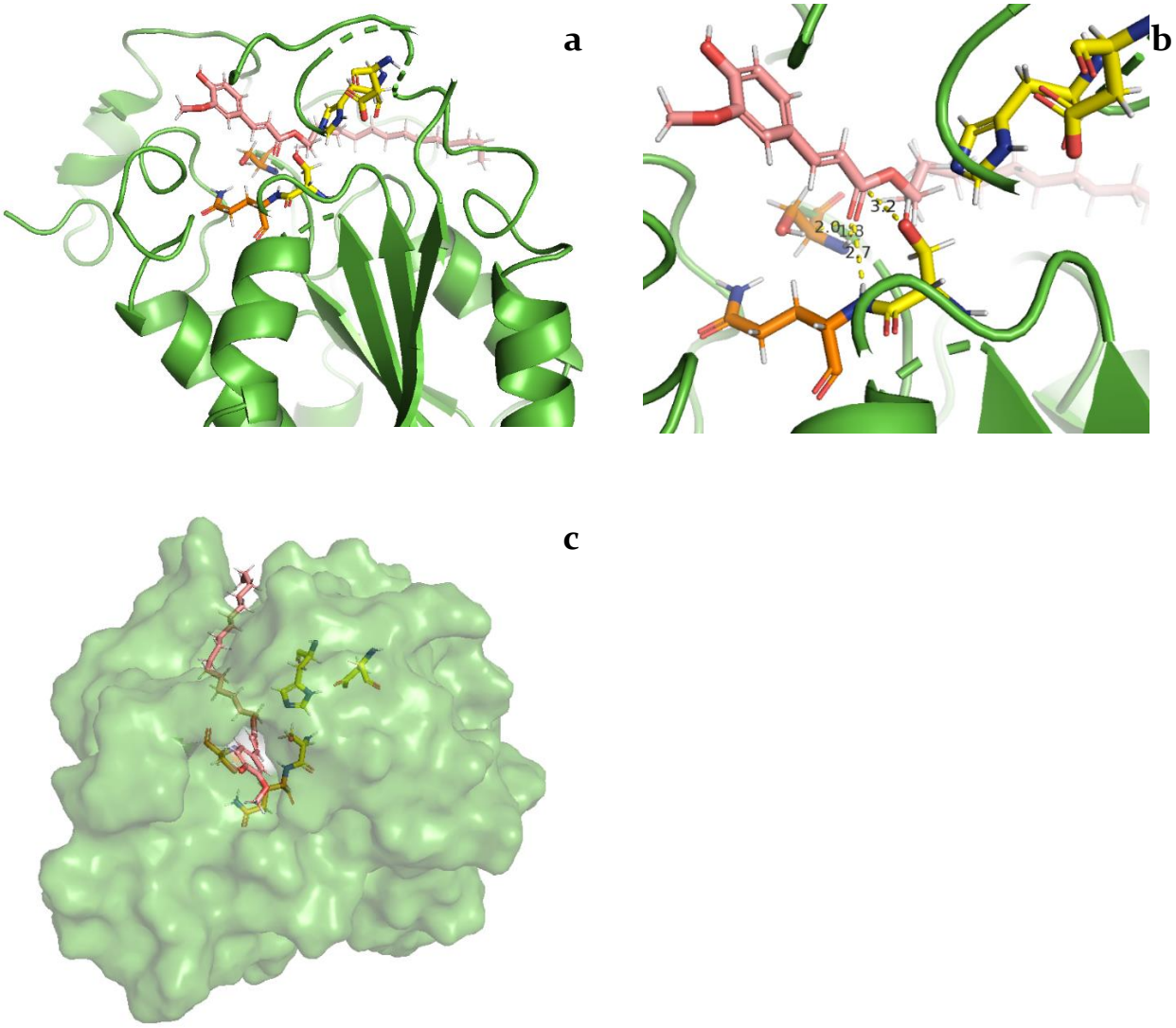

Figure S 23. *Docking of FA-C16 in* T. terrestris *cutinase. Active site and oxyanion hole residues show in sticks coloured by element with custom carbons coloured yellow and orange, respectively. FA-C16 represented in sticks coloured by element with salmon custom carbons.* ***a.*** T. terrestris *cutinase represented in green cartoon figure with docked FA-C16.* ***b.*** T. terrestris *cutinase represented in green cartoon figure with docked FA-C16. Measurements displayed are in Å and are represented by yellow dashed lines* ***c.*** T. terrestris *cutinase represented in green surface figure. The aliphatic domain of FA-C16 goes through the binding tunnel.*

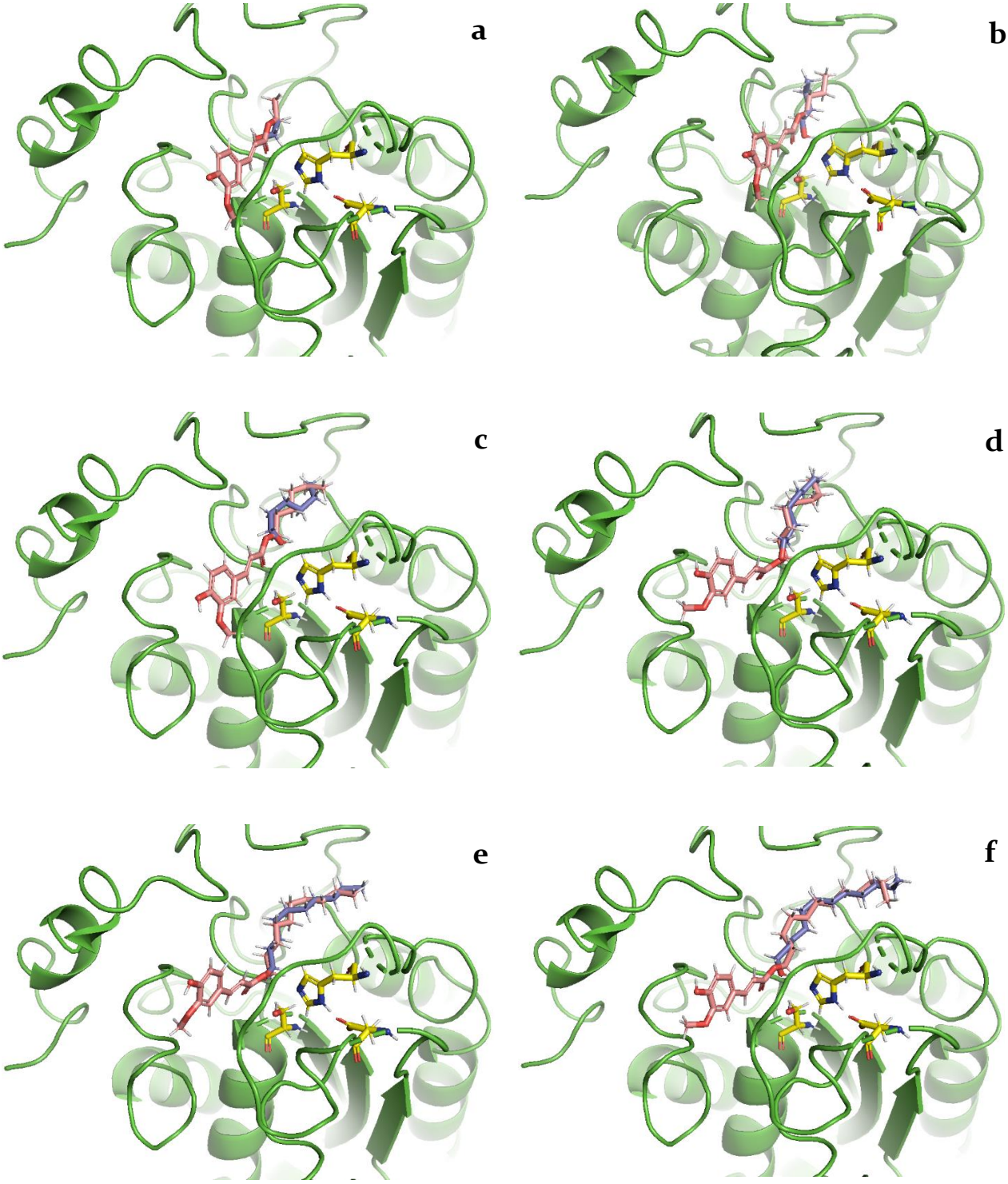
a
b
c
d
e
f

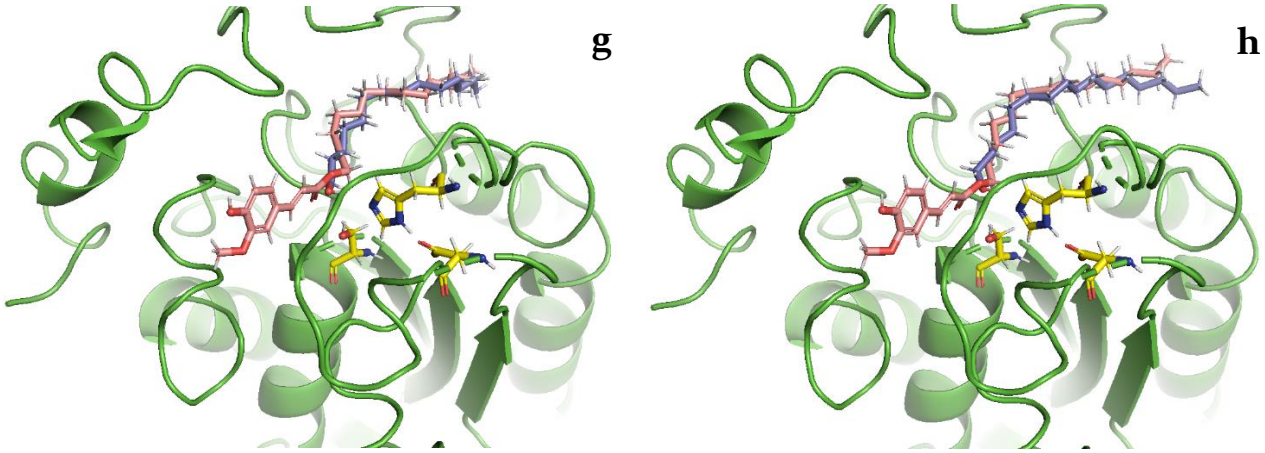

Figure S 24. *Substrate vs. product docking in* T. terrestris *cutinase.* T. terrestris *cutinase represented in green cartoon figure. Active site residues show in sticks with custom carbons coloured yellow. Substrate and correspondent product represented in sticks coloured by element with salmon and blue custom carbons, respectively.* ***a.*** *FA-C2 vs. OH-C2.* ***b.*** *FA-C4 vs. OH-C4* ***c.*** *FA-C6 vs. OH-C6.* ***d.*** *FA-C8 vs. OH-C8.* ***e.*** *FA-10 vs. OH-C10.* ***f.*** *FA-C12 vs. OH-C12.* ***g.*** *FA-C14 vs. OH-C14.* ***h.*** *FA-C16 vs. OH-C16.*

Table S 3. *Experimental specific activities of* F. solani, M. cinnamomea *and* T. terrestris *cutinases.*

Substrate	**Experimental specific activity (U/mg)**		
	T. terrestris cutinase	*F. solani* cutinase	*M. cinnamomea* cutinase
pNPA (C_2)	266.2 ± 4.5	151.4 ± 11.2	553.5 ± 2.5
pNPB (C_4)	2322.4 ± 17.8	456.5 ± 19.8	1147.9 ± 8.3
pNPH (C_6)	1056.4 ± 18.8	473.1 ± 22.3	1076.2 ± 5.0
pNPC (C_8)	1043.1 ± 5.8	---	646.9 ± 33.3
pNPD (C_{10})	1262.3 ± 8.7	558.3 ± 24.8	607.6 ± 28.3
pNPL (C_{12})	1257.1 ± 1.4	203.6 ± 33.1	494.5 ± 5.0
pNPM (C_{14})	880.7 ± 7.2	140.7 ± 33	962.6 ± 5.0
pNPP (C_{16})	412.6 ± 15.2	44.7 ± 3.5	619.5 ± 10.8

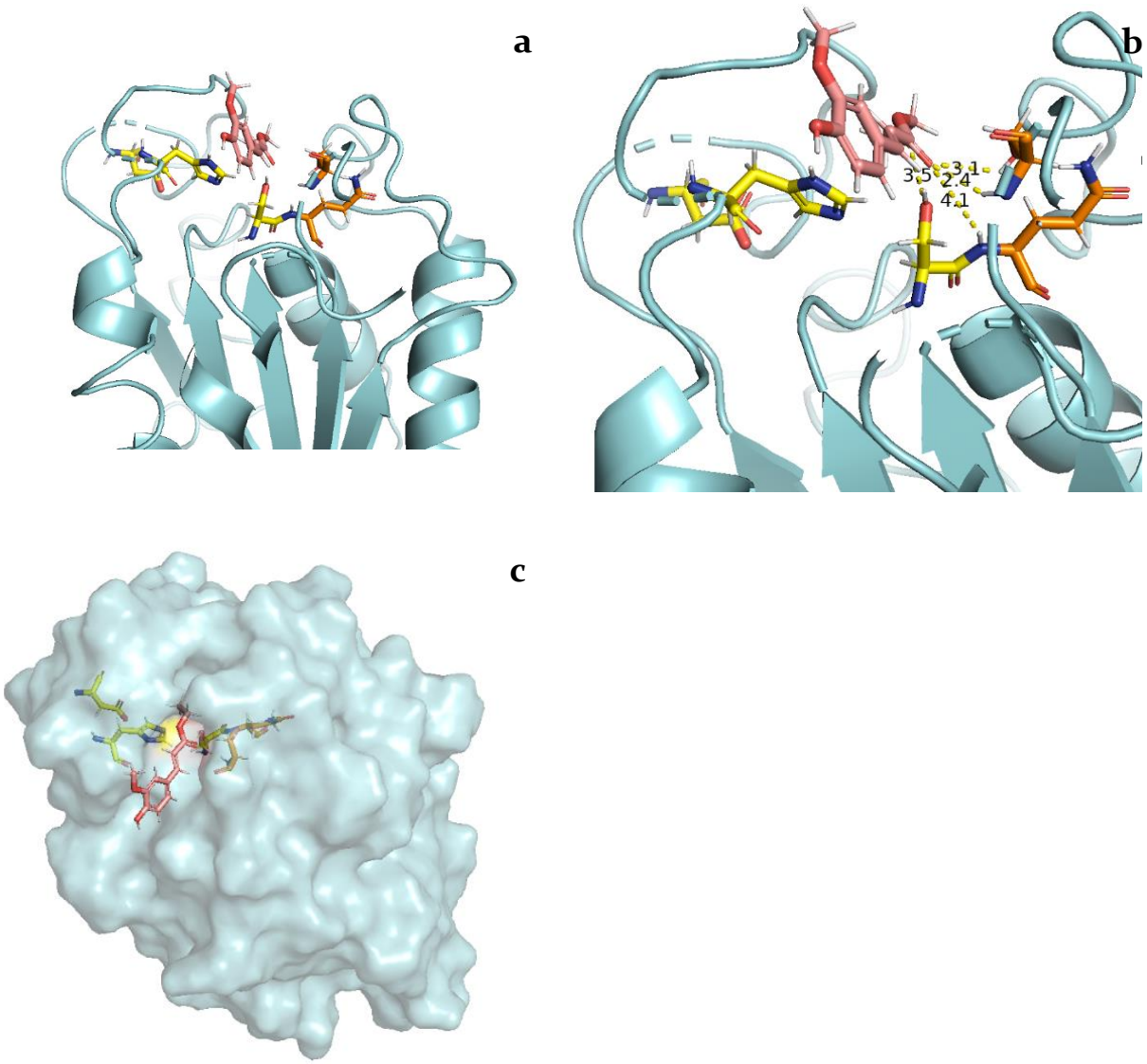

Figure S 25. *Docking of FA-C2 in* F. solani *cutinase. Active site and oxyanion hole residues show in sticks coloured by element with custom carbons coloured yellow and orange, respectively. FA-C2 represented in sticks coloured by element with salmon custom carbons.* ***a.*** F. solani *cutinase represented in cyan cartoon figure with docked FA-C2.* ***b.*** F. solani *cutinase represented in cyan cartoon figure with docked FA-C2. Measurements displayed are in Å and are represented by yellow dashed lines* ***c.*** F. solani *cutinase represented in cyan surface figure. The aliphatic domain of FA-C2 goes through the binding tunnel.*

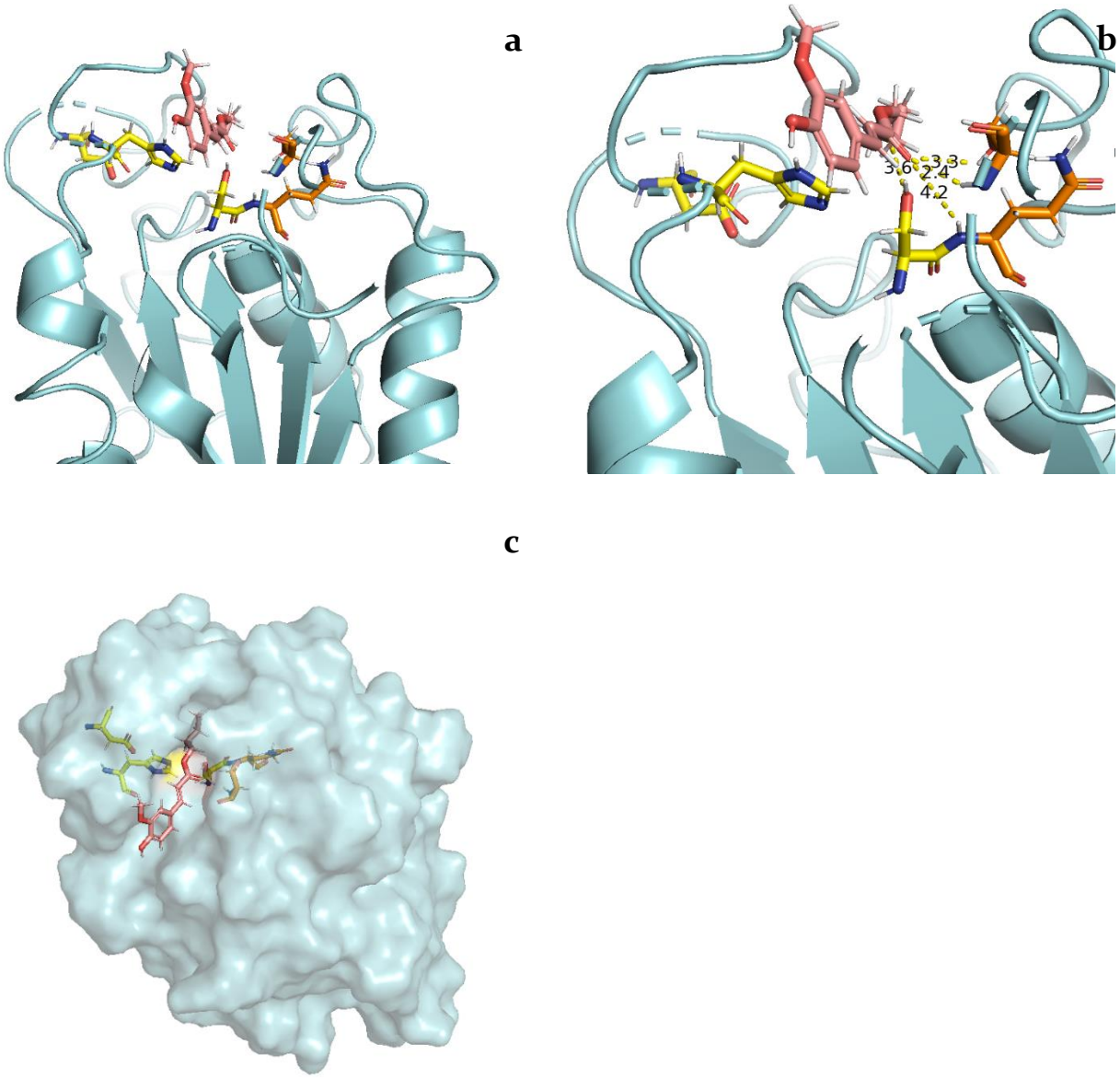

Figure S 26**. Docking of FA-C4 in* F. solani *cutinase. Active site and oxyanion hole residues show in sticks coloured by element with custom carbons coloured yellow and orange, respectively. FA-C4 represented in sticks coloured by element with salmon custom carbons.* ***a. F. solani *cutinase represented in cyan cartoon figure with docked FA-C4.* ***b.*** F. solani *cutinase represented in cyan cartoon figure with docked FA-C4. Measurements displayed are in Å and are represented by yellow dashed lines* **c.** F. solani *cutinase represented in cyan surface figure. The aliphatic domain of FA-C4 goes through the binding tunnel.*

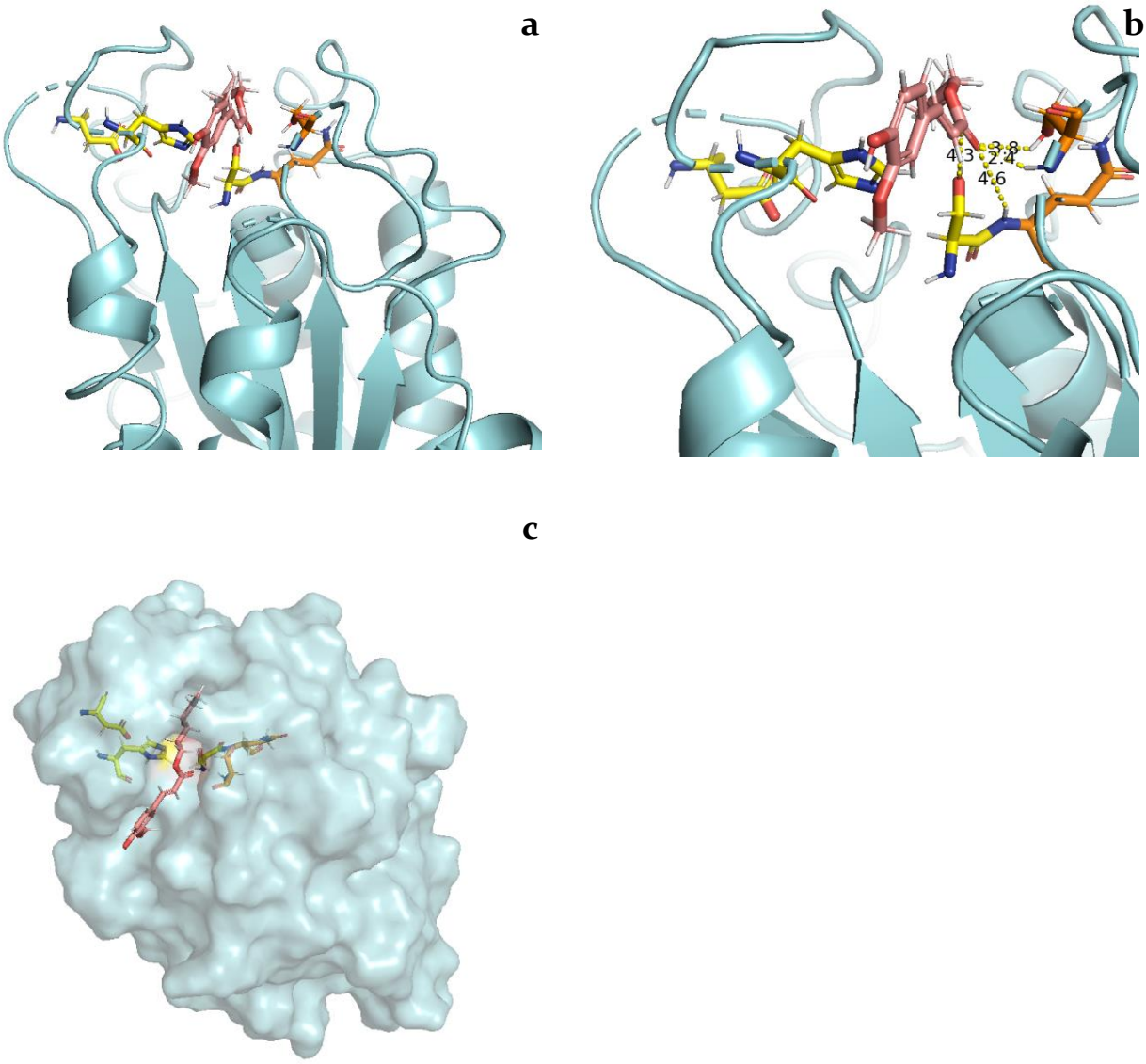

Figure S 27*. Docking of FA-C6 in* F. solani *cutinase. Active site and oxyanion hole residues show in sticks coloured by element with custom carbons coloured yellow and orange, respectively. FA-C6 represented in sticks coloured by element with salmon custom carbons.* ***a.*** F. solani *cutinase represented in cyan cartoon figure with docked FA-C6.* ***b.*** F. solani *cutinase represented in cyan cartoon figure with docked FA-C6. Measurements displayed are in Å and are represented by yellow dashed lines* ***c.*** F. solani *cutinase represented in cyan surface figure. The aliphatic domain of FA-C6 goes through the binding tunnel.*

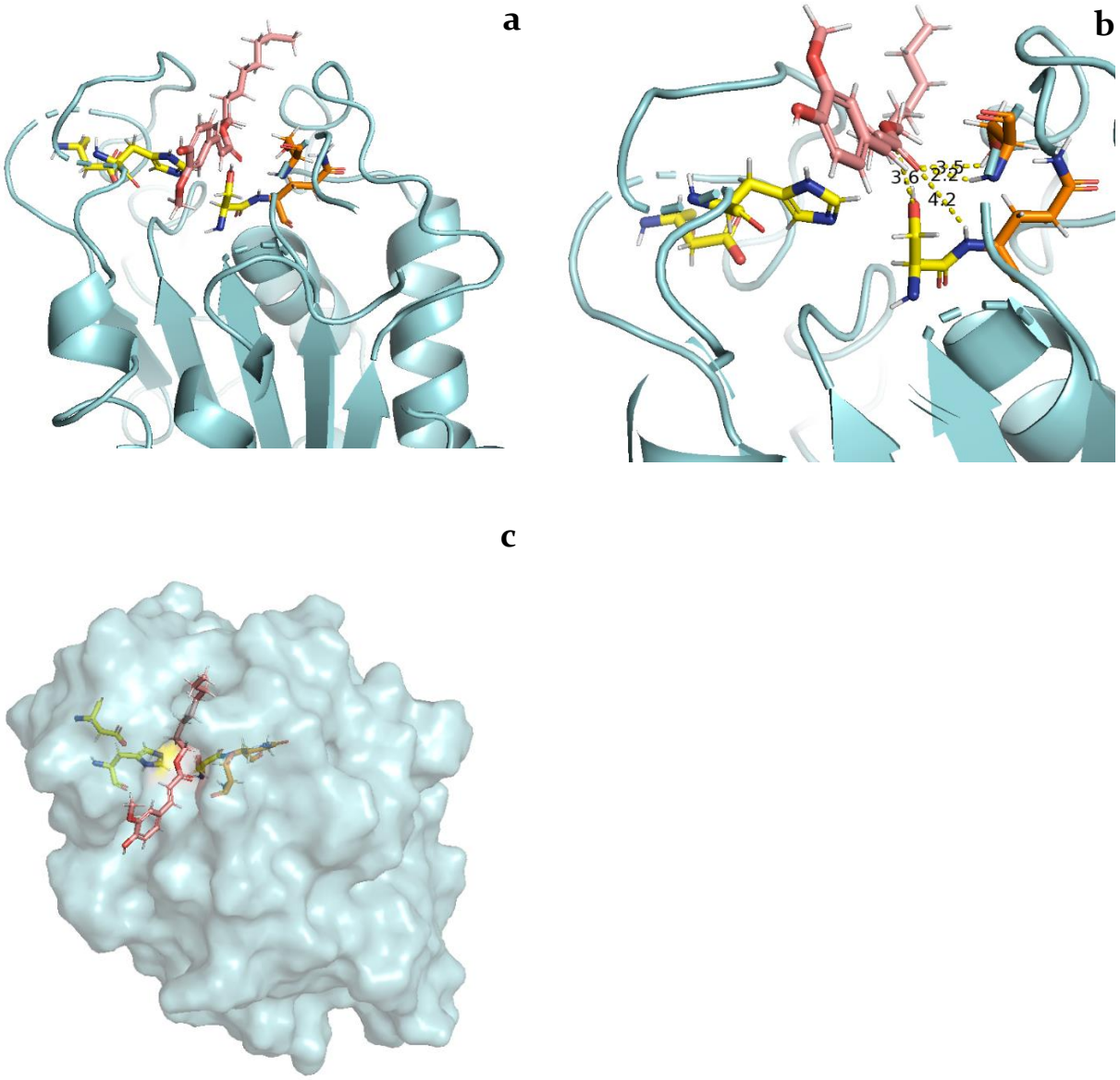

Figure S 28**. Docking of FA-C8 in* F. solani *cutinase. Active site and oxyanion hole residues show in sticks coloured by element with custom carbons coloured yellow and orange, respectively. FA-C8 represented in sticks coloured by element with salmon custom carbons.* ***a. F. solani *cutinase represented in cyan cartoon figure with docked FA-C8.* ***b.*** F. solani *cutinase represented in cyan cartoon figure with docked FA-C8. Measurements displayed are in Å and are represented by yellow dashed lines* ***c.*** F. solani *cutinase represented in cyan surface figure. The aliphatic domain of FA-C8 goes through the binding tunnel.*

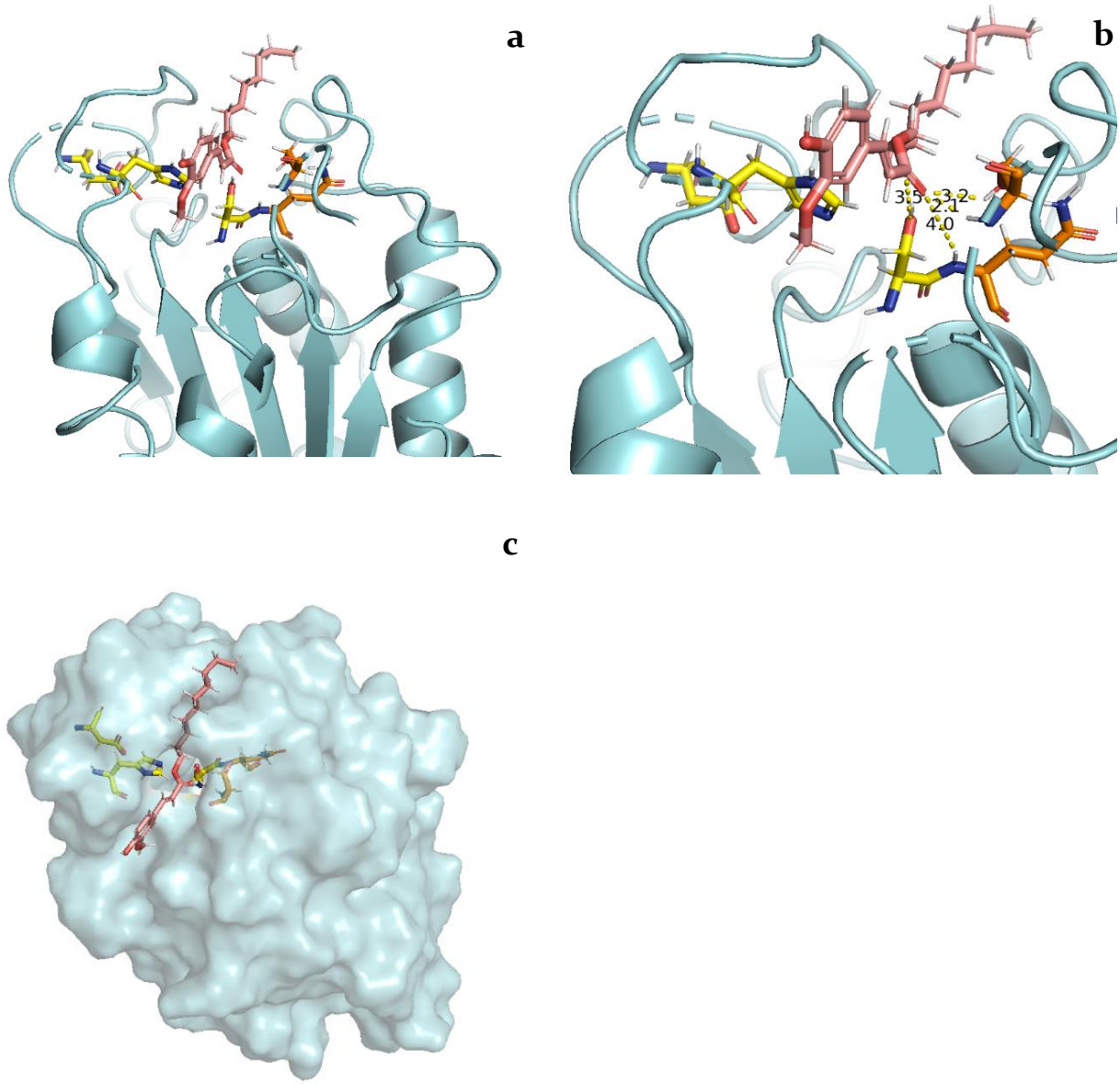

Figure S 29**. Docking of FA-C10 in* F. solani *cutinase. Active site and oxyanion hole residues show in sticks coloured by element with custom carbons coloured yellow and orange, respectively. FA-C10 represented in sticks coloured by element with salmon custom carbons.* ***a. F. solani *cutinase represented in cyan cartoon figure with docked FA-C10.* ***b.*** F. solani *cutinase represented in cyan cartoon figure with docked FA-C10. Measurements displayed are in Å and are represented by yellow dashed lines* ***c.*** F. solani *cutinase represented in cyan surface figure. The aliphatic domain of FA-C10 goes through the binding tunnel.*

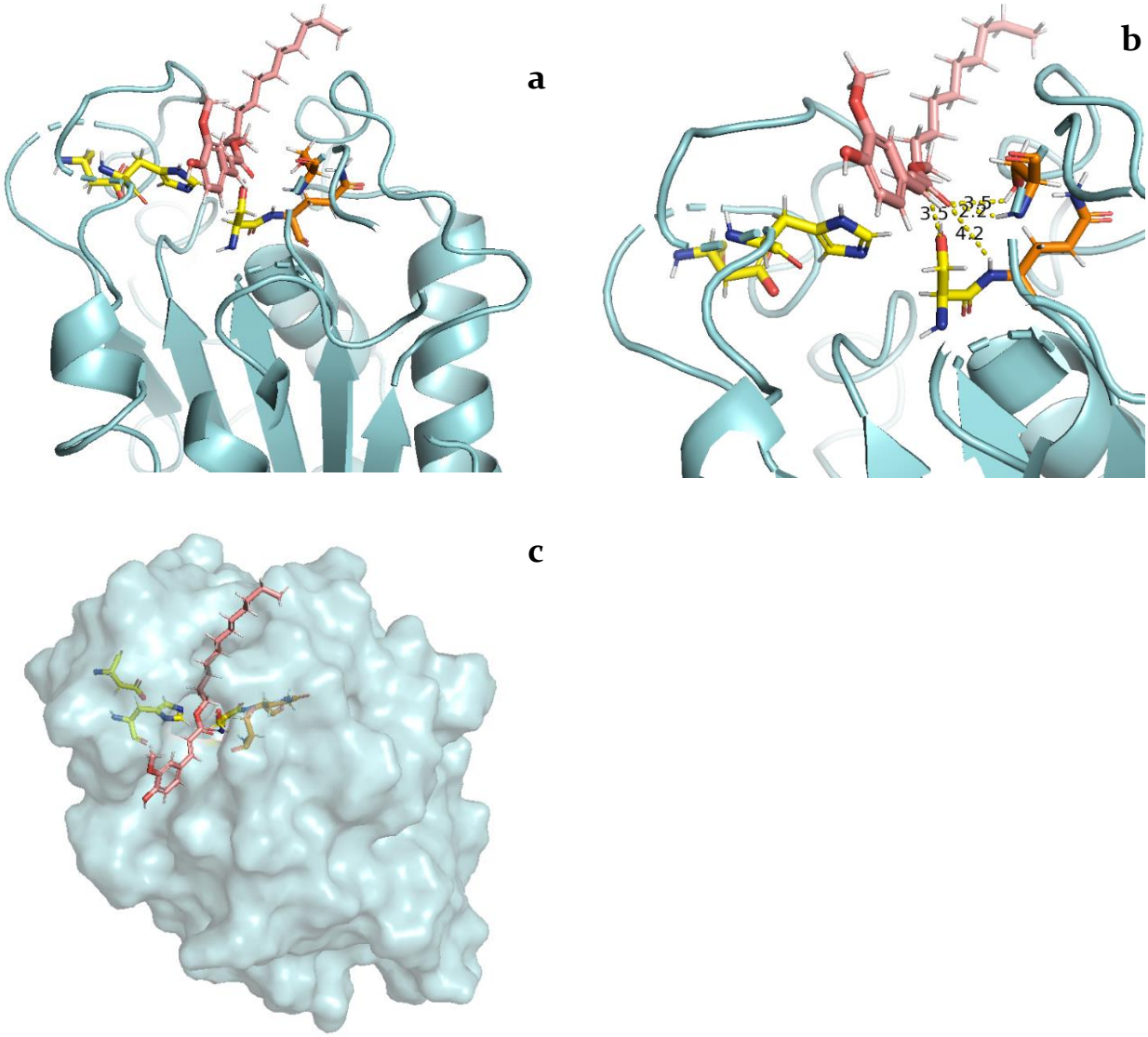

Figure S 30**. Docking of FA-C12 in* F. solani *cutinase. Active site and oxyanion hole residues show in sticks coloured by element with custom carbons coloured yellow and orange, respectively. FA-C12 represented in sticks coloured by element with salmon custom carbons.* ***a. F. solani *cutinase represented in cyan cartoon figure with docked FA-C12.* ***b.*** F. solani *cutinase represented in cyan cartoon figure with docked FA-C12. Measurements displayed are in Å and are represented by yellow dashed lines* ***c.*** F. solani *cutinase represented in cyan surface figure. The aliphatic domain of FA-C12 goes through the binding tunnel.*

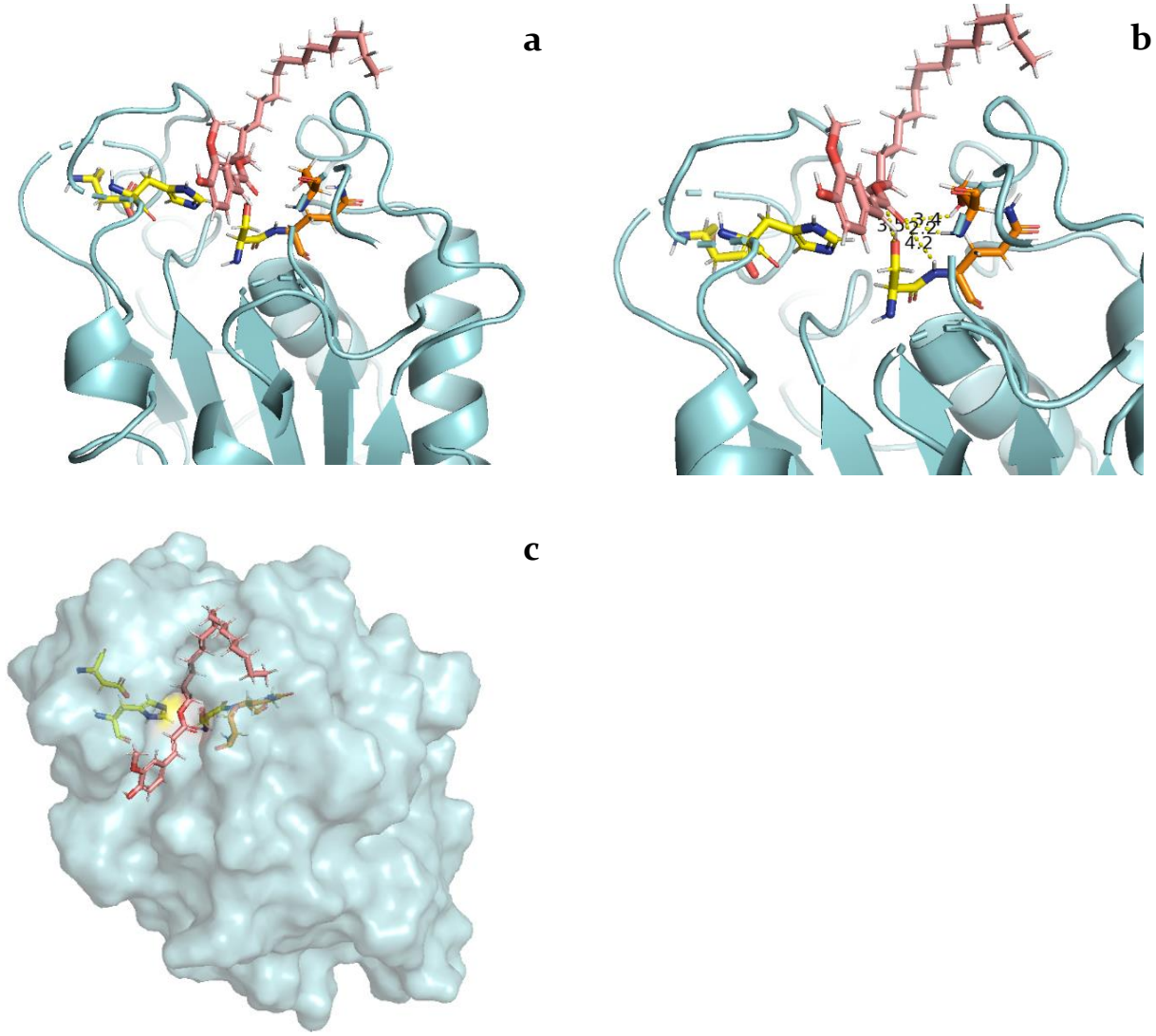

Figure S 31*. Docking of FA-C16 in* F. solani *cutinase. Active site and oxyanion hole residues show in sticks coloured by element with custom carbons coloured yellow and orange, respectively. FA-C16 represented in sticks coloured by element with salmon custom carbons.* ***a.*** F. solani *cutinase represented in cyan cartoon figure with docked FA-C16.* ***b.*** F. solani *cutinase represented in cyan cartoon figure with docked FA-C16. Measurements displayed are in Å and are represented by yellow dashed lines* **c.** F. solani *cutinase represented in cyan surface figure. The aliphatic domain of FA-C16 goes through the binding tunnel.*

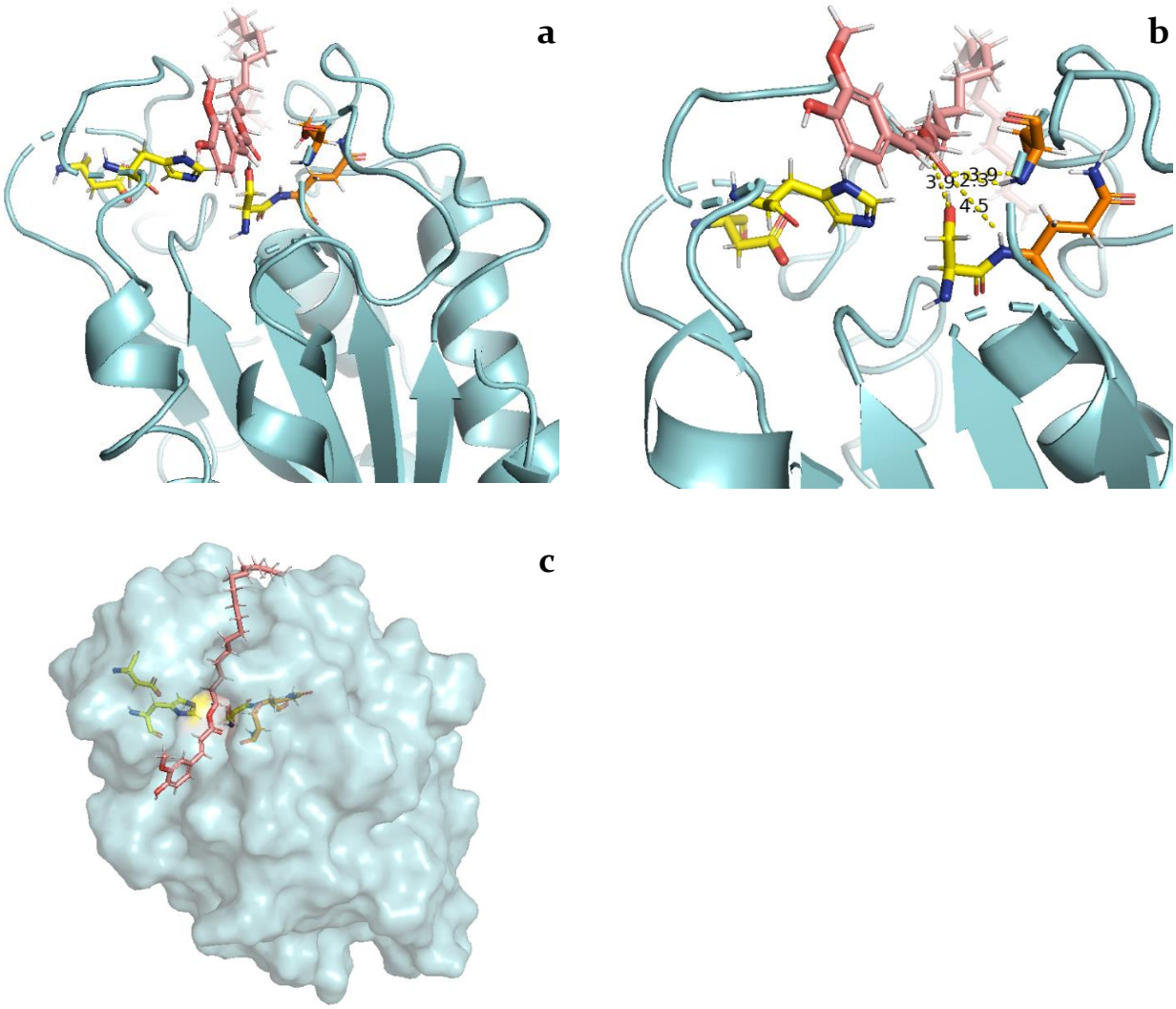

Figure S 32**. Docking of FA-C18 in* F. solani *cutinase. Active site and oxyanion hole residues show in sticks coloured by element with custom carbons coloured yellow and orange, respectively. FA-C18 represented in sticks coloured by element with salmon custom carbons.* ***a. F. solani *cutinase represented in cyan cartoon figure with docked FA-C18.* ***b.*** F. solani *cutinase represented in cyan cartoon figure with docked FA-C18. Measurements displayed are in Å and are represented by yellow dashed lines* ***c.*** F. solani *cutinase represented in cyan surface figure. The aliphatic domain of FA-C18 goes through the binding tunnel.*

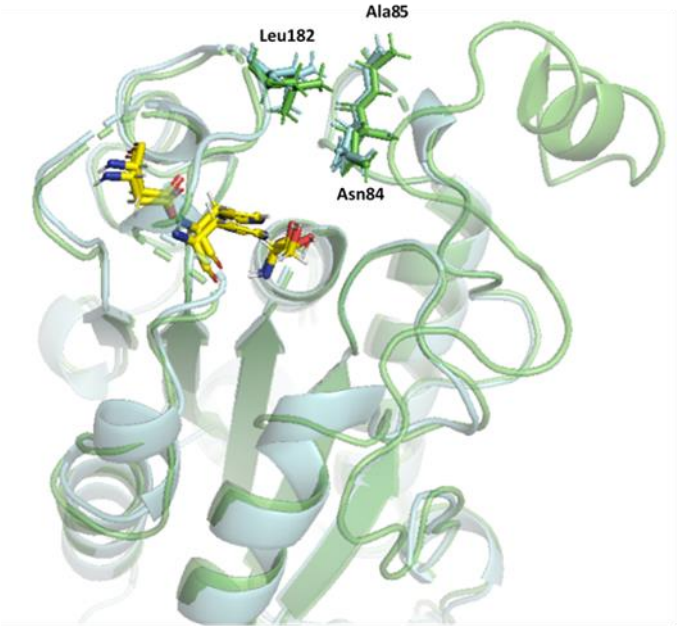

Figure S 33. *Top enclosing binding residues in* F. solani *and* T. terrestris *cutinases aligned.* F. solani *cutinase (PDB ID: 1cex) coloured cyan and* T. terrestris *cutinase coloured green.* F. solani *cutinase binding residues, Leu182-Asn84-Ala85, show in cyan sticks and homologous* T. terrestris *cutinase residues show in green sticks.*

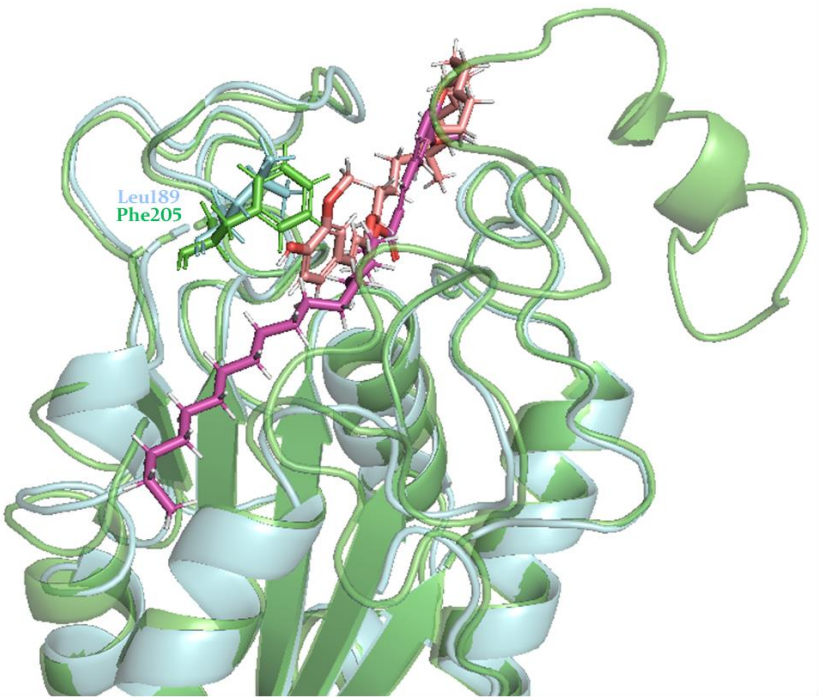

Figure S 34. *Substitution of Leu189 in* F. solani *cutinase (PDB ID: 1cex) for a Phe205 in* T. terrestris *cutinase. Residues show in sticks.* F. solani *cutinase coloured cyan and* T. terrestris *cutinase coloured green. Reverse ligand pose between the two docked enzymes.*

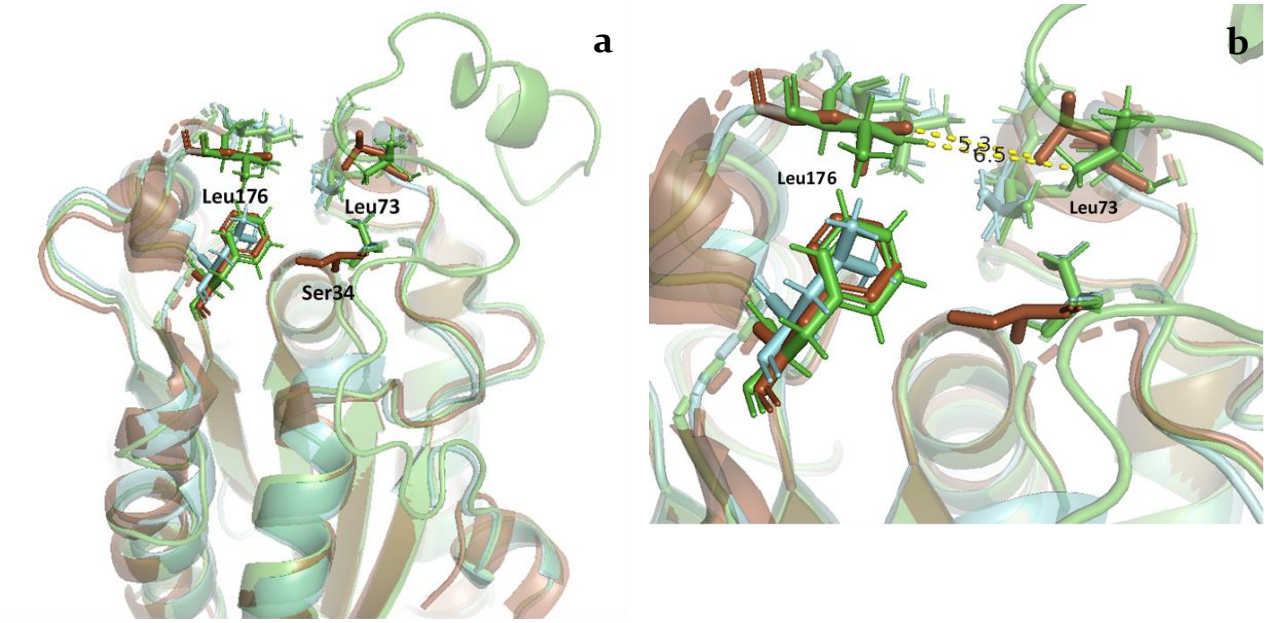

Figure S 35. *Binding cleft is smaller in* M. cinnamomea *cutinase.* M. cinnamomea *cutinase (brown),* T. terrestris *cutinase (green) and* F. solani *cutinase (cyan). Binding cleft residues show in sticks.* ***a.*** *Serine34 from* M. cinnamomea *cutinase is blocking entrance.* ***b.*** *Distance from Leu176-Leu73 is smaller compared to distance between the homologous residues in* T. terrestris *cutinase. Distances in Å.*

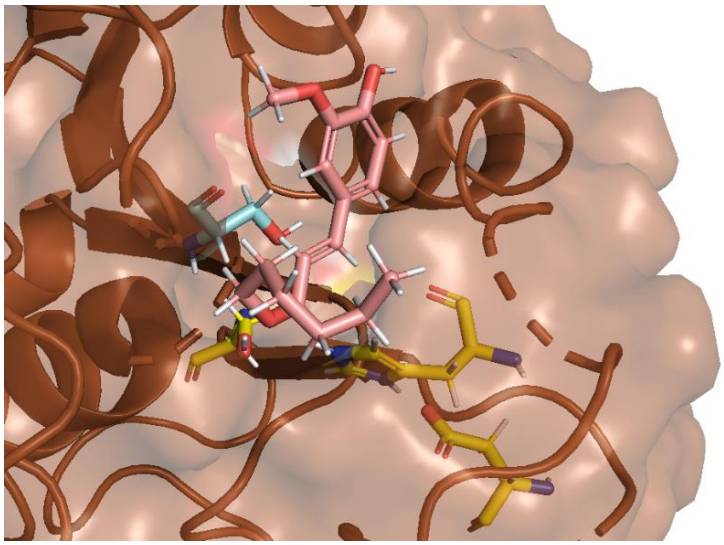

Figure S 36. *Steric hindrance of serine in* M. cinnamomea *cutinase. Serine from* M. cinnamomea *cutinase (cyan stick) is blocking the entrance of FA-C6 (represented by sticks coloured by element with salmon custom carbons). Image purely illustrative. It is still a bad docked pose for the ligand as the enzyme still reports activity for this chain length.*